MECHANISM OF FLUORIDE-BASED ETCH AND CLEAN PROCESSES

A Thesis
Presented to
The Academic Faculty

by

Ashish Arunkumar Pande

In Partial Fulfillment
of the Requirements for the Degree
Doctor of Philosophy in Chemical Engineering in the
School of Chemical and Biomolecular Engineering

Georgia Institute of Technology
May, 2011

MECHANISM OF FLUORIDE-BASED ETCH AND CLEAN PROCESSES

Approved by:

Dr. D. W. Hess, Advisor
School of Chemical and Biomolecular Engineering
Georgia Institute of Technology

Dr. A. B. Frazier,
School of Electrical and Computer Engineering
Georgia Institute of Technology

Dr. C. L. Henderson
School of Chemical and Biomolecular Engineering
Georgia Institute of Technology

Dr. J. Janata,
School of Chemistry and Biochemistry
Georgia Institute of Technology

Dr. C. L. Liotta
School of Chemical and Biomolecular Engineering &
School of Chemistry and Biochemistry
Georgia Institute of Technology

Date Approved: [Jan 19, 2011]

Life is a strange business. Happy is the man who is nothing.

J. Krishnamurti, *Letters to a young friend*

ACKNOWLEDGEMENTS

First of all, I want to thank my Advisor, Dr. D. W. Hess, for his continuous technical, non-technical and financial support throughout my Ph.D. It is remarkable that he was always charming with me and available for me at any point. I also want to thank my committee members, Dr. C. L. Henderson, Dr. J. Janata, Dr. C. L. Liotta and Dr. A. B. Frazier, for their valuable suggestions. I am thankful to Dr. Henderson for his comments on reflectometry as well as kindly allowing me access to his lab instrument. Dr. Grover's help in state estimator algorithm is specially appreciated. The funding for this work was provided by Lam Research Inc. I enjoyed working with Dr. D. S. L. Mui and Dr. J. Zhu of Lam Research.

A number of other professors at Georgia Tech helped me in my research by providing valuable technical comments. This includes Dr. Costas Tsouris and Dr. Sotira Yiacoumi (CE), Dr. Svens Behrens (ChBE), Dr. Minami Yoda (ME) and Dr. Paul Kohl (ChBE).

I am thankful to present and past members of Hess group. They helped me in my transition from modeling world to experimental world. Dr. G. Levitin provided valuable suggestions in my research. A special thanks to her for worrying about me when not everything was well with me. Dr. S. Pathak provided me valuable suggestions for reactor set up. Dr. B. Balu helped me whenever there was a problem with XPS. I will always remember the time I spent with Dr. Pathak, Dr. Balu and Sonam Sherpa while troubleshooting XPS. Dr. I. Song, Dr. Y. Xiong and Dr. L. Xiu encouraged me in my research. Fangyu Wu deposited a number of films for me on a very short note without expecting anything in return. Lester Lee and Michael Casciato were good people to work with.

In addition to Hess group members, I am also thankful to people from other group. Dr. R. Xiong helped me in state estimator's algorithms. Ugur (Lee group) helped me in a number of Matlab troubleshooting problems. Past and present members of Henderson, Grover (Andres!), Kohl group in ChBE and Mizaikoff (chemistry) helped in running a number of experiments. Pei, Yanhui and Firman provided me 'open' access to Dr. Teja's lab and treated me as part of their group. I am specially thankful to Dr. Gelbaum for his support and training in NMR, without him, most part of NMR work would have been imcomplete. A number of my friends in Georgia Tech helped me in troubleshooting issues with Fluent, Matlab or other softwares.

Gloria Beale patiently placed orders for countless things in my research. Bradley and Jeff from machine shop fabricated a number of things for me. Kevin Guger helped me in a number of computer related issues.

I am thankful to my friends at Georgia Tech and outside for bearing with me for so long. Dhaval, Manoj, Prashant (NO ORDER!) and Annapoorani were with me since the time I joined GT. Divya, Swati, Prabuddha, Pramod were with me through difficult days at GT. Each passing year only added to my list of friends at GT. Samir and Suchitra provided a strong motivation to work for Vibha. Without all of my friends, my life at GT seemed meaningless. My present and past room-mates have faced a number of problems for me. My family members have provided moral support throughout my Ph.D. I cannot imagine a world without them.

TABLE OF CONTENTS

Page

LIST OF TABLES

LIST OF FIGURES

LIST OF SYMBOLS AND ABBREVIATIONS

BF	BiFluoride
BHF	Buffered HF
BPSG	Boron Phosphorus Silicate Glass
CFD	Computational Fluid Dynamics
DMSO	Dimethyl Sulfoxide
DT	DihydrogenTrifluoride
EKF	Extended Kalman Filter
ER	Etch Rate
F	Fluoride
FEOL	Front End Of Line
FTIR	Fourier Transform Infrared
IC	Integrated Circuit
MEMS	MicroElectroMechanical systems
mMHE	modified Moving Horizon Estimator
MSE	Mean Square of Errors
NMR	Nuclear Magnetic Resonance
QCM	Quartz Crystal Microbalance
RLS	Recursive Least Squares
SE	Spectroscopic Ellipsometry
SEM	Scanning Electron Microscope
SR	Spectroscopic Reflectometry
TBA	TetraButylAmmonium

THF	Tetrahydrofuran
TOX	Thermally grown SiO_2

SUMMARY

Fluoride-containing solutions are widely used to etch silicon dioxide-based films. A critical issue in integrated circuit (IC) and microelectromechanical systems (MEMS) fabrication is achievement of adequate selectivity during the etching of different film materials when they are present in different areas on a device or in a stack. The use of organic fluoride-based salts in aqueous/organic solvent solutions can yield etch selectivities <1.9 for thermally-grown silicon dioxide relative to borophosphosilicate glass films, and thus may also obviate the need to add surfactants to the etch solutions to realize uniform etching. Etch studies with aqueous-organic fluoride salt-based solutions also offer insight into the etch mechanism of these materials. Specifically, the importance of water content in the solutions and of ion solvation in controlling the etch chemistry is described.

With respect to fluoride-containing solutions, etching of SiO_2 films using aqueous HF-based chemistries is widely used in IC and MEMS industries. To precisely control film loss during cleaning or etching processes, good control over the contact time between the liquid (wet) chemistry and the substrate is necessary. An integrated wet etch and dry reactor system has been designed and fabricated by studying various geometrical configurations using computational fluid dynamics (CFD) simulations incorporating reaction kinetics from laboratory data and previously published information. The effect of various process parameters such as HF concentration, flow rate, and flow velocity on the etch rates and uniformity of thermally-grown silicon dioxide and borophosphosilicate glass films was studied. Simulations agree with experiments within experimental error.

This reactor can also be used to wet etch/clean and dry other films in addition to SiO_2-based films using aggressive chemistries as well as aqueous HF under widely different process conditions.

A spectroscopic reflectometry technique has been implemented in-situ in this custom fabricated reactor to monitor the thickness and etch rate in wet etching environments. The advantages of this technique over spectroscopic ellipsometry in specific situations are discussed. A first principles model has been developed to analyze the reflectometry data. The model has been validated on a large number of previously published studies. The match between experimental and simulated thickness is good, with the difference ~ 5 nm. In-situ thickness and etch rate have been estimated using Recursive Least Squares (RLS), Extended Kalman Filter (EKF) and modified Moving Horizon Estimator (mMHE) analyses applied to spectroscopic reflectometry using multiple wavelengths with ZnO employed as a model film. The initial guess for EKF and mMHE has been obtained from a CFD model. It has been shown that both EKF and mMHE are less oscillatory than RLS/LS in the prediction of thickness and ER and more robust when a smaller number of wavelengths are used, in addition, the computational time for EKF is less than that of mMHE/RLS. For no restrictions on computational requirements, LS should be the method of choice whereas in the case of faster etching systems, with the availability of a better process model, EKF should be starting point. The choice of algorithm is thus based on sampling rate for data collection, process model uncertainty and the number of wavelengths required.

CHAPTER 1

INTRODUCTION

Transistors serve as tiny switches that are at the heart of microprocessor operation. Progress in the microelectronics industry is typically gauged by adherence to Moore's Law, which originally stated that the number of transistors doubles every two years[1]. The progression of minimum feature size (also referred to as device generation) and functionality (number of transistors) in Intel microprocessors over a period of thirty years is shown in Figure 1. Although an ambitious prediction, the microelectronics industry has achieved or even exceeded this claim for the past 40 years through the implementation and integration of material and process innovations.

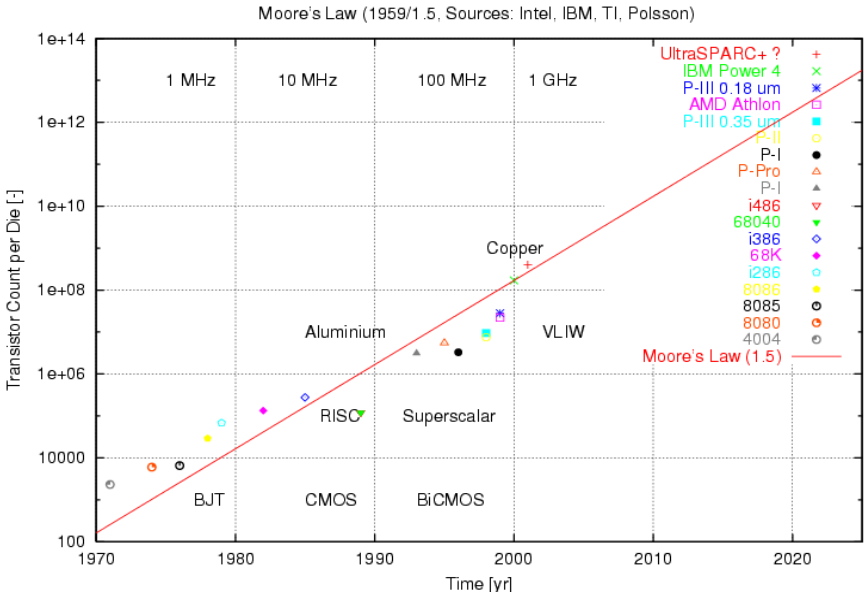

Figure 1 Moore's law for transistor count [2]

IC fabrication is performed in a layer-by-layer or sequential processing approach in which the devices are fabricated bottom-up by a series of repetitive process steps such as cleaning and surface preparation, ion implantation, photolithography, film deposition, film etching, and device and circuit metallization. Etching represents a critical step in conventional pattern transfer processing. The lithographic and etch processes are significant contributors to the final dimension, dimensional variation, and functionality of patterned features[1]. In order to reduce the processing time and cost, it may be advantageous to consider simplified fabrication scenarios that reduce the number of pattern transfer steps and the corresponding process related variability. Thus, integrated processes that combine several process steps into one step are attractive. _ENREF_1

Liquid phase processing is used routinely in the fabrication of integrated circuits ICs, MEMS, and nano-structured devices. In particular, liquid-based processes are invoked for etching, cleaning, rinsing, surface conditioning, and drying[3-5]. Surface cleaning, rinsing, residue removal, and conditioning sequences represent approximately 20% of the total number of processing steps used in the fabrication of state-of-the-art ICs[5].

The use of thin (<20 nm) films, closely-spaced features, and ultra-shallow (<50 nm) junctions exacerbates the control necessary for effective liquid cleaning. Implementation of alternate or new (to the IC industry) materials into device structures is taking place in order to keep pace with Moore's Law. Selectivity (difference in etch rate between two materials for a specific cleaning chemistry/condition) in cleaning and etching processes is therefore paramount. Figure 2 and Figure 3 illustrate the terminology of selecitivity and

isotropic etch [6]. As shown in Figure 2, a poorly selective etch removes the top film, but also attacks the underlying film or substrate, whereas an infinitely selective etch leaves the underlying material unetched. As shown in Figure 3, a perfectly isotropic etch produces rounded sidewalls, whereas a completely anisotropic etch produces vertical sidewalls. In IC processing, we typically desire highly anisotropic etch processes in order to enhance the packing density of devices. However, isotropic etches are often required in MEMS processing where a 'cantilever' structure is to be fabricated.

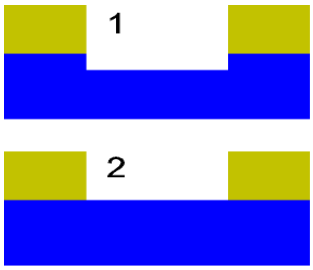

Figure 2 selective (2) vs. non-selective (1) etch [6]

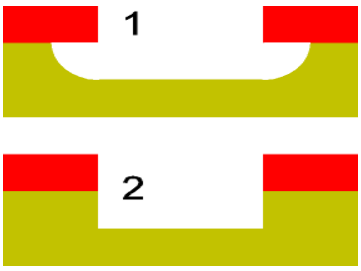

Figure 3 Isotropic (1) vs. non-isotropic (2) etch [6]

In order to eliminate or minimize attack of and damage to films or substrates, avoid modification of surfaces, promote contaminant removal rates and enhance process control, a number of approaches have been implemented[5]. The thinner films and smaller

feature sizes in current and future device structures also dictate that surface roughness must be minimized if reliable and controllable device properties are to be achieved. Such changes have dramatic ramifications for cleaning in that formulation of a simple, generic cleaning chemistry and approach for the >100 cleaning/residue removal/conditioning steps is not feasible. Customized individual cleaning steps that depend upon the composition of the films, impurities, residues, and substrates present, the sequences of steps preceding and following the cleaning, and the chemical nature of the specific surface are therefore being developed.

A number of different SiO_2 films are used in IC and MEMS devices: SiO_2 films are thermally-grown or deposited by CVD and plasma-enhanced CVD, with the deposited oxides often doped with boron (BSG), phosphorus (PSG), or both (BPSG). The oxides can be grown or deposited at temperatures ranging from 200 to 1100 C, and so have a range of densities, defects, and dopant concentrations which alter the etch rate in F-based solutions; considerable data have been collected on the etch rate of various types of films, especially the doped oxides [7-11]. Generally, P-doped films etch faster and B-doped films etch slower than undoped SiO_2, and the etch rate varies with P concentration; with BPSG, the etch rate depends upon the relative concentrations of B and P. In part, the difference in etch rates is believed to be due to the enhanced electron density at P sites relative to B sites. That is, after protonation of the hydroxyl group on the SiO_2 surface to form Si-OH_2^+, replacement of this group with F from various fluorinated species is facilitated by electron donation from the P and the etch rate increases. Obviously such electron donation is inhibited when B is present in the oxide lattice. A critical issue in IC and

MEMS fabrication is therefore how to obtain adequate selectivity between etching of different SiO_2-based films using HF-based solutions. If specific etchant species or conditions can be used to promote preferential interactions with different bonding structures in doped oxides, selectivity may be tailored so that control of cleaning/etching steps can be greatly improved.

For more than 40 years, aqueous solutions of hydrofluoric acid (HF) have been used to etch or remove SiO_2-based layers. Excellent reviews of the etching requirements, chemical solutions used, results obtained, and suggested etch mechanisms for these studies are available[7,8,12-17]; detailed discussion of the current understanding of SiO_2-based film etching in HF solutions will be presented in the chapters that follow. Until the late 1970s, aqueous HF solutions were used to etch patterns in SiO_2 and SiN_x layers; since that time, glow discharges or plasmas have been primarily used for pattern formation due to the need for anisotropic etch profiles in small device structures[18]. However, HF-based solutions are currently used extensively and will be used for the foreseeable future in micromachining or isotropic SiO_2 film removal and in post-plasma cleaning or resist removal for IC and MEMS fabrication processes [19]; use of these solutions is particularly prevalent in front end of line (FEOL) processes [13,16,17]. The relative etch rates of borophosphosilicate glass (BPSG) and thermally-grown SiO_2 (TOX) achievable in HF solutions is >5 depending upon HF concentration, which frequently results in the use of higher HF concentrations, leading to uncontrollable etch processes. Buffered HF (BHF) is typically used to alleviate this problem; however, due to problems

with surface roughness and non-uniformity of etch rate across the wafer, surfactant must be added [9,10,20,21]. For a surfactant-free solution, alternate chemistries are required

Even with the use of optimal chemistry to achieve the desired selectivity, the reactor geometry as well as process parameters such as concentration, flow rate and temperature can influence the overall performance defined in terms of etch rate (ER) variation across the wafer in a clean process. CFD simulations have been used in this thesis to design a reactor configuration in which the influence of these parameters on ER can be predicted. A laboratory-scale liquid HF reactor system has been assembled to verify these simulations and obtain experimental etch rate data. This reactor can be operated at short contact times (<1 sec). One immediate benefit of the short contact time concept is improvement of overall system throughput. In addition, this approach also allows the use of more concentrated chemistries that are not otherwise possible due to the constraint in film loss.

In-situ monitoring of optical constants and thicknesses of thin films is of interest when investigating the kinetics of film formation and etching as well as in process development for the fabrication of ICs, solar cells and MEMS devices [22-24]. A Spectroscopic Reflectometric (SR) technique has been used in this thesis to monitor in-situ film removal rates. Various 'state-estimation' techniques have been used to optimally extract the value of etch rate (ER) and thickness from in-situ real time acquired data. These predicted ER and thickness values can then be used to gain insight into reaction mechanisms.

The goals of this thesis are to improve cleaning/etching selectivities, efficiencies and effectiveness by performing

1) Investigations to further understand the chemistry of fluoride-based etch/clean solutions
2) Experiments on a laboratory-scale integrated wet etch/dry reactor with a configuration similar to that developed by LAM
3) Mathematical simulations to investigate the effect of process parameters on film etching and drying in the laboratory-scale reactor
4) In-situ measurements to provide improved monitoring for better process control

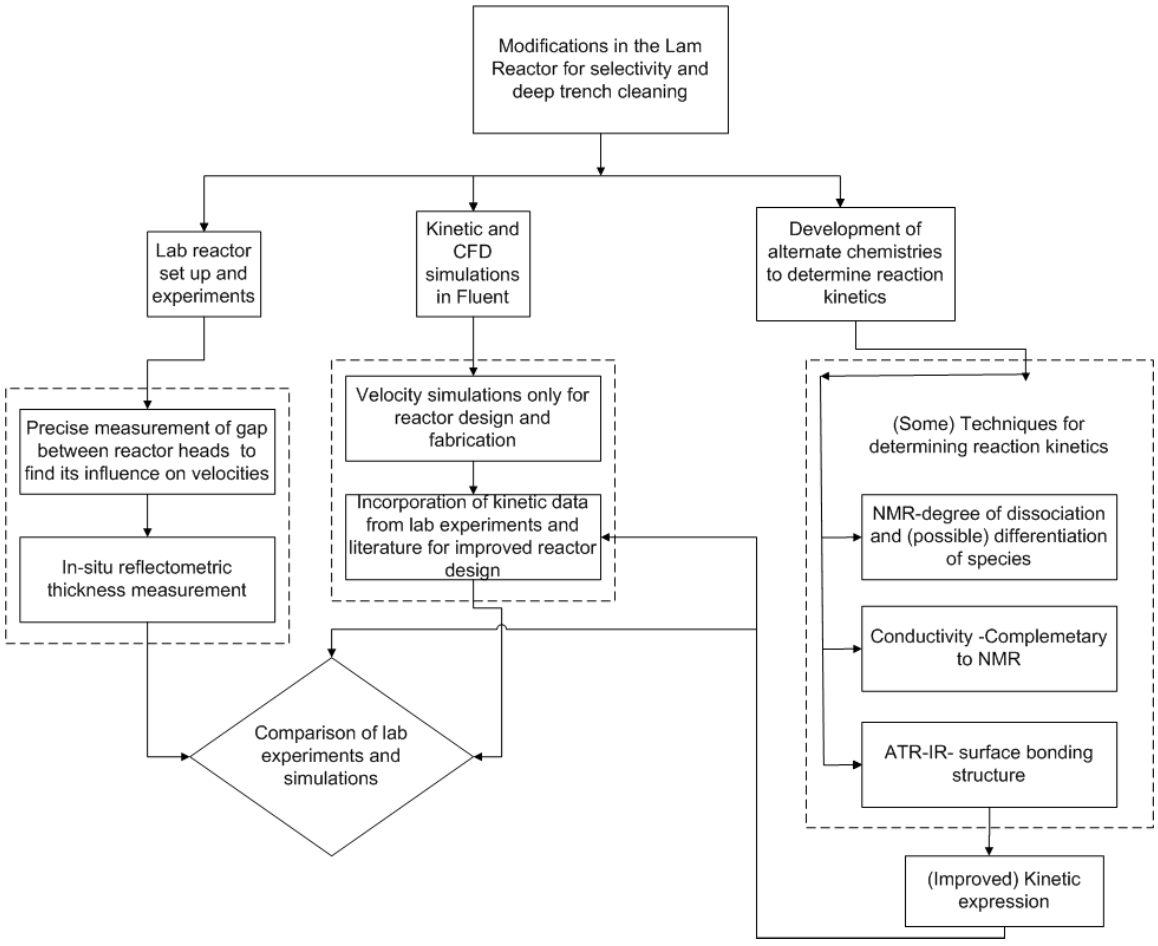

Figure 4 Overview of the thesis organization

The organization of this thesis is as follows. Chapter 2 introduces the background literature for etching of SiO_2-based films in fluorine-containing solutions. Chapter 3 describes the development of alternate chemistries for selective etching of BPSG as compared to TOX. Chapter 4 focuses on the design of a laboratory scale reactor using velocity (CFD) simulations. Chapter 5 deals with further refinement of this design by incorporating reaction kinetics into the CFD simulations. Chapter 6 describes the fabrication of a laboratory scale reactor and details the experimental configuration. Chapter 7 deals with the development of an in-situ optical sensor based upon reflectometry. Chapter 8 combines the ideas developed in Chapters 6 and 7 to investigate the ZnO-formic acid etching system that was used as a case study to explore the capabilities of this approach to etch rate measurements. Chapter 9 summarizes the findings of this thesis. Opportunities for future work are outlined in Chapter 10. Appendices are provided at the end of this thesis to offer further details regarding the approaches used in this work and to complement the understanding of material presented in the various chapters.

CHAPTER 2

BACKGROUND LITERATURE ON SiO_2 ETCHING IN AQUEOUS HF

[1]Due to the large number of publications over the past 50 years that address fluorine-based aqueous etching of SiO_2-based films, only selected references and review articles will be cited and the results summarized. Considerable work has also been performed using aqueous HF solutions with ammonium fluoride added (termed Buffered HF or BHF) to inhibit F^- depletion and ultimately stabilize SiO_2 etching characteristics (see, for example, Ref. [9,12,25-28]); again, only selected references will be supplied.

2.1 Solution chemistry

Two primary equilibria (Eqns (1) and (2)) have been used to describe the dissociation of the weak acid HF in water at concentrations <1 M.

$$HF \leftrightarrow H^+ + F^- \tag{1}$$

$$HF + F^- \leftrightarrow HF_2^- \tag{2}$$

Several other chemical equilibria have been postulated [29], [30], [31].

$$HF + HF_2^- \leftrightarrow H_2F_3^- \tag{3}$$

---

[1] Part of this chapter has been submitted for publication in IEEE trans. Semiconductor Manufacturing., 2010

$$H_2O + HF \leftrightarrow \left[\mathrm{H_3O^+ \cdot F^-} \right] \leftrightarrow \mathrm{H_3O^+ + F^-} \quad (4)$$

$$2HF \leftrightarrow (HF)_2 \quad (5)$$

Various arguments to support and to refute these equilibria have been offered. However, as noted previously [32], because (i) the exact chemical species present in solutions of HF have been difficult to measure, and (ii) the concentrations of the species present vary nonlinearly with initial HF concentration, the etch rate expressions are mostly empirical, with the dependence of etch rate on chemical species concentration determined by the best data fit to a specific mathematical expression. In these situations, no physical meaning of the etching process is evident.

2.2 General Etching Considerations

Even the overall etch reaction for SiO_2 in fluoride-containing solutions (no mechanism assumed) is not well-established. For instance, the accepted dissolution reaction is generally written as [10]

$$SiO_2 + 6HF \leftrightarrow H_2SiF_6 + 2H_2O \quad (6)$$

Early investigators concluded [25] that the etch reaction does not exclusively generate the hexafluorosilicate ion because this species can dissolve up to 20 mole % more SiO_2 than the original HF solution. However, other investigators have claimed that without addition of HF to the solution, H_2SiF_6 in water does not show observable etching of SiO_2 [7]. Subsequent studies have suggested that the final etch product is a molecule that contains at least two silicon atoms, i.e., decafluorodisilicic acid, produced according to [10]

$$4H^+(aq) + 5SiF_6^{-2}(aq) + SiO_2(s) \leftrightarrow 3F_4SiSiF_6^{2-}(aq) + 2H_2O \quad (7)$$

so that the overall etch reaction is actually

$$10HF(aq) + 2SiO_2(s) \leftrightarrow 2H^+(aq) + F_4SiSiF_6^{2-}(aq) + 4H_2O \quad (8)$$

and reaction (7) may be very rapid [10].

At pH ~7, the etch rate of SiO_2 has been reported to be near zero with F^- present in the unprotonated state, thereby precluding F^- as a primary etchant [25]. Other investigators [13] reported that aqueous NH_4F solutions do not etch SiO_2 and that above a certain molarity of NH_4F in HF, the etch rate of SiO_2 saturates. Etch rates correlated well with HF_2^- as NH_4F concentration was increased in HF solutions until the H^+ concentration was so low that protonation of the Si-O bond was inhibited, thereby limiting the etch rate [13]. Although a small SiO_2 etch rate was observed in KF solutions, a direct correlation between etch rate and HF_2^- concentration in KHF_2 solutions was noted [11].

From consideration of reactions (1) and (2) only, etch rate data were correlated to the following expression [25]:

$$R = A\ [HF] + B\left[HF_2^-\right] + C \quad (9)$$

However, at higher HF concentrations, polymeric species such as $(HF)_n$ have been suggested to play an important role [31]. Most of the subsequent etch rate correlations have modified rate expression (9) by adding and/or altering the specific terms and etch species, often by inclusion of some of the equilibria described by reactions (3) through (5) [7,11,33]. Agreement between modeling and theory is poor over a large concentration range because i) knowledge of chemical species is severely limited and ii) etch reactions occur

on the surface, thereby requiring kinetic expressions that accurately describe surface reactions.

2.3 Importance of H^+ in SiO_2 Etching Mechanism

Addition of strong acids (e.g., HCl) to HF solutions to alter pH, even at constant HF concentrations, increased SiO_2 etch rates [7,8,13,34,35]. A change in etch mechanism [13,25] correlated with the etch rate change at an H^+/HF_2^- ratio of ~0.02. Since the dependence of etch rate on HF_2^- concentration is different for HF and KHF_2 solutions at the same concentration of HF_2^-, K^+ and H^+ may play important roles in establishing the etch rate [11]. When strong acids were added so that $[H^+]$ was above 1-2 M, the etch rate was enhanced as a result of the catalytic role of H_3O^+ in the dissolution process, even though $[HF_2^-]$ was low [14]. Of the etchant solutions investigated, [14] those containing both HF and concentrated H_2SO_4 showed higher etch rates than did HF/HCl or HF/HNO_3 mixtures due to the formation of the strong acid HSO_3F. However, DF exhibited only a weak isotope effect and no isotope effect was observed for DF_2^-; thus, protons may not play a major role in the rate determining step in the etching reaction [36].

A number of pathways may be possible to form surface species that lead to Si-O bond rupture [7,37]. For instance, an HF molecule can react directly with the SiO_2 surface to cause Si-O bond breaking by association of F with Si and H with O. However, if reaction of hydrogen with the oxygen in SiO_2 to form hydroxyl groups is the first step in the etching process, then Si-O bond breakage may occur by two possible pathways: (a) hydroxyl group formation causes polarization and weakening of the underlying Si-O bond, thus facilitating Si attack by a fluoride species; (b) the hydroxyl group is replaced

by a fluoride ion, which results in weakening and ultimately breaking of the underlying Si-O bond. In a related approach, an etching model based on the effect of surface charge on the adsorption of solution species has been proposed [38].

Various other studies have led to the assumption that the adsorption processes of HF, HF_2^- and H^+ determine the etch rate [14], where HF_2^- adsorbs onto surface silanol groups, HF onto vicinal silanol groups and H^+ onto surface bridging oxygen atoms (siloxane units). Adsorption of electronegative species increases the electron density on the oxygen and leads to increased H^+ adsorption. Thus, the rate determining step is Si-O-Si bond breakage due to adsorbed species.

Since the SiO_2 etch rate displayed the same trends as did HF_2^- and $(HF)_2$ species concentrations while [HF] and $[F^-]$ followed different trends, HF_2^- and $(HF)_2$ were assumed to be the primary etchant species in Quartz Crystal Microbalance (QCM) studies [15]. A two-step reaction mechanism was therefore proposed: protonation of a surface oxygen atom bonded to a silicon atom (to release OH^- and H_2O from the surface to form the reactive intermediate) followed by nucleophilic attack of Si by HF_2^- or $(HF)_2$ as shown in Figure 5 to Figure 7 [15]. The pKa value of the deprotonation reaction increases due to the buildup of surface charge at pH > 4. Consequently, the concentration of SiOH surface groups and the etch rate are higher than expected from a simple acid/base equilibrium reaction. All subsequent reaction steps to remove the Si-F unit from the SiO_2 matrix are fast reaction steps (>10X faster than protonation) that involve HF_2^- addition reactions on F_xSi-O bonds.

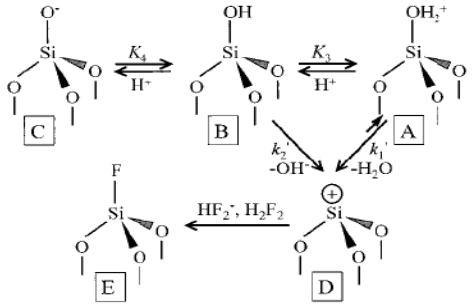

Figure 5 Proposed reaction mechanism for the rate determining step of SiO_2 dissolution; replacement of an SiOH unit by an SiF unit [15]

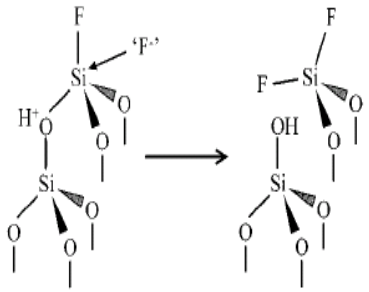

Figure 6**.** Nucleophilic substitution reaction to remove SiF unit [15]

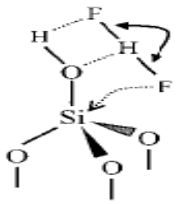

Figure 7. HF_2^- assisted OH^- elimination reaction with consecutive F^- addition [15]

CHAPTER 3

FORMULATION OF SELECTIVE ETCH CHEMISTRIES

A critical issue in IC and MEMS fabrication is how to obtain adequate selectivity between etching of different SiO_2-based films using aqueous HF-based solutions. If specific etchant species or conditions can be used to promote preferential interactions with different bonding structures in doped oxides, selectivity may be tailored so that control of cleaning/etching steps can be greatly improved.[2]

In this chapter, we investigate the possibility of achieving selectivity of BPSG ER /Thermal oxide (TOX) ER close to unity. Although several previous studies have addressed this issue [9,10,20,21], surface roughness, non-uniformity of etch rate across the wafer, and the need for surfactant addition limited the ability to achieve selectivities near 1. Some studies [39] have invoked a relatively complicated etch chemistry (with 4 or more components) that may present a challenge to implement in manufacturing processes. The chemistries developed here have only three components and have uniform etch rate across a wafer while maintaining sufficient ER to ensure adequate throughput in manufacturing processes.

---

[2] Part of this chapter has been published in J. Electrochem. Soc., 157(6), G147-G153, 2010

3.1 Chemicals

TetraButylAmmonium BiFluoride (TBABF, >95%), TetraButylAmmonium Fluoride (TBAF,>98%), N-methylformamide (>99%, GC), TetraButylAmmonium Dihydrogen Trifluoride (TBADT>90%), TetraEthylAmmoniumFluorideTriHydroFluoride (TEATHF) and TetraEthylAmmoniumFluorideTetraHydroFluoride (TEATetraF) were obtained from TCI America. NH_4HF_2 and $NaHF_2$ were obtained from Climate Neutral (technical grade, >95% purity). KF (reagent grade, 98%),KHF_2 (99%), H_2SiF_6 (technical grade 33.5-35%), propylene carbonate (HPLC, 99.7%),and N,N dimethyl acetamide (>99.9%, HPLC) were obtained from Sigma Aldrich.D_2O(Wilmad LabGlass, >99.9%), Toluene (Fluka, GC, 99.5%) N-methyl-2-pyrrolidone(Riedel de Haen, GC, 99.5%) Hydrogen peroxide (Fisher, 30%) and HF were obtainedfrom J.T.Baker (ACS reagent, 48-51%). Formamide (>99.9%) Tetrahydrofuran (THF)(B&J Brand 99.9%) and Dimethylsulfoxide (DMSO) (ACS grade, 99.9%) were obtainedfrom VWR.All chemicals were used as received without further purification.

3.2 Substrates

Thermally grown SiO_2 (TOX) or BPSG obtained from Lam Research Inc. were the film materials studied. Etch rates of TOX and BPSG in aqueous HF solutions were used as the criterion to determine the quality of TOX and to compare with literature values; rates are shown in Figure 8. The boron (1.13-5.16 wt%) and phosphorus (2.46-3.52 wt%) content of BPSG wafers was characterized by Energy Dispersive Spectroscopy (EDS) using a Leo 1530 Thermally-Assisted Field Emission (TFE) Scanning Electron Microscope (SEM). It was observed that the phosphorus concentration had less variation within the

sample as compared to the boron concentration. This observation was consistent from sample to sample. The same batch of wafers was used for all ER experiments.

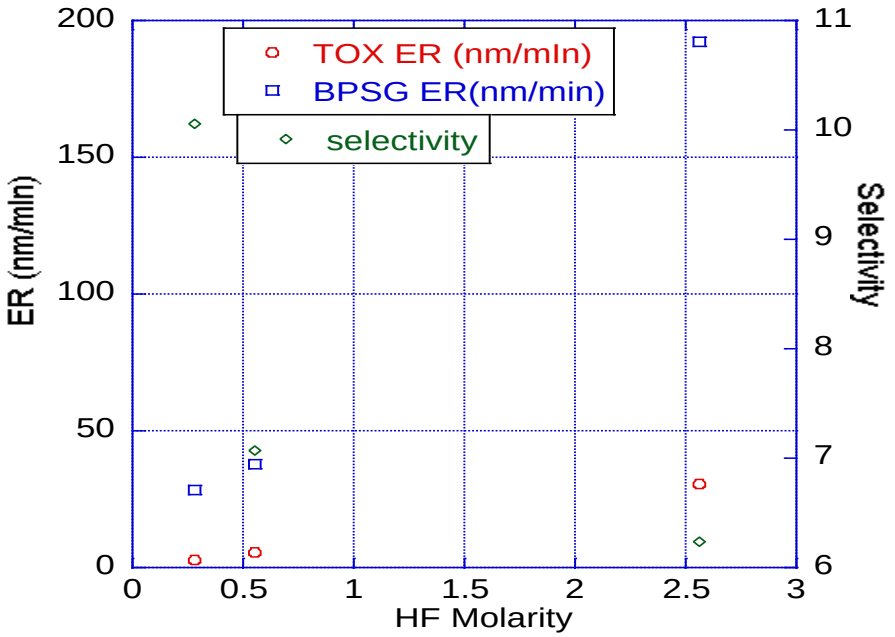

Figure 8 Selectivity and etch rate dependence on aqueous HF solution composition

3.3 Etch rate (ER) measurements

For ER measurements, samples of 1cm*1cm size were used. These samples were immersed into salt solutions of specified concentration and the solution stirred. After etching for a certain time, samples were rinsed in DI water and oxide thicknesses measured using a J. A. Woollam M2000 ellipsometer. Total etch times for each sample were at least 9 min and in some cases, where ER was very low, times up to 30 minutes were used. The transfer time between etching and rinsing of samples was kept to a minimum (<2 sec). The effect of solution volume and stirring were also investigated. Volumes > 10 ml avoided etchant depletion effects (the thickness vs. time data was

linear) and the stirring rate was unimportant over the range of conditions studied (stirrer rotation rates up to 300 rpm were investigated). The accuracy of salt solution volume measurements was 0.1 ml and the accuracy for salt weight measurements was 1 mg.

All experiments were repeated at least twice and the average of the film thickness obtained is reported for a given concentration at a given time. There are two ways to define ER.

1. The slope of a plot of etched thickness vs. time with a straight line fitted to the data by linear least squares regression. In this case, the line need not pass through the origin (may not have zero intercept).
2. The slope of a plot of etched thickness vs. time with the straight line passing through origin (zero intercept required).

For results reported in this thesis, the ER is determined according to definition 1 unless specifically noted otherwise. In addition, we should note that a non-zero intercept of ER data is not necessarily an experimental error as has been reported previously[10,28], since adventitious contaminants could alter initial ERs.

A few selected substrate samples (TOX and BPSG) were cleaned in piranha solution (5 vol 98% H_2SO_4 : 1 vol 30% H_2O_2) at 120^0 C for 30 min. After cleaning, they were rinsed in DI water and dipped in 1:10 HF solution for 5-8 sec to remove a thin layer of oxide and rinsed again. Samples were dried using HP N_2, the thickness measured, and the ER experiments performed in aqueous salt solutions as described in the next section. The maximum time lag between the HF dip and the ER measurement was 15 min. Results

indicated that the ER of samples after cleaning is higher than that without a cleaning treatment in most cases; the maximum difference observed was 0.5 nm/min. Also the difference in etched thickness was detected only at longer etch times (>6 min). Many of the data points (>80%), especially at shorter times, for the two cases (cleaned vs. no cleaning treatment) were within experimental error. Due to the minor differences in ER observed, experiments were therefore performed without a pre-etch cleaning step. The values of ER reported here should therefore be considered as lower limit, although the maximum difference observed was 0.5 nm/min.

Since DMSO and THF can both contain moisture as an impurity, solution compositions at ~0.05 mole fraction water (the importance of mole fraction of water is discussed below) was prepared using fresh THF and DMSO. For all other compositions, DMSO and THF that had been stored in a glove box were used. A Karl Fisher analysis was performed on these solvents and the water content was <0.3 wt% for both solvents. Since this value is negligible relative to other concentrations used, it is not considered in concentration calculations.

3.4 NMR

For NMR experiments, a capped Teflon NMR liner tube (Wilmad, Inc.) was used inside a 5mm OD NMR glass tube in a Varian Mercury 400 instrument. The low temperature experiments were performed in a Bruker DRX-500 NMR. D_2O was used as a locking solvent as well as the solvent for salts (specific issues regarding solvents are discussed in the next section). Locking is simply the adjustment of the deuterium lock field (Z0) such that the deuterated solvent's resonance (the deuterium signal) is centered on a predefined

lock frequency. The spectrometer uses this information in order to compensate for any magnetic field drift (i.e. small loss over time of field strength). Without this drift compensation, sample peaks would appear at a different frequency over time leading to peak broadening. Modern NMR magnets generally do not drift more than a few Hertz per hour, which is small relative to the overall field (only 0.01 ppm at 500 MHz). No internal standard reference was used. However, experiments were repeated to ensure that chemical shift differences between successive runs were <0.01 ppm.

3.5 Results and discussion

3.5.1 Initial Characterization of aqueous HF solutions

Since knowledge of the effect of concentration of the different chemical species on film ER will assist in the investigation of etch mechanism and thus selectivity, initial characterization studies of the aqueous HF solutions were carried out to establish if the individual chemical species could be detected via NMR or FTIR. As shown in Figure 12 ,infrared spectroscopy studies of 1:100 HF:H_2O solution did not allow this differentiation. ^{19}F NMR indicated that with increased HF concentrations, more negative values of chemical shift were observed. In addition, only one peak (in the range of -159.2 ppm- -161.0 ppm) was detected, which was relatively broad at lower concentrations and narrower at higher concentrations as shown in Figure 9 to Figure 11. Similar results were observed for ^{1}H NMR spectra. Values of the chemical shifts observed were in agreement with those reported previously [40]. Even at lower temperatures (~265 K), F species differentiation was not possible in aqueous systems.

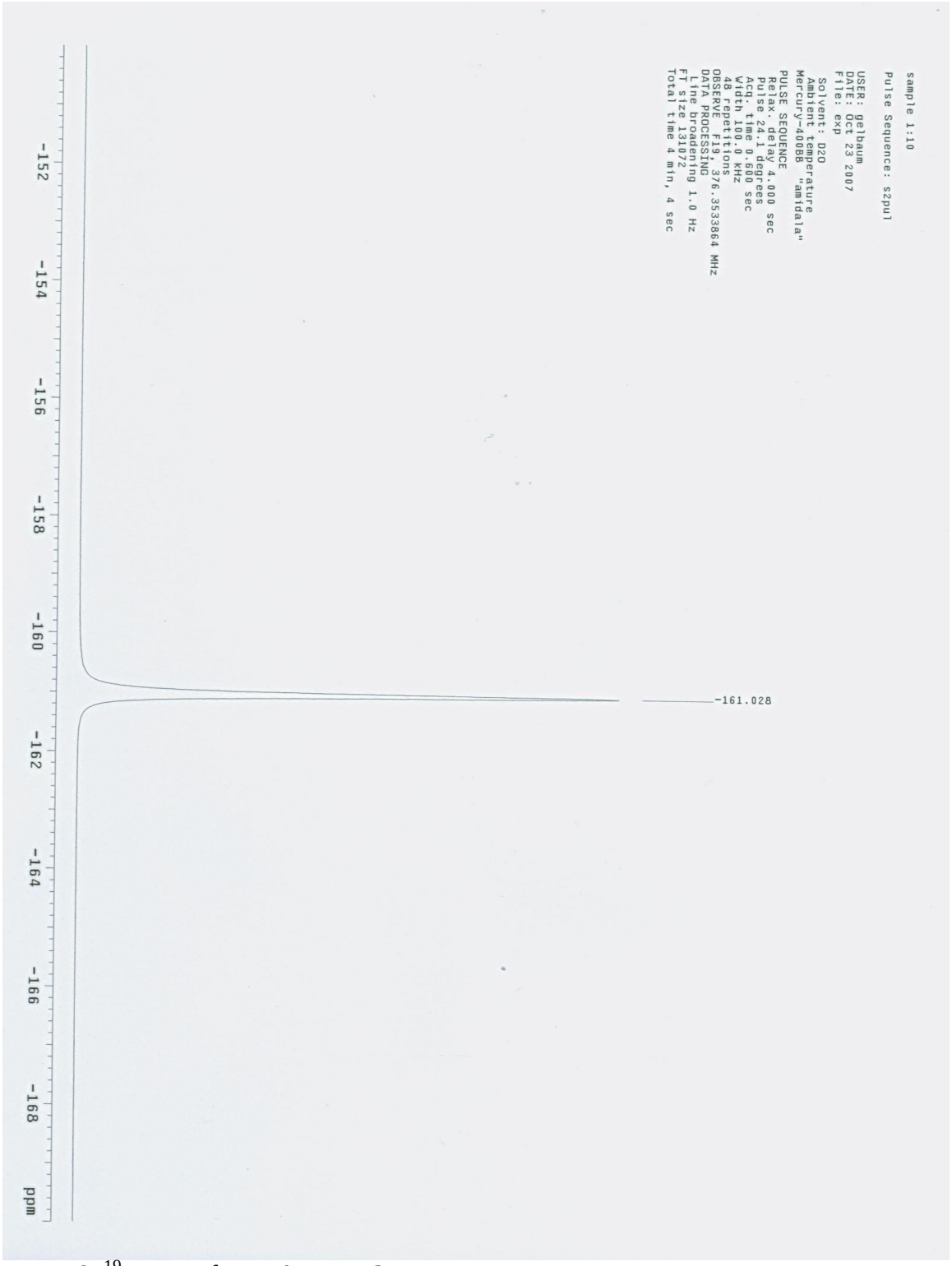

Figure 9 ^{19}F NMR for 1:10 HF:H_2O

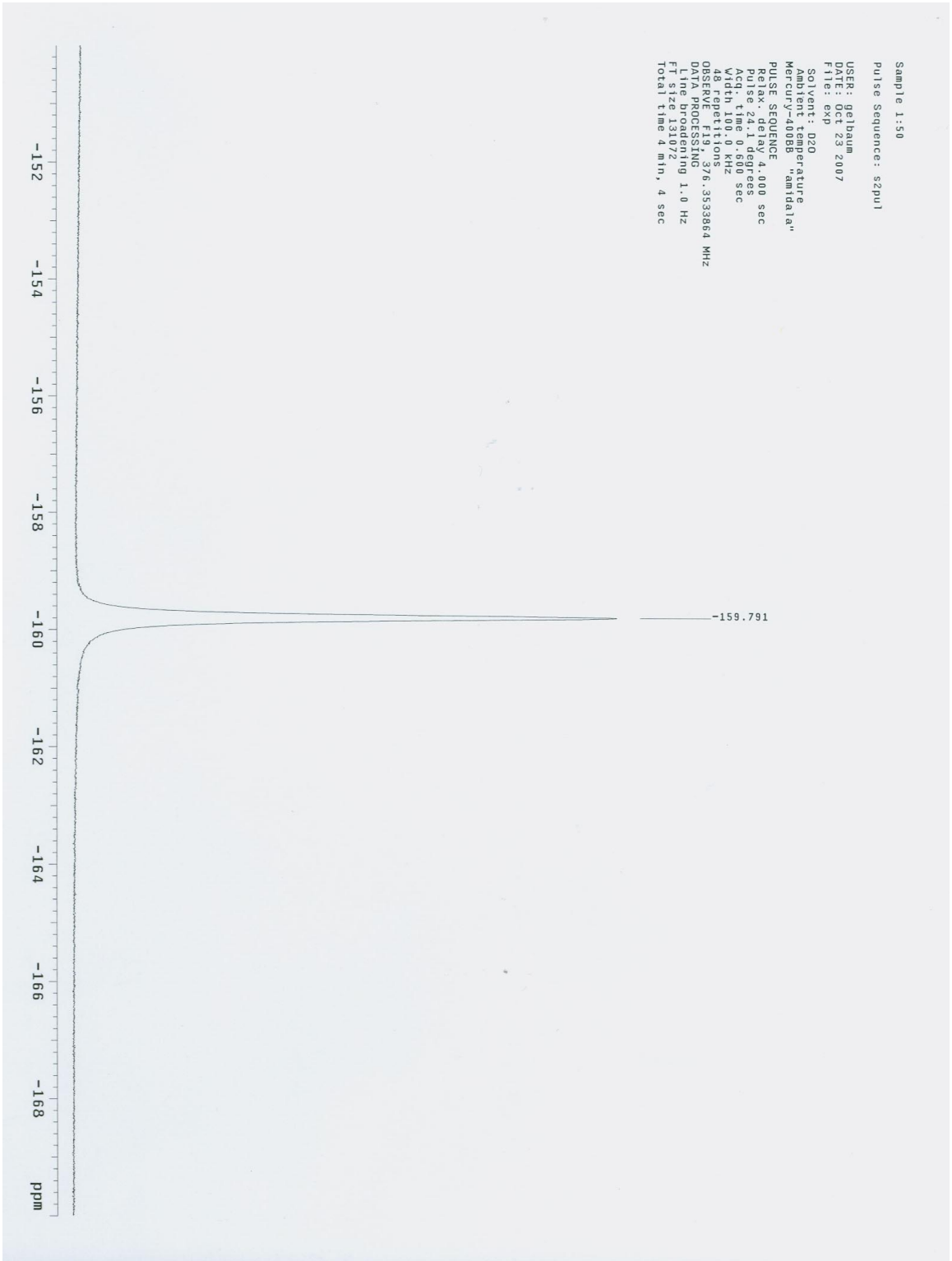

Figure 10 ^{19}F NMR for 1:50 HF:H_2O

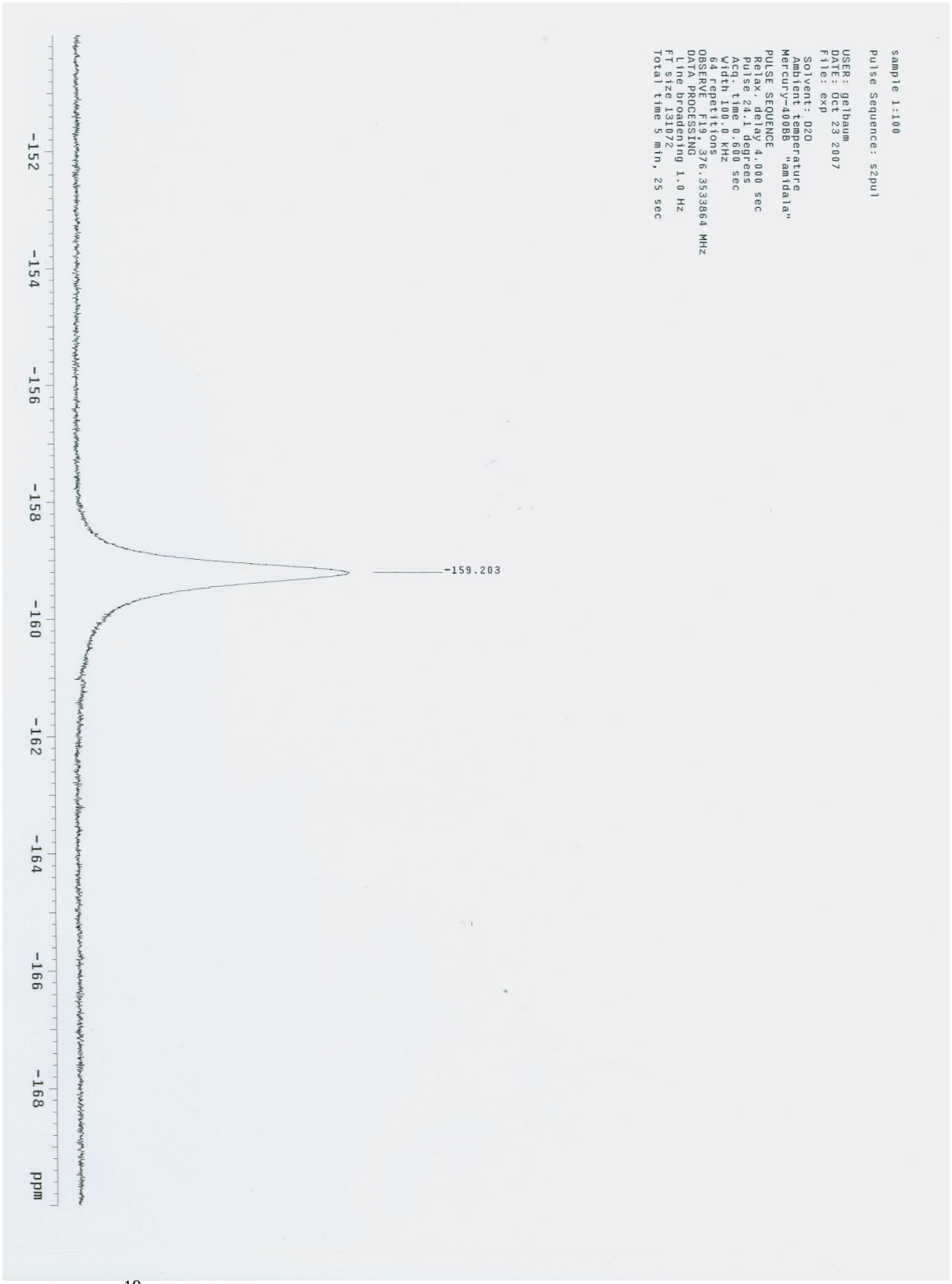

Figure 11 ^{19}F NMR for 1:100 HF:H_2O

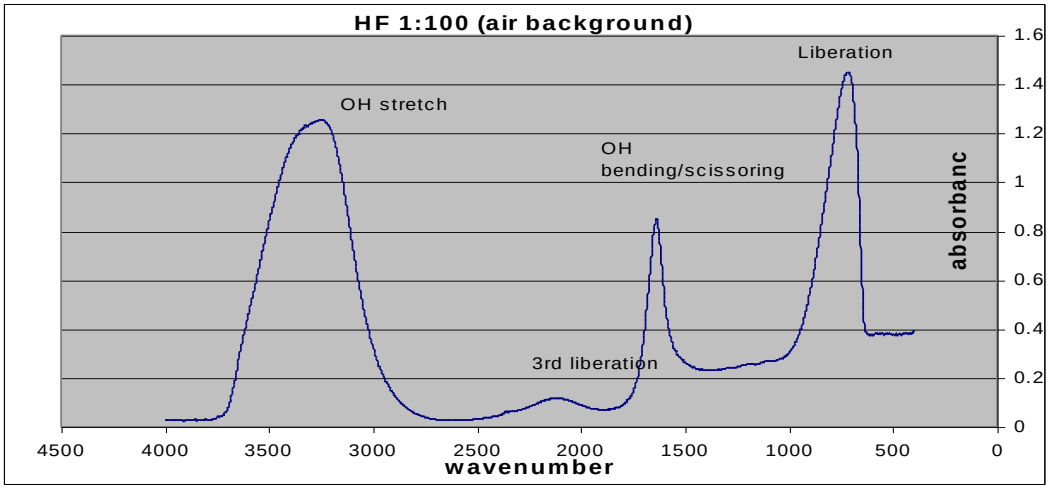

Figure 12 FTIR for 1:100 HF:H_2O solution with air as background, 3rd Liberation is overtone/combination liberation HOH bend, wavenumber in cm^{-1}

3.5.2 Use of organic solvents

Although water is an extraordinarily versatile solvent, the numerous equilibria existing in aqueous solutions of HF complicate the investigation of etch mechanisms and solution species dependencies. Thus, non-aqueous solutions are proposed to control desirable equilibria and tailor etch rates and selectivity. A decrease in the solution dielectric constant should increase the attractive force between dissociated species so that dissociation decreases. Indeed, addition of a relatively low dielectric constant solvent such as isopropyl alcohol (IPA) to HF decreases the etch rate of SiO_2 relative to HF/water solutions [41]. Since HF_2^- is the etchant species for SiO_2, the formation of HF_2^- is apparently inhibited by decreasing HF dissociation. By comparison, in HF/water/ethanol solutions, HF and HF_2^- predominate in dilute HF solutions, whereas HF and higher degree polyhomoconjugated species, $(HF)_nF^-$, predominate in concentrated HF solutions [42].

3.5.3 Strategy for Using F-based Organic Salts

Various fluorine-containing commercially available salts are proposed that can generate the same etchant species as those in aqueous HF solutions when dissociated (We have avoided the use of anhydrous HF due to safety concerns). The salts selected have TetraButylAmmonium (TBA) as the cation and Fluoride (F)/BiFluoride (BF) /Dihydrogen Trifluoride (DT) as anions. Organic salts have been implemented since inorganic salts such as KHF_2 are not readily soluble in organic solvents such as DMSO. Another major factor in the use of organic salts is the compatibility of the cations with IC manufacturing processes. Furthermore, when changing from tetrabutylammonium to tetrabutylphosphonium, salts with a common anion display identical solvation properties [43]. Hence, with these cations, the solvent properties are dominated by the choice of anion. H^+ has been shown to have an important effect on the SiO_2 etch reaction mechanism [7,8,13]. Therefore, cations with acidic protons, such as trialkylammonium and trialkylphosphonium that can affect the ER directly and thereby further complicate the reaction mechanism, were not included. Finally, ER studies using KHF_2, NH_4HF_2 and $NaHF_2$ in the concentration range 0-1 M in aqueous solution demonstrated that the ERs differ by less than 1 nm/min for the same concentration.

3.5.4 Effect of solvent dielectric constant

Initial ^{19}F NMR studies using mixtures of 1M TBAF and TBABF in THF established that HF_2^- and F^- can be individually detected. Thus a number of organic solvents were chosen for study. The solvent selected should have a high dielectric constant and should be aprotic in order to separate the effect of H^+ in the etch mechanism as described above. Common solvents that meet this requirement are dimethyl sulfoxide (dielectric constant ≡

ε = 47.2), dioxane (ε = 2.2), acetonitrile (ε = 36.6), toluene (ε = 2.4) and tetrahydrofuran (THF) (ε = 7.52). Since acetonitrile is unstable in the presence of fluoride [44], this solvent was not considered further. Because the presence of low ε organic solvents should generate lower HF_2^- concentrations, etch rates should decrease. Furthermore, salt dissociation should therefore be tailorable with solvent choice. In addition, since solvent dielectric constant also plays an important role in interionic associations, etch rates and thus selectivities may be further tuned.

Table 1 shows the effect of changing dielectric constant using various solvents on TOX etch rate. Obviously, no clear correlation between ER and ε was observed, indicating that this parameter is not the only factor that establishes etch rates. In Table 1, when no ER is listed, this indicates that the ER value is too low (<0.1 nm/min) to be accurately measured.

Table 1. Etch rate of TOX for different solvents in 0.5 molal solution of TBABF

	Solvent	Dielectric constant	ER (nm/min)
1	Toluene	2.385 (20° C, [45])	-
2	N,n dimethyl acetamide	37.78 (25° C, [45])	-
3	D_2O	78.3 (25° C, [46])	3.82
4	Formamide	111 (20° C,[45]	0.31
5	Hydrogen peroxide	83.1 (35.3wt%, 20^0C, [47])	7.50
6	N-methylformamide	182.4 (25° C,[48])	-
7	Propylene carbonate	66.14 (20° C, [45])	-
8	N-methyl pyrrolidone	32.0 (25° C, [49])	-

3.5.5 Consideration of polar protic solvents

As described previously [15] and indicated in Figure 13, the reaction of HF with SiO_2 is a two step reaction: protonation of a surface oxygen atom bonded to a silicon atom (to release OH^- and H_2O from the surface to form the reactive intermediate) followed by nucleophilic attack of Si by HF_2^-. In the reaction of $HF_2^-/H_2F_3^-$ anions with SiO_2, the polar part of the solvent should stabilize an ionic intermediate (such as that labeled D in Figure 13) and the protic part should solvate the leaving group of OH^- or H_2O. Organic salt solutions in organic solvents such as DMSO and THF show very low ER for TOX and BPSG, indicating that these polar aprotic solvents cannot solvate the leaving group. Thus a polar protic solvent was considered for this application. While a number of polar protic solvents exist, water was used because of its versatility. In this study, water composition was systematically varied over the concentration range from 0-~0.9911 mol

fraction. In order to alleviate the control issues associated with the transfer of solute (salts) from/to the organic phase and to/from the aqueous phase, DMSO and THF which are completely miscible with water but differ in dielectric constant, were chosen as the organic solvents. It should be noted that addition of water complicates the investigation of etch mechanism as described previously. Although water allows achievement of reasonable ERs (>1 nm/min), addition of a protic solvent to aprotic solvent not only changes the reaction rate, but may also affect the etch mechanism [50].

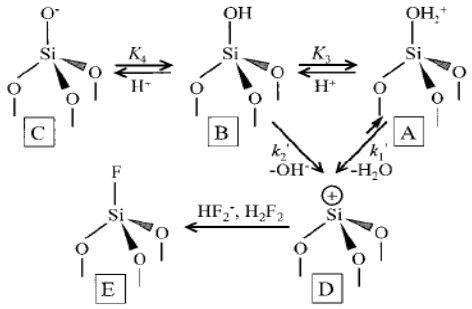

Figure 13 Proposed reaction mechanism describing the rate determining step for SiO_2 dissolution; replacement of an SiOH unit by an SiF unit [15]

3.5.6 ER of aqueous/organic salt mixtures

As shown in Figure 14, the TOX etch rate decreases rapidly with a decrease in water mole fraction in TBABF and TBADT solutions; in contrast, with aqueous HF solutions ER increases with an increase in water mole fraction. It should be noted that the ER in Figure 14 is plotted as an independent variable; i.e., water mole fraction values (and corresponding salt mole fractions) are those at a constant ER. This graph allows determination of the mole fraction of salt needed for a specific ER. The salt mole fraction

is fixed at 0.0089, a value selected from Figure 14, where upon a slight change in water mole fraction (but little change in salt mole fraction), the etch rate increases drastically. This observation is not due to ER sensitivity to experimental errors, since the extra mass of salt needed to achieve this change in mole fraction is much greater (>0.1 g) than the accuracy of the balance (1mg) used to weigh the salt.

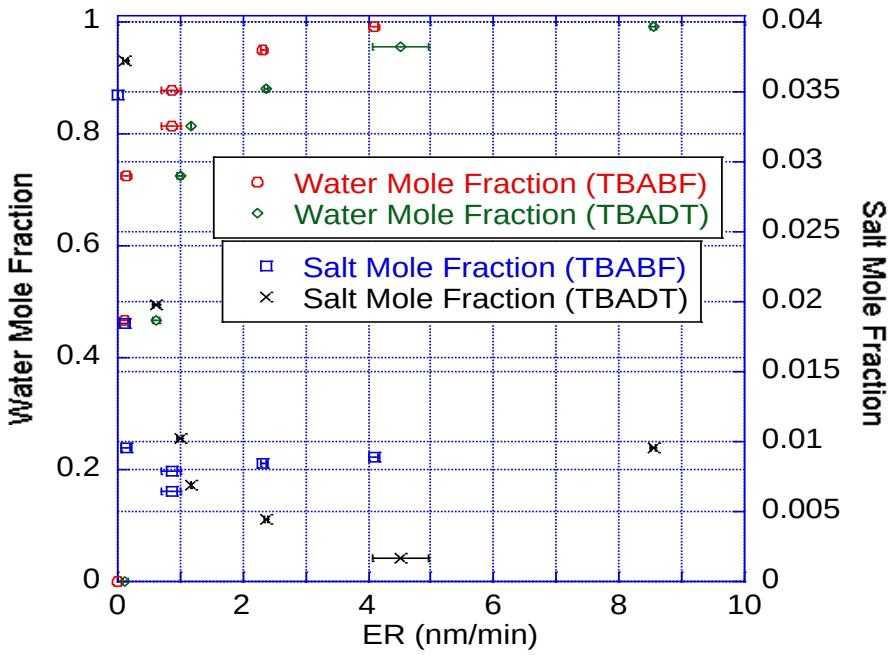

Figure 14 Dependence of etched thickness of thermal oxide (TOX) on water and salt mole fractions for TBABF and TBADT

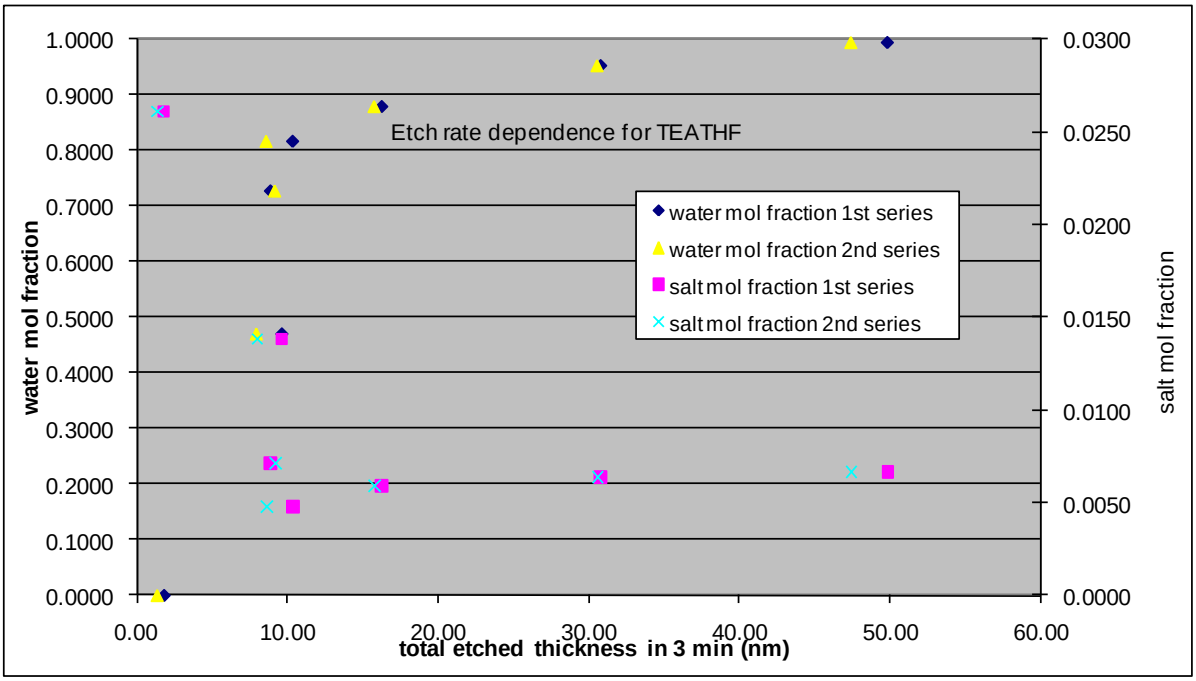

Figure 15 Dependence of etched thickness of thermal oxide (TOX) on water and salt mole fractions for TEATHF

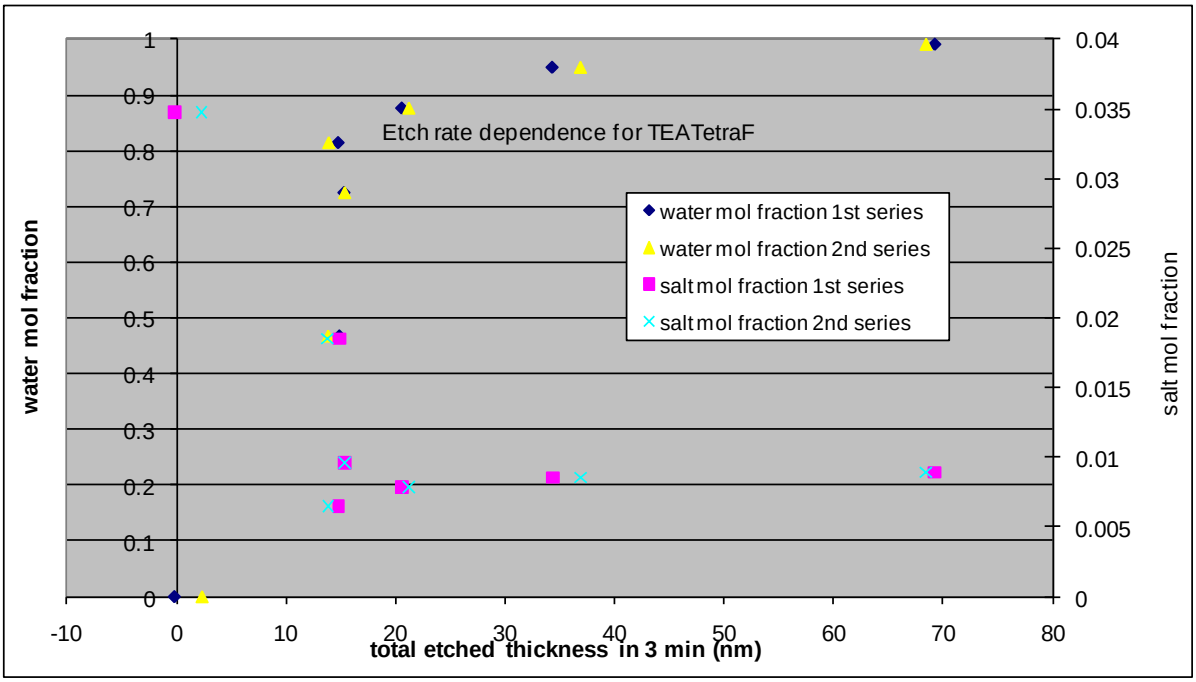

Figure 16 Dependence of etched thickness of thermal oxide (TOX) on water and salt mole fractions for TEATetraF

Figure 15 and Figure 16 show the etched thickness of thermal oxide on salt and water mole fractions for TEATetraF and TEATHF which follow a similar trend as that of TBABF. Figure 17 and Figure 18 show the effect of water mole fraction on ERs of TOX and BPSG respectively for TBABF and TBADT salt solutions in THF or DMSO. A rapid increase in etch rate at a water mole fraction ~0.8 is observed. This trend may not be due to the effect of dielectric constant alone since the dielectric constant relationship for both DMSO-water mixtures and THF-water mixtures is linear [51,52]. Rather, the increase in ER is probably due to either 1) formation of new species in the bulk solution or 2) change in the reaction mechanism at the film surface. Possibility 1) is not likely since there is no evidence of additional species present according to the NMR results displayed in Table 7. Since NMR is sensitive to the solution contained within the primary solvation shell [53], we

conducted NMR studies to qualitatively describe the ER variation; these studies will be described in the next section. Possibility 2) can be verified using an FTIR cell as described in the future works section.

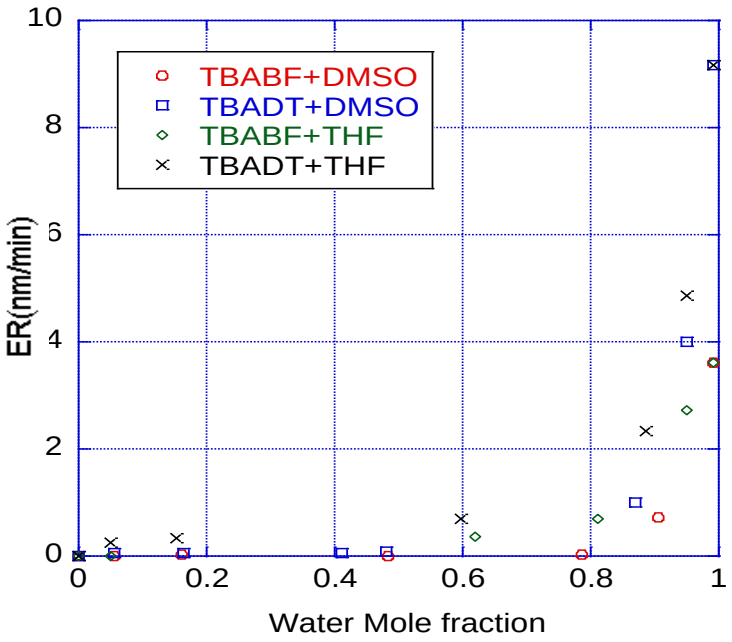

Figure 17 Dependence of etched thickness of Thermal oxide (TOX) on water mole fraction for 0.0089 mol fraction TBABF/TBADT in DMSO/THF

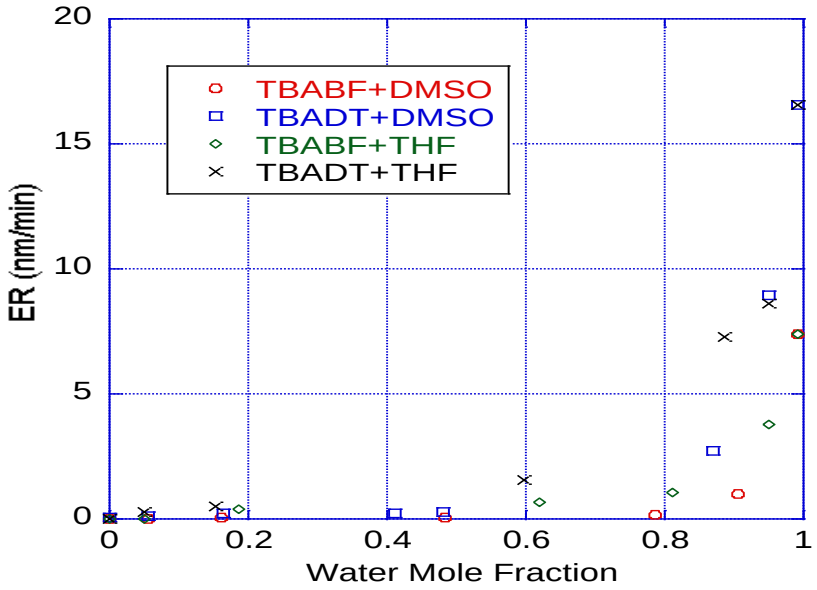

Figure 18 Dependence of etched thickness of BPSG on water mole fraction for 0.0089 mol fraction TBABF/TBADT in DMSO/THF

Etch rates with TBADT were always greater than those of TBABF. These trends are consistent with previous studies [54] which indicate that higher ionic species such as $H_2F_3^-$ contribute more prevalently to etch rates at higher aqueous HF concentration if neutral polymeric species, e.g., $(HF)_2$, formation is neglected. Such observations indicate that the relative concentrations of the various chemical species present at specific concentrations of aqueous/organic mixtures is therefore crucial for the establishment of etch rates and for selectivity control.

Figure 20 shows the ER variation for TOX and BPSG as well as selectivity for these films in TBABF-water solutions; Figure 21 shows a similar plot for TBADT-water solutions. It was observed that a selectivity of 2.0 is easily achieved at >0.5 molar

concentration of these salts in water, with selectivity decreasing even further below this value with increasing molarity for TBABF. For TBADT, the selectivity remains nearly constant after 0.5 molar. The limited solubility of TBADT in water (as indicated by the formation of a turbid solution) prevented the collection of data at higher TBADT molarity. The intercept for the data in Figure 20 and Figure 21 is <0.5 nm and therefore is not reported. The presence of a maximum in the ER for TOX and BPSG in Figure 20 has been reported previously [9,28] in buffered HF (BHF) solutions. Similarly, the initial increase in ER can be explained by increasing HF_2^- concentration at increased TBABF molarity. The subsequent decrease is likely due to co-ordination and/or blocking of TBA^+ cations with HF_2^- at even higher TBABF molarity, analogous to results reported for etching is solutions of BHF as shown in Figure 19.

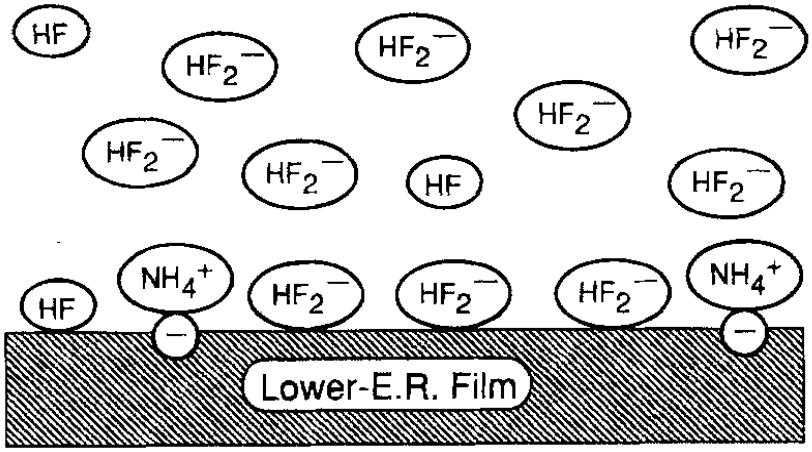

Figure 19 NH_4^+ blocking model as proposed by Kunii [28]

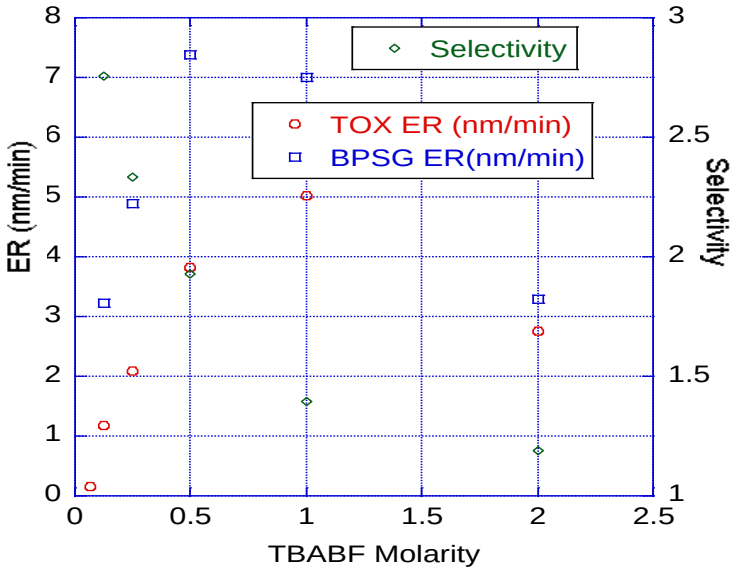

Figure 20 ER and selectivity variation for TOX and BPSG in TBABF + water solution

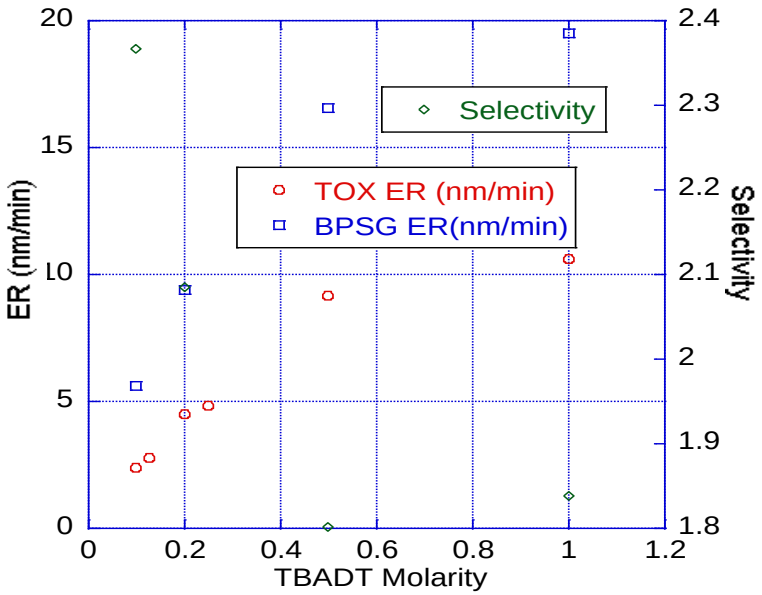

Figure 21 ER and selectivity variation for TOX and BPSG in TBADT + water solution

Due to the very small ER in the region 0-0.8 mol fraction of water in Figure 17 and Figure 18, the selectivity calculation is highly sensitive to small variations in experimental results, since even a small change in etch rate of either film leads to a large change in selectivity. Also, we have observed that in some cases, the intercept value is as large as the ER (slope) itself i.e. the intercept cannot be neglected, especially at lower ER. In the case of low concentrations, this result may be primarily due to depletion of reactants. If the ER is determined by definition 2 in Section 2.3 (ER regression line passes through the origin), selectivities are essentially always less than those determined by definition 1. The linearity of plots of etched thickness vs. time, as determined by R^2 values, is improved for both salts in THF and water solutions at water mole fractions <0.8. DMSO solutions in the same range show lower R^2 values. This may be due to the slow changes in solvation of anions in the reaction environment. Indeed, it has been reported [55] that rearrangement of hydrogen bonded water networks in a water saturated nitrobenzene solution leads to slow changes in solvation; this possibility can be evaluated by using an ATR-FTIR cell as described in the future work section. Also, the linearity of the plots improves with increasing water mole fraction for both salts in THF and DMSO. These results are summarized in Table 2 to 5, where the intercept is also reported as noted in previous studies[10]. All experiments were conducted at a constant TBABF/TBADT mole fraction of 0.0089; from the water mole fraction, the DMSO mole fraction can be calculated. The last entries at 0.99 mole fraction of water represent the situation where no organic solvent was added. R^2 values that are missing in the tables indicate that the etched thicknesses did not follow a linear trend or the R^2 values were

low (<0.4). We note that for a mole fraction of water >0.8, a selectivity of 1.5 – 2.0 can be achieved. However, due to the rapidly increasing etch rates in this regime, selectivity values are sensitive to experimental errors.

Table 2 Etch rates for TBABF solutions in water and DMSO (TBABF mole fraction =0.0089)

	TOX ER	BPSG ER	intercept	R^2	Intercept	R^2
water mole fraction	(nm/min)	(nm/min)	TOX		BPSG	
0	0	0	0	-	0	-
0.0551	0	0.02	0	-	0.05	0.48
0.1624	0.03	0.07	0	-	-0.35	0.96
0.4837	0	0.05	0.66	0.96	0.63	0.50
0.7853	0.02	0.18	0.52	0.88	1.09	0.98
0.9050	0.73	0.98	3.50	0.99	2.99	1.00
0.9911	3.62	7.38	3.06	1.00	5.93	0.96

Table 3 Etch rates for TBABF solutions in water and THF (TBABF mole fraction =0.0089)

	TOX ER	BPSG ER	intercept	R^2	Intercept	R^2
water mole fraction	(nm/min)	(nm/min)	TOX		BPSG	
0	0	0	0	-	-	-
0.0513	0	0	0	-	-	-
0.1873	0	0.41	0	-	1.03	1.00
0.6204	0.37	0.65	0	0.99	1.32	1.00
0.8125	0.70	1.06	0	0.99	1.75	1.00
0.9494	2.72	3.79	0	0.99	3.08	1.00
0.9911	3.62	7.38	3.06	1.00	5.93	0.96

Table 4 Etch rates for TBADT solutions in water and DMSO (TBADT mole fraction =0.0089)

	TOX ER	BPSG ER	intercept	R^2	Intercept	R^2
water mole fraction	(nm/min)	(nm/min)	TOX		BPSG	
0	0	0.05	-	-	0	-
0.0551	0.06	0.1	0	-	0	-
0.1627	0.07	0.22	0	-	-0.31	0.93
0.4105	0.06	0.23	0.06	0.93	-0.28	0.76
0.4809	0.09	0.28	0.77	0.89	0.91	0.96
0.8707	1.01	2.74	1.38	0.99	-3.63	0.98
0.9510	4.00	8.94	3.55	1.00	-4.01	1.00
0.9911	9.18	16.54	-1.26	1	9.27	1.00

Table 5 Etch rates for TBADT solutions in water and THF (TBADT mole fraction =0.0089)

	TOX ER	BPSG ER	intercept	R^2	Intercept	R^2
water mole fraction	(nm/min)	(nm/min)	TOX		BPSG	
0	0	0	-	-	-	-
0.0513	0.26	0.30	-0.71	1.00	-	-
0.1527	0.32	0.51	-1.11	0.89	0.96	0.94
0.5974	0.69	1.54	-0.26	1.00	-1.64	1.00
0.8855	2.34	7.26	0.61	1.00	0.35	1.00
0.9494	4.85	8.62	6.97	1.00	0	1.00
0.9911	9.18	16.54	-1.26	1.00	9.27	1.00

3.5.7 NMR studies of aqueous/organic solvents containing organic salts

In an effort to gain more insight into the etch mechanism, we conducted ^{19}F NMR studies. Peak positions were verified from those reported previously [40]. In Table 6 - 8,, the values in parentheses correspond to the areas under the curve.

Considering the NMR peak positions for HF_2^- and F^- in Table 6 , it is clear that the peak for the mixture is between the positions of the two individual peaks. Comparison of the peak position of $H_2F_3^-$ in TBADT (~ -156 ppm), to peaks for a mixture of TBA-based salts indicates that the peaks are again located between the positions of the two individual peaks. This averaging of peak positions may be due to anion exchange between the fluoride species.

Table 6 Peak positions for various salts (0.5 molal) in D_2O for ^{19}F NMR (values in parentheses indicate area under the peak)

	Salt	Peak 1 (ppm)	Peak 2 (ppm)
1.	KF / TBAF, various conc.	-122.6/-122.7	-
2.	KHF_2 / TBABF	-149.2/-148.7	-
3.	KF+KHF_2 *	-143.7	-
4.	TBAF + TBABF *	-140.8	-
5.	TBADT	-130.7 (9.17)	-156.2 (90.83)
6.	TBABF + TBADT *	-130.6 (11.17)	-153.5 (88.3)
7.	TBAF + TBADT*	-130.5 (8.56)	-149.1 (91.44)

* Equivolume solutions

The SiF_6^{2-} NMR peak is located at ~ -131 ppm as recorded in Table 7, in agreement with previous reports. [40] An increase in aqueous HF concentration causes peak position shifts to lower frequencies, i.e., upfield (higher ppm). The general trend of NMR peak shifts to higher ppm corresponds to higher ER, and is observed for all chemistries investigated.

Table 7 Peak positions for ^{19}F NMR (values in parentheses indicate area under the peak)

	Solution compositions	Peak 1 (ppm)	Peak 2 (ppm)
1.	H_2SiF_6	-130.9	-
2.	49% HF	-170.5	-
3.	0.9491 mol frac D_2O in THF, 0.0089 mol frac TBABF*	-148.7	-
4.	0.8115 mol frac D_2O in THF, 0.0089 mol frac TBABF*	-148.1	-
5.	0.9428 mol frac D_2O in DMSO, 0.0089 mol frac TBABF*	-148.4	-
6.	0.7889 mol frac D_2O in DMSO, 0.0089 mol frac TBABF*	-148.0	-
7.	0.9491mol frac D_2O in THF, mol frac TBADT*	-130.6 (8.86)	-156.4 (91.14)
8.	0.9505 mol frac D_2O in DMSO, mol frac TBADT*	-130.0 (6.63)	-156.2 (93.37)
9.	0.4345 mol frac D_2O in DMSO, mol frac TBADT*	-125.4 (28.72)	-156.3 (71.28)
10.	0.0089 mol frac $NaHF_2$ in D_2O	-132.5 (0.36)	-149.0 (99.64)**

*The mole fractions correspond to a rapid rise of etch rate as indicated in Figure 14, Figure 17 and Figure 18.

**broad peaks

THF and DMSO are weaker acids than is water, yielding lower ERs in aqueous/organic salt solutions since H^+ plays an important role in the etch mechanism [15]. For TBABF solutions in both THF and DMSO, an increase in water mole fraction shifts the NMR peak position to higher ppm, indicating an increased degree of solvation. Previous studies have reported both upfield and downfield shifts of ^{19}F peaks for HF_2^- with an increase in water concentration [56]; the upfield shifts were ascribed to hydrogen bonding. Also, the peaks for THF solutions are always upfield compared to DMSO indicating that there is an increased degree of solvation in THF solutions. As seen from Figure 17 and Figure 18, this increased solvation corresponds to an increase in ER.

The donor numbers of DMSO and THF are 29.8 and 20.0, respectively, while the acceptor numbers of DMSO and THF are 19.3 and 8.0 respectively; thus, as indicated previously [50], DMSO is a stronger electron pair donor than is THF. This property makes it more difficult for DMSO to solvate anions relative to THF. Such arguments should result in a greater SiO_2 ER in aqueous DMSO salt solutions than in THF salt solutions. This apparent discrepancy can be explained by the fact that DMSO can form hydrogen bonds with water above a DMSO mole fraction (X_{DMSO}) of 0.1 [57] which can account for the decrease in ER below this concentration. Because of differences in molecular structure, it is reasonable to assume that the extent of hydrogen bonding is lower in THF-water pairs than in DMSO-water pairs. Since hydrogen bonding inhibits the availability of water to take part in the reaction, ERs are higher for aqueous salt solutions in THF than in DMSO.

Below X_{DMSO} = 0.1, the fluoride anion is preferentially solvated by water [58]. A similar result should hold for HF_2^- in aqueous DMSO or THF mixtures which can explain the rapid rise in etch rate above X_{Water} = 0.9. Furthermore, Figure 17 and Figure 18 indicate that above X_{Water} = 0.9, the ER is nearly independent of the presence of organic solvent.

For TBADT solutions in both THF and DMSO, analogous trends to those of TBABF are observed. The etch product peak of SiF_6^{2-} also shifts to upfield positions with increasing D_2O mole fraction; in addition, the relative area under this peak decreases indicating an increased availability of the etchant $H_2F_3^-$ and hence an increase in ER.

NMR studies of aqueous HF solutions wherein the solution has reacted with SiO_2 to the extent that both the product and reactant species appear in NMR spectra have been performed (areas under the peaks are much larger than the detectability limit in these cases). As discussed in the section on initial characterization, aqueous HF solutions show a single NMR peak. The current study thus confirms the presence of reactant and product species. Table 8 shows NMR peak positions for a 1:350 HF:H_2O aqueous solution (ER of 3.8 nm/min initially) wherein the etchant has reacted with a BPSG film and has thus been depleted to the extent that the ER decreases to an ER of 2.5 nm/min or to an undetectable value (<1nm/min). The NMR spectra show three peaks; the peak at -130 ppm is due to SiF_6^{2-} (product), at -150 to HF_2^- reactant, and at -159 to $H_2F_3^-$ reactant. The areas under the peaks for both SiF_6^{2-} and $H_2F_3^-$ are consistent with an increase in product species and a decrease in reactant; however, the reason for an increase in HF_2^- peak area while

observing a decrease in ER is not apparent. Nevertheless, the relative change in peak area is small.

Table 8 ^{19}F NMR peak positions for depleted HF solutions (values in parentheses indicate area under the peak)

	Depleted HF	Peak 1 (ppm)	Peak 2 (ppm)	Peak 3 (ppm)
1.	"no" ER (<1nm/min)	-130.1 (81.78)	-150.6 (3.48)	-160.9 (14.74)
2.	2.5 nm/min	-130.1 (30.98)	-150.6 (2.63)	-159.5 (66.4)

3.6 Conclusions

Tetrabutylammonium-based salts have been used in an aqueous-organic solvent to vary ERs and hence selectivity of BPSG ER / Thermal oxide ER (TOX). Water concentration plays an important role in establishing the ER. THF and DMSO have been used as the organic solvents. Results have demonstrated that the solvent dielectric constant is not the only factor that establishes ER and that the differences in ER behavior of these two solvents can be explained in terms of relative basicity. NMR studies show that solvation of anions correlates with the observed ERs.

CHAPTER 4

DESIGN OF A LABORATORY SCALE REACTOR

The fact that surface cleaning, rinsing, residue removal, and conditioning sequences represent approximately 20% of the total number of processing steps used in the fabrication of state-of-the-art ICs [5] indicates that throughput can be increased by optimizing these processing steps and better integrating them into overall process sequences.

As film thicknesses and dimensions have decreased in succeeding device generations, HF solution formulations have become increasingly dilute (between 1:50 and 1:200, HF:water) in order to minimize or avoid unwanted attack or etching of films/structures during surface cleaning [17,59-61]. In addition, cleaning cycle times have been shortened to reduce chemical use and enhance wafer throughput [33,60]. Unfortunately, these trends have resulted in severe limitations that inhibit effective and efficient cleaning, and future device structures will clearly exacerbate these problems. First, although dilute HF solutions may minimize etch rates of films that are to be maintained on surfaces, they also reduce the etch rate of films that are to be removed; thus, longer exposure times are needed which obviates the primary advantage of dilute mixtures. Second, due to the equilibria between HF, F^-, H^+, HF_2^-, $(HF)_n$, and OH^- in aqueous solutions, the concentrations of chemically reactive species may be difficult to adjust so that removal rate and selectivities are optimized. In addition, such phenomena may also inhibit control of the kinetics of contaminant or film removal. If more concentrated HF solutions could

be used, shorter exposure times to existing/desired films will result, thereby enhancing throughput. In addition, these higher concentration solutions offer an additional approach to controlling the concentration of specific etchant species present in the solution due to the HF solution chemistry and equilibria.[3]

The use of a selected chemistry that depends upon the composition of the films, impurities, residues, and the chemical nature of the surfaces present in a manufacturing process requires careful study of interactions between the chemistry and process parameters invoked in the operation. Specifically, the etch rate (and hence selectivity) may vary across the wafer because of inherent reaction rates as well as due to interaction with process parameters such as flow rate, concentration, and temperature. In such situations, studies that account for these effects simultaneously are required in order to better understand and control the process. Computational Fluid Dynamics (CFD) has served as a design tool to allow improved control of wet cleaning processes in the semiconductor industry [62]. In addition, the use of thin (<20 nm) films, closely-spaced features, and ultra-shallow (<50 nm) junctions exacerbates the control necessary for efficient and effective liquid cleaning. For on-line process control, particularly for Model Predictive Control (MPC) implementation, a predictive model for the process is essential. While CFD has excellent predictive capabilities, it cannot be directly implemented in

---

[3] Part of this chapter has been submitted for publication in IEEE Trans. Semicond. Manufac., 2010

process control strategies because of the computational time; however, model reduction strategies can assist in model simplification [63].

Recently, Lam Research Corporation designed and built a single wafer short contact time reactor for substrate cleaning/etching [39,64-66]; a schematic is shown inFigure 22. Contact time is defined as the length of time a single point on the wafer is in contact with the liquid (wet) chemistry. In this system the contact time is on the order of one second with controllability down to a fraction of a second (~0.3 or less). One immediate benefit of the short contact time concept is improvement of overall system throughput. In addition, this approach also allows the use of more concentrated chemistries that are not otherwise possible due to the constraint in film loss. Preliminary results from this reactor configuration indicated that investigations into the chemistry flow rates, contact times and etchant compositions are critical to establish the proper process condition for the most effective etching, cleaning and throughput. We have used CFD to design a miniaturized and simplified version of this reactor capable of processing 2 cm x 2 cm substrates. In this laboratory reactor the substrates are stationary and positioned immediately beneath the inlet holes. Although the drying process has been modeled and described in detail in the literature, see for example refs [66-70], a drying model has not been incorporated into the current CFD simulations.

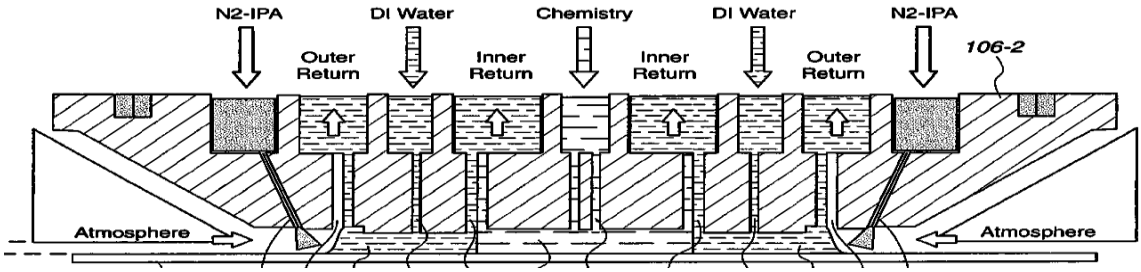

Figure 22 schematic of LAM reactor

In an integrated clean process, cleaning of wafer surfaces can be performed using convective fluid transport. Also, wafer rinsing must be carried out as quickly as possible to minimize the time during which films or substrates can continue to etch. Hence, we have designed our reactor using CFD simulations (but no reaction kinetics) based solely on velocity fields with a target value of tangential velocities at a distance of 0.05 mm or less from the wall to be >1 mm/sec for a constant flow rate of 100 ml/min. This criterion was used as a semi-quanitative way of quickly arriving at the final reactor design by comparison of velocity fields under various scenarios. This ensures that the contact time remained low (<1 sec) as we have verified from a set of residence time distribution studies (described later in the chapter). This approach also helps to minimize the number of iterations needed for reactor design. As described below, based on the insight gained using these simulations, we have subsequently incorporated reaction kinetics into the simulations using a simplified geometry to allow prediction of the (observed) etch rate profiles of films within experimental error. The final design was based on CFD simulations that used a commercial software package (FLUENT®).

It should be noted that we have used etching of SiO_2 films in aqueous HF solutions as a model system to validate our simulations, to design the experiments and to test the operation of the integrated process. This reactor configuration is versatile in that it can be used to wet etch/clean/dry other films under widely different process conditions. Since fluid velocities decay with distance from the inlet in this radial flow reactor (i.e., the flow distribution is well defined), the specific chemical characteristics of a particular film and the process conditions used cause the concentration of reactants (and correspondingly the etch rate) to vary as a function of position in the reactor. Experimental investigation and simulation of the various process variables can provide insight into the etching mechanism.

This chapter is organized in the following way. The approach to reactor design using CFD simulations is described and the manner by which reaction kinetics for SiO_2 etching is incorporated into these simulations is discussed. The details of the etch reactor system are then outlined, experimental results presented and opportunities for improvement in this reactor design identified.

4.1 Laboratory-Scale Reactor Design Using Velocity Simulations

Specific geometries were created in GAMBIT® and a structured mesh generated for most of the regions within these geometries for reduction of computational time. The worst element had an equisize skew quality value of 0.34 or better. After confirming the geometric symmetry for the velocity distribution (or the reaction contours as described below), only one-half or one-quarter of the geometry, depending on the specific situation

studied, was generated to reduce the computational time. The geometry was imported into Fluent 3ddp solver and the continuity and momentum balance equations solved for each of the geometries using FLUENT®. Laminar flow was assumed and the 3D, single phase, single species equations were solved using a sequential, implicit, steady state solver in the absolute velocity configuration and a cell-based gradient option. No energy equations were used and only system hydrodynamics were studied without employing reaction kinetics. Since the equations for these situations are well documented, they are not repeated here [71].

Dependence on grid selection was determined by using boundary adaptation, gradient adaptation, isovalue adaptation and also by manually re-meshing the geometry. Each of these simulations was then compared with the starting base case and if the velocity profile vectors were different for the different meshes, the smaller grid was chosen. The procedure was repeated until no difference between successive simulations was observed. Under-relaxation parameters for continuity and momentum were 0.3 and 0.7 respectively. Where appropriate, under-relaxation parameters for species and energy were initially set to the default value of 1. Depending on the solution convergence, any/all of these relaxation parameters were lowered by trial and error. The default discretization schemes of first order upwind scheme was used for species, energy and momentum. For pressure, the default discretization standard is used. The pressure velocity coupling method was SIMPLE. The H/D ratio is used to characterize the reactor geometry, where H is the distance between the top head and the wafer surface (see Fig. 4 below for detail) and D is the diameter of the inlet hole. Unless otherwise indicated a default value of 0.5 for this

ratio is used in this thesis. The species inlet mass fraction (where appropriate) was specified to be the equilibrium mass fraction computed using MATLAB® (see the following section on "kinetic simulations"). A no slip boundary condition was used at the reactor walls and wafer surface. All solid surfaces were assumed to be stationary unless otherwise noted for a specific case. No reaction was specified at non-reactive surfaces. The species zero diffusive flux was invoked for cases involving multiple species. These conditions remained the same for reactive surfaces with the only difference that reaction was specified to occur. For the outlet, an "outflow" boundary condition was specified instead of pressure outlet.

Table 9 shows the design parameters, their final selection/range of values over which simulations were investigated and whether or not that parameter was predicted to be important.

Table 9 Influence of process parameters based on velocity simulations

Parameter	Important?	Comment
Inlet hole diameter	Yes	Between 0.5 and 2 mm
Spacing between top reactor 'head' and wafer surface	Yes	Variable gap adjustment system has been implemented (between 0.1 mm – 5mm)
Geometry of wafer	No	Simulated for square and

		circular wafers
Configuration of inlet flow (perpendicular vs. parallel to wafer)	Yes	Perpendicular
Configuration (concentric vs. single holes for de-ionized water (DI) and HF-based solutions)	No	Single holes
Size of wafer	No	Simulated for 1 inch and 2 inch wafers
Number of inlets	Yes	4
Spacing between inlet holes	Yes	>0.5 mm
Number and location of exhausts (outlets)	Yes	Safety concerns dictated a small reservoir for collection of product fluid and hence the exhaust was from this reservoir
Staggered vs. normal arrangement of water and HF-based chemistry inlet	No	Non-staggered
Reactor size	No	varied from a reactor of 90 mm X 100 mm to a reactor of 32.6 mm X 29.8 mm

Figure 23 shows the cross-sectional schematic of a reactor configuration in which some of the terms used in Table 9 are explained.

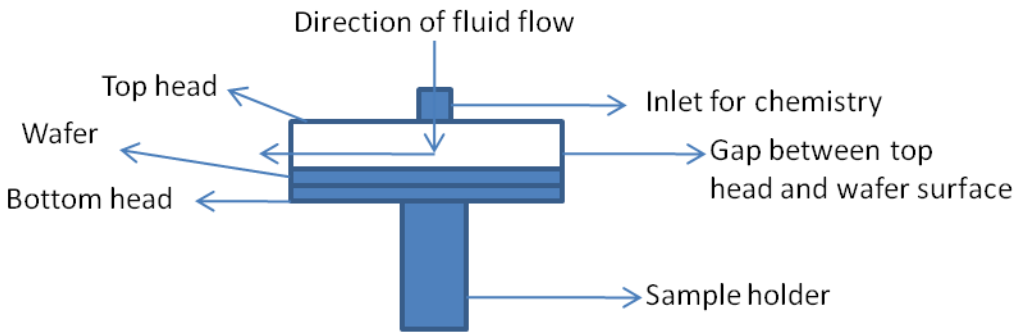

Figure 23 Reactor cross-sectional schematic for explanation of some terms used in Table 9

As an example of the results of the simulation studies, Figures. 5 and 6 compare the velocity profiles (in m/sec) obtained for variation in H/D of 0.19 to 0.5 at a constant gap between the reactor top head and the wafer surface. These figures show a magnified view of the inlet region (between the inlet and the wafer surface) with only a quarter of the wafer shown. There is a very low velocity region close to the center of inlet near the wafer surface around which the velocity profiles appear to develop. The blue colored region at the top of the profiles in Figure 24 and Figure 25 indicates the top reactor head around the inlet hole. Clearly, a smaller inlet hole diameter corresponds to a higher velocity at radial positions away from the inlet.

Figures 7 and 8 compare the flow velocities (in m/sec) for variation in head gap at a constant value of inlet hole diameter. The head gap dictates the volume available for liquid to flow through the reactor which in turn will establish the flow velocity. These

figures show a magnified view of the region near the inlets where the simulation has been performed for a staggered arrangement of inlets. Only half of the cylindrical portion around each inlet is shown. Out of the eight inlets, only four inlets are used for fluid entry (as indicated by higher velocity region around those inlets). As the head gap decreases, the flow velocity increases for all parts of the wafer except near the inlet regions.

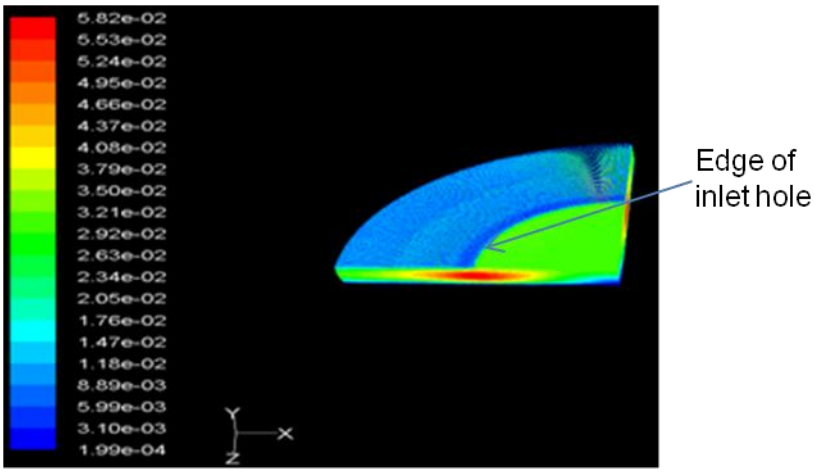

Figure 24 Velocity profiles in the inlet region, in m/sec, (H/D = 0.19)

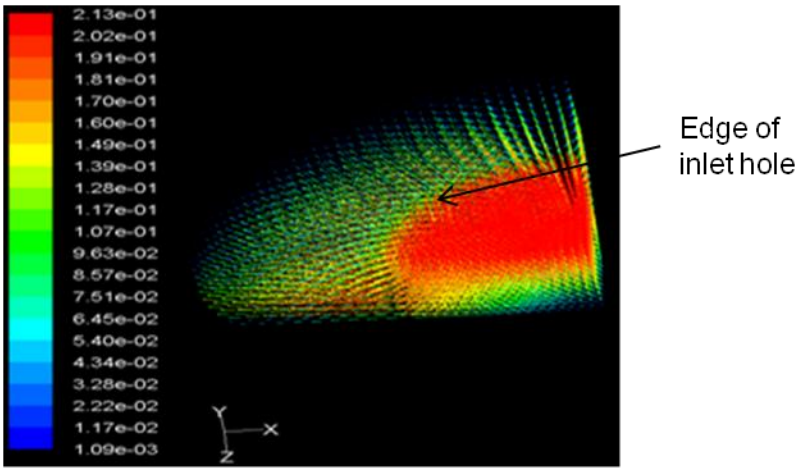

Figure 25 Velocity profiles in the inlet region, in m/sec (H/D = 0.5)

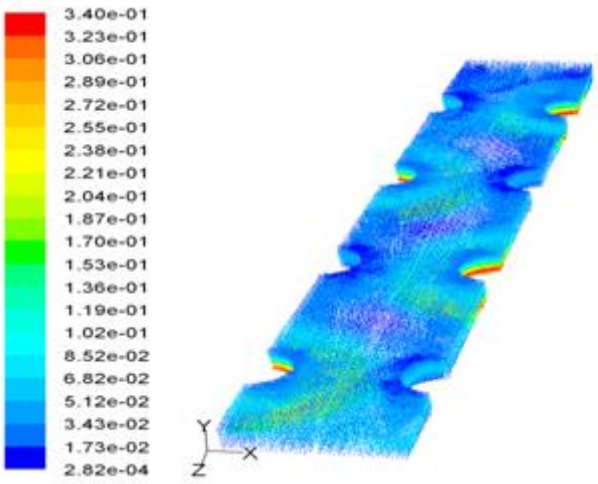

Figure 26 Velocity profiles near the inlet region, in m/sec, (H/D =0.5)

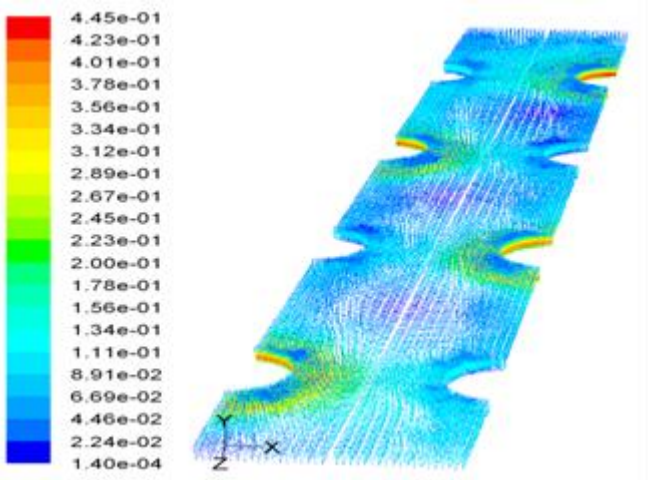

Figure 27 Velocity profiles near the inlet region, in m/sec, (H/D =0.25

Since we want to consider contact times as low as 0.1 sec, a dynamic simulation for the determination of residence time was also performed for the geometry shown in Figure 28; results of the simulation are shown in Figure 29. In Figure 29, the legends E1L etc. refer

to the outlets (Exits) number (labeled from 1 to 4 in Figure 28). The ‘L/R’ denotes the left or right exit. The inlets that are shaded are the ones that provide fluid into the reactor i.e. non-shaded inlets are blocked for fluid entry. The tracer is fed into inlet #1 (shaded). Only a half-geometry of the reactor is simulated to reduce the computational time since the geometry is symmetric. The two concentric circles (of radii differing by 0.2 mm) indicate the wafer (inner circle) and the tolerance provided by the sample holder (the sample holder is assumed to be a trench cut out in a suitable material in these simulations). The tracer is a pulse input and the details for carrying out this calculation are given in [72]. The mass flow rate is negative due to the convention that outgoing flow is negative. The small spike in mass flow rate profile at ~ 0.38 sec is due to the increase in time step at the cost of decreased accuracy to decrease the computational time. However, this alteration does not substantially change the results. The flow distribution obtained is consistent with an intuitive understanding of the process in that the peak corresponding to the ‘E1L’ should come earlier in time than the peak labeled ‘E1R’ as shown in Figure 29.

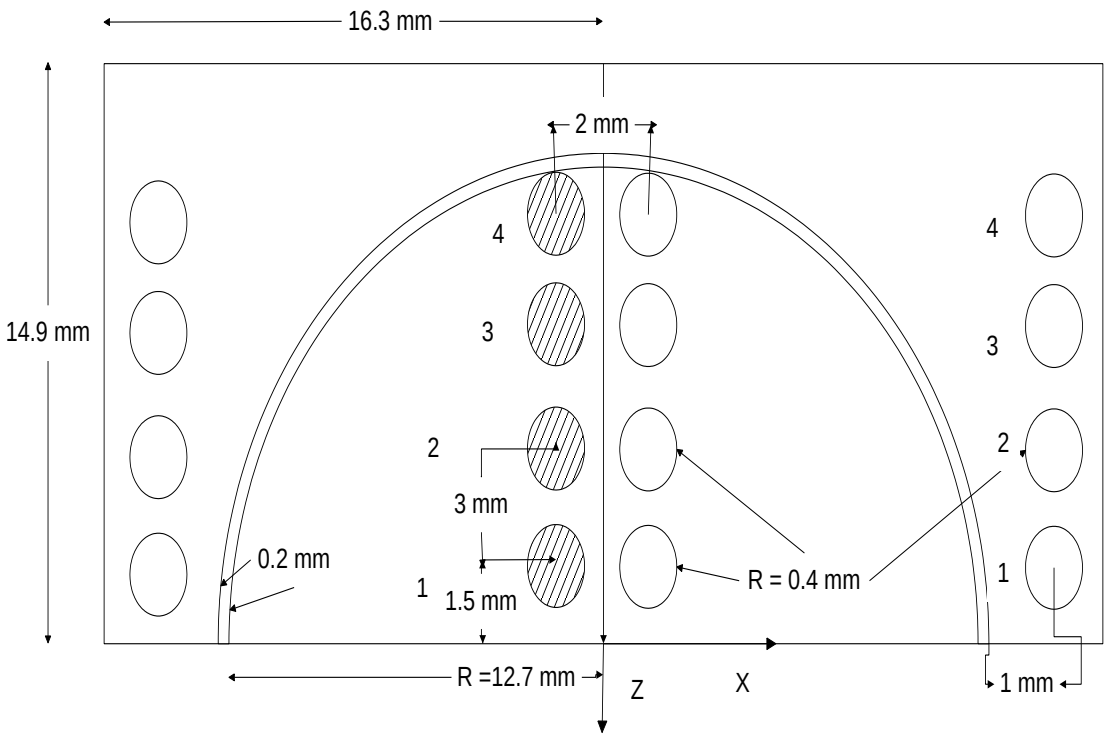

Figure 28 Reactor schematics simulated for residence time determination, shaded inlets only are used to provide fluid into the reactor

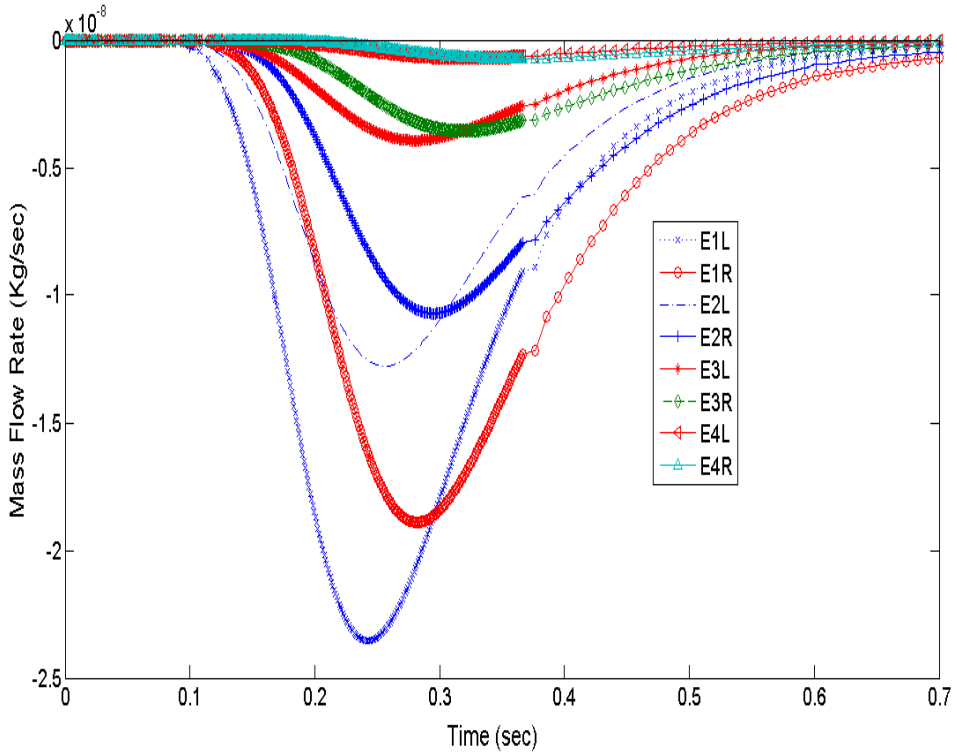

Figure 29 The residence time (sec) for the geometry of Figure 28, 'E' refers to exits, numbers 1-4 to the inlets in Figure 28 and 'L/R' refers to Left or Right

4.2 Conclusion

This study shows that diameter of the inlet is the most important parameter that controls ER variation from the center to the edge of the wafer followed by spacing between the reactor top head and the wafer surface. In order to reduce the number of iterations in the design process, single-inlet-hole simulations are carried out to study the influence of process parameters such as concentration and flow rate by incorporating kinetics as detailed in the next chapter.

CHAPTER 5

CFD – INCLUDING KINETIC SIMULATIONS

[4]Since even the overall etch reaction for SiO_2 in fluoride-containing solutions (no mechanism assumed) is not well-established [10], some investigators have suggested that it is easier mathematically to express the etch rate only as a function of HF, which then removes the dependence on the specific etching species and surface complexes [7,8]. Etch rates can then be written in various forms, including power law kinetics or Freundlich or Langmuir Hinshelwood kinetic expressions. Since the exact mechanism and kinetic expressions are complicated/unclear, the current CFD simulations described in detail in this thesis invoked first order kinetics for the surface reaction of aqueous HF with SiO_2. However, we should note that various kinetic expressions from more advanced experimental data can be incorporated into the simulations if desired.

Based on velocity simulations, kinetic simulations were performed by invoking various kinetic expressions reported previously as well as the ones obtained in our laboratory. Although more complicated forms for reaction kinetics have been reported [25,54], we invoked first order kinetics for HF solutions, i. e,

$$r_{SiO_2}(kgmol/(m^2.\text{sec})) = kC_{HF} \qquad C_{HF} \text{in kgmol/m}^3 \tag{10}$$

where k is the reaction rate constant and C_{HF} is the concentration of HF.

---

[4] Part of this chapter has been submitted for publication in IEEE Trans. Semicond. Manufac., 2010

This choice was based on our preliminary results and on the simplicity of these kinetic expressions; indeed, this assumption led to a reasonable (within 10%) agreement with experimental etch rate results.

In FLUENT®, a reaction mixture is defined to be composed of species that are involved in the reaction(s) under consideration. For purposes of the current analysis, the (liquid state) species in addition to water are identified as H_2SiF_6, HF, F^-, HF_2^-, $H_2F_3^-$, and H^+, while the solid state species is silicon dioxide. Continuity, momentum balance and species balance equations are solved without consideration of the energy balance. The specific heat capacity and density values of HF are defined at 49% of the pure liquid values due to the non-linear dependence of these properties on concentration. For all fluoride species, all properties except molecular weight are considered to be the same values as those of molecular HF. Pure substance properties for HF are from [73], H_2SiF_6 from [74] and SiO_2 from [75]. Mass diffusivity of all species is taken to be that of various conc. of HF = $5*10^{-5}$ – $5*10^{-6}$ cm^2/sec [76]. The standard state enthalpy and standard state entropy of all components except water are set to zero. A reference temperature of 298.15 K is used for all of the components. The density of the mixture is calculated by a volume weighted mixing law, while the specific heat capacity, thermal conductivity and viscosity by mass weighted mixing laws. In the species transport model, inlet diffusion and diffusion energy source are used. The mass deposition source of the wall surface reactions is invoked to take into account the effect of surface mass transfer in the continuity equation. The etch rate in nm/min is changed to the units of $kg/(m^2.sec)$ by multiplying the etch rate in nm/min by the density of SiO_2 (assumed to be 2200 kg/m^3). A

plot of ER of SiO_2 in kg-mol/(m^2.sec) vs. concentration of HF in kg-mol/m^3 gives the rate constant (slope) in units of kg-mol SiO_2.m/(kg-mol HF.sec) as shown in Figure 30 (the error bars on this plot are smaller than the symbol size). This value is then used in the simulations for various cases as shown in Table 10.

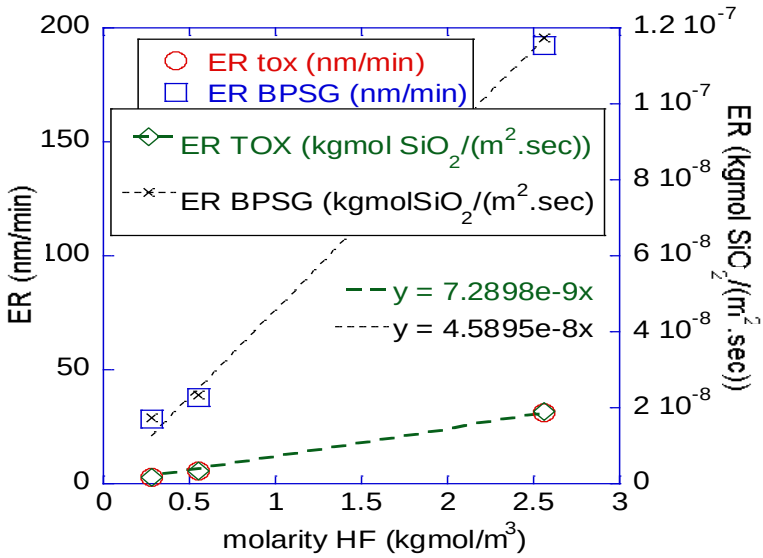

Figure 30 SiO_2 etch rate in nm/min and kgmol/(m^2.sec) vs. HF concentration, the pre-exponent values were obtained by curve fitting

As noted above, the geometry simulated is one-quarter of a one inch diameter wafer. The configuration has one inlet at the top, which is perpendicular to the wafer and at the wafer center. The 'default' values are those determined from velocity simulations (previous section).

In order to simulate the equilibrium reaction, the inlet (bulk) concentration of species taking part in the equilibrium process must be the equilibrium concentration. If this is not

true, the system will try to attain equilibrium based on its specified forward and backward reaction rate constants [77]. In this case, it would not be possible to differentiate between the species mass fraction changes due to surface reaction from the ones due to 'approach towards equilibrium'. That is, at locations away from the inlet, if the species concentration changes, it will not be possible to determine if this change is due to surface reaction or if it is due to incorrect specification of equilibrium. This concentration for each species is calculated from the equilibrium relationships, fluoride balance and charge neutrality as described by Equations [10] – [15]. Calculations are performed in MATLAB® and are compared with results for the same set of calculations reported in [32]. Figure 32 shows the calculation results for the case of 0.1 – 6 mol/kg HF only. The same calculation has been carried out when strong electrolytes such as F^- and HF_2^-, are present.

$$HF \leftrightarrow H^+ + F^- \qquad K_a = 6.85 \cdot 10^{-4} \quad mol/kg \tag{11}$$

$$HF + F^- \leftrightarrow HF_2^- \qquad K_1 = 5.0 \quad kg/mol \tag{12}$$

$$HF + HF_2^- \leftrightarrow H_2F_3^- \quad K_2 = 0.58 \quad kg/mol \tag{13}$$

$$K_w = C_{H^+} C_{OH^-} \tag{14}$$

$$a_0 + c_0 + 2d_0 = C_{HF} + C_{F^-} + 2C_{HF_2^-} + 3C_{H_2F_3^-} \tag{15}$$

$$C_{H^+} + c_0 + d_0 = C_{OH^-} + C_{F^-} + C_{HF_2^-} + C_{H_2F_3^-} + b_0 \tag{16}$$

where $a_0 = C_{HF,initial}$, $b_0 = C_{H^+,initial}, c_0 = C_{F^-,initial}, d_0 = C_{HF_2^-,initial}$

Comparison of Figure 31 [32] with Figure 32 indicates that at higher HF concentration ranges, the equilibrium constant relationship is not satisfied in this simulation. To get a

better estimate of species concentration profiles, the equilibrium relationship is recalculated for all the cases reported in [32]. These values are used as a starting point in FLUENT®. Also, species concentration values calculated by our MATLAB® code agree with previously reported values for species concentrations calculated by taking into account only HF dissociation and bifluoride formation [54]. A concentration of HF:H_2O = 1:100 was used in all simulations reported here unless otherwise indicated.

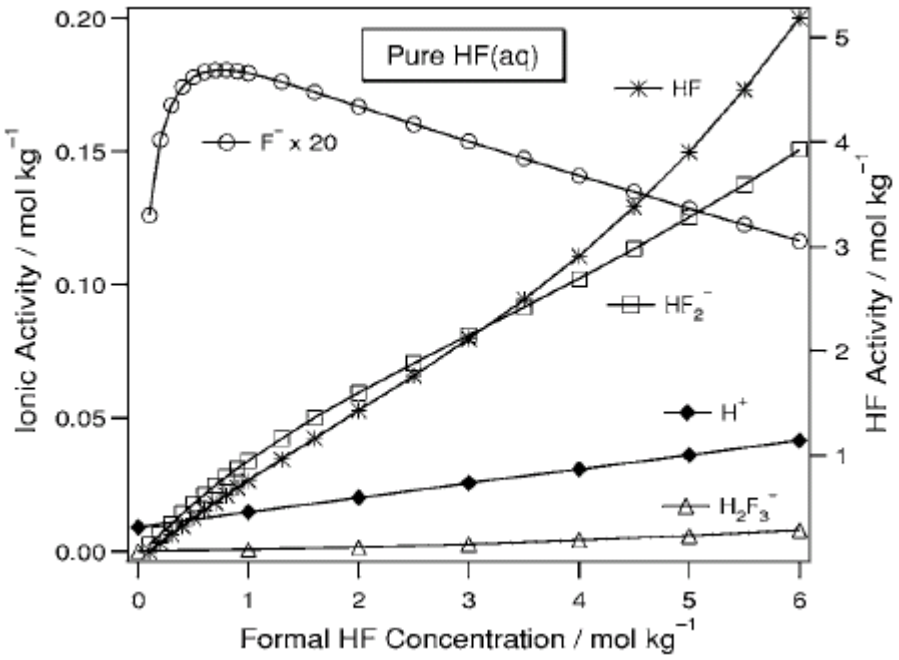

Figure 31 0.1-6 mol/kg HF (aq) – predicted values as per ref. [32]

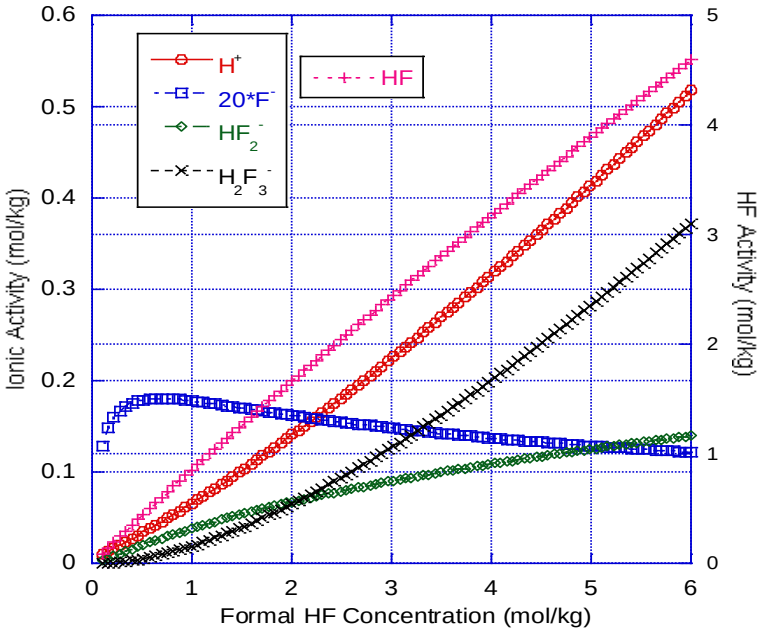

Figure 32 0.1-6 mol/kg HF (aq) – calculations from this work,

Simulations have been used to study Thermally-grown silicon OXide (TOX) and Boron and Phosphorus doped SiO_2 (BPSG) films, since we observe one order of magnitude difference in the ER between them. The effect of grid size was investigated both by changing the grid directly and by using grid adaptation in FLUENT®. Boundary adaptation, gradient adaptation and isovalue adaptation were used for this purpose. When the simulations no longer displayed a grid size dependence, the meshing was accepted as appropriate. Due to the finite grid size, there will always be some error for the calculation of ER at the wall; however, the profiles followed the ER trends observed in our laboratory experiments as described in detail below. The base (comparison) case simulation corresponds to the values given in Table 10.

Table **11** gives a summary of the simulation results for BPSG and TOX.

Table 10 Parameter values for the base case

	Parameter	Value
1.	TOX pre-exponent	$7.3*10^{-9}$ kgSiO2.m/(kg-mol HF.sec)
2.	BPSG pre-exponent	$4.6*10^{-8}$ kgSiO2.m/(kg-mol HF.sec)
3.	Head gap/diameter of inlet (H/D)	0.5
4.	Reynolds number (based on inlet diameter and the average flow velocity in the inlet)	212.63
5.	Concentration of HF:H_2O	1:100

Table 11 Summary of the simulation results for ER in nm/min

Case	Wafer	ER at center of wafer (nm/min)	ER at edge of wafer (nm/min)	Difference in ER: center ER – edge ER (nm/min)
Base case	TOX	3.18	3.18	0
	BPSG	22.71	22.55	0.16
High concentration (1:10)	TOX	29.1	29.1	0
	BPSG	206.99	205.63	1.36
Higher flow rate (Re = 2126.3)	TOX	3.18	3.18	0
	BPSG	22.68	22.66	0.03
Lower flow rate (Re = 21.263)	TOX	3.18	3.18	0
	BPSG	22.68	22.28	0.41
Lower gap H/D = 0.25	TOX	3.18	3.18	0
	BPSG	22.71	22.6	0.11
HF dissociation with surface reaction	TOX	3.02	3.02	0
	BPSG	21.6	21.3	0.3
HF dissociation +bifluoride formation	TOX	2.83	2.83	0
	BPSG	20.21	20.07	0.14
HF dissociation +bifluoride formation +trifluoride formation	TOX	2.8	2.8	0
	BPSG	19.96	19.83	0.14
Activity Coefficients	TOX	2.8	2.77	0.03

	BPSG	19.94	19.72	0.22

For the simulation of reaction kinetics, velocity profiles are not compared; rather, mass fraction profiles are used as indicative of chemical species/surface reaction profiles. For brevity, these profiles are not reported here for every simulation; instead, three representative conditions for the contours of surface etching of BPSG are shown in Figure 33, Figure 34 and Figure 35; the parameter values used for the simulations performed are shown in Table 10. The contours of surface reaction rate are negative because of the convention in FLUENT® that deposition profiles are positive and etch profiles are negative.

We include here a brief description of the simulation results for the cases shown in Table 11.

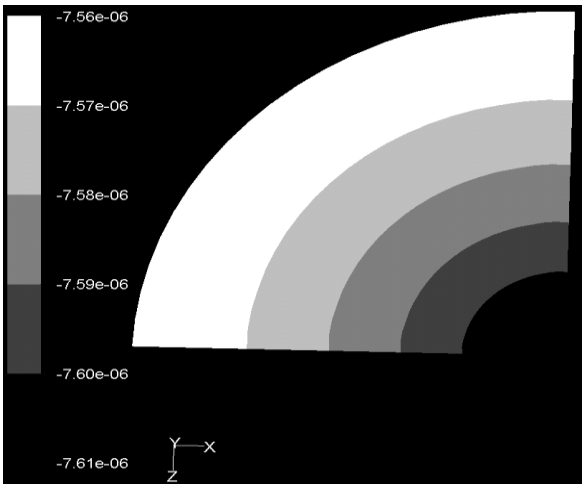

Figure 33 Contours for surface etching of BPSG in kg/(m^2.sec) for 1:10 HF:H_2O

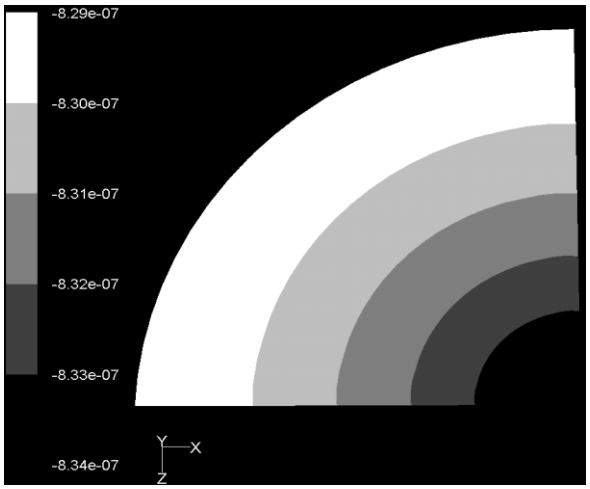

Figure 34 Contours for surface etching of BPSG in kg/(m^2.sec) for the Base Case

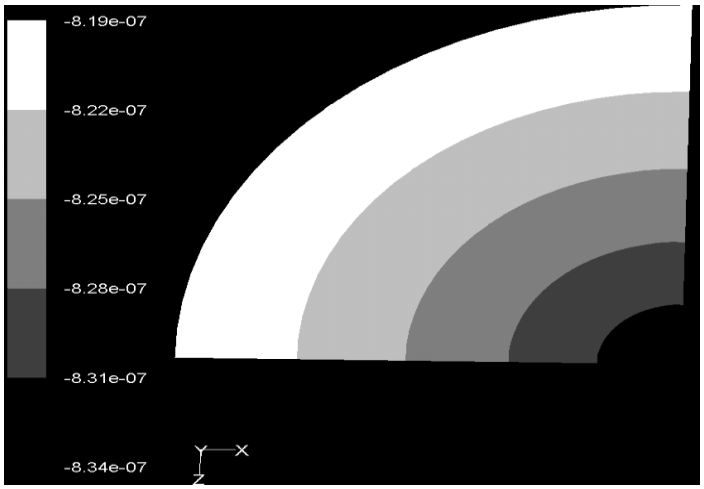

Figure 35 Contours for surface etching of BPSG in

kg/(m^2.sec) for Re = 21.263

5.1 Effect of higher concentration

As expected intuitively, H_2SiF_6 mass fraction contours for 1:100 HF:H_2O vs. 1:10 HF:H_2O concentration indicate that the amount of H_2SiF_6 generated is greater for the

1:10 solution than for 1:100 solution. Since the etch rate is driven by mass fractions near the surface, the bulk HF mass fraction contours are essentially uniform over the entire wafer indicating that no significant HF depletion occurs in the bulk solution during etching of either BPSG or TOX. The etch rate for BPSG is close to an order of magnitude greater than that for TOX. However, the etch rate variation across the wafer for BPSG in 1:10 HF is approximately 1.4 nm/min which is one order of magnitude higher than that in the 1:100 solution as shown in Table 11. It should be noted that BPSG in 1:100 solution shows a center-to-edge ER difference while TOX in 1:10 HF does not show this difference. Apart from the numerical inaccuracies in the simulation and inherent difference in ER of TOX vs. BPSG (as seen from Figure 30), this center-to-edge effect is due to the combination of a high ER film (BPSG) in a dilute (1:100) solution, thereby enhancing the reactant depletion. This effect is in contrast to that of a low ER film (TOX) in a concentrated solution (1:10).

5.2 Effect of flow rate

The nominal operating mass flow rate was increased/decreased by one order of magnitude. The effect of these flow rate changes on ER variation is described below.

5.2.1 Increasing flow rate

An increase in flow rate has no effect on the mass fraction profiles of chemical species/surface reaction rate for TOX. As a result, the center-to-edge ER variation remains insignificant. For BPSG, higher flow rates decrease the ER variation across the wafer from 0.16 nm/min in the base case to 0.03 nm/min. It should be noted that the Reynolds number in this high flow case is in the transition regime between laminar and turbulent flow. As a result, inclusion of the effects of turbulent kinetic energy (k) and

turbulent kinetic energy dissipation rate (ε) in the simulation may become important in this flow condition.

5.2.2 Decreasing flow rate

A decrease in flow rate from the base case has no effect on the profiles for TOX. For BPSG, the ER variation across the wafer increases to 0.4 nm/min. This change resulted in the variation of HF mass fraction profiles (from 0.00556 to 0.00546) across the wafer and corresponding changes in H_2SiF_6 profiles.

5.3 Effect of gap between reactor top head and wafer surface

A decrease in gap height to half of the nominal value has no significant effect on either the etch rate or the etch rate profiles for TOX. The change in profiles for BPSG ER is also marginal (0.11 nm/min).

5.4 Incorporation of various equilibria

In order to include the effect of various equilibrium reactions in FLUENT®, several strategies were employed.

1) With no surface reaction included, the contours of any chemical species should be independent of the position in the reactor and should be the same as that of the inlet concentration. Since each of the equilibrium reactions is modeled by a forward and backward reaction, these contours should be independent of changes in the forward and backward reaction rate constant. This assumption was verified by changing both reaction rate constants over the range of $1*10^{-9}$ to $1*10^{9}$, while keeping the required equilibrium constant at a fixed value.

2) With no surface reaction included, if the inlet concentration is not the equilibrium concentration for a specific set of reactions, the contours of species mass fraction should

change with position in the reactor. Also, this change will be dependent on the value of rate constant specified. Indeed, this dependence was observed in all simulated cases that included equilibrium reactions.

3) With surface reaction included, the species mass fraction contours may change with position in the reactor, depending upon the process conditions. However, these mass fractions should be independent of the values of forward and backward rate constants. This assumption was verified by changing the rate constants over the range $1*10^{-9}$ to $1*10^{4}$. With an increase in the forward rate constant > $1*10^{4}$, increasing difficulties were encountered with convergence of the solution to the set of equations.

Results of this investigation of the influence of forward and backward reaction rate constants on the simulation of equilibria, led to the selection of a forward rate constant of 1, with the backward rate constant calculated from the corresponding equilibrium constant. Both the default specification in FLUENT® and a User Defined Function (UDF) were used in order to specify these values. Simulation results from these two approaches are virtually identical since the difference between the mass fraction profiles for species calculated by these two approaches is $<1*10^{-6}$.

5.4.1 Inclusion of HF dissociation

The variation in ER across the wafer is unchanged from that of the base case for TOX. The absolute ER is lower than that of the base case since the mass fraction of HF (whose contours are again unchanged across the wafer) is reduced due to dissociation, for the same initial concentration of HF. The mass fraction contours of F^- and H^+ are essentially

constant at a value of $2.56*10^{-4}$ and $1.35*10^{-5}$ throughout the reactor due to negligible HF depletion. The variation in ER for BPSG increased from 0.16 nm/min to 0.3 nm/min.

5.4.2 Inclusion of HF dissociation and bifluoride formation

The absolute ER is lower than that of both the base case and the case in which HF dissociation is included. Mass fraction contours and ER variation follow the same trends as those for inclusion of HF dissociation (5.4.1).

5.4.3 Inclusion of HF dissociation, bifluoride formation and dihydrogen trifluoride formation

The absolute ER is marginally lower (variation occurs in the third decimal place, and so does not appear in Table 11) than that of the case in which bifluoride formation is included. Other trends are identical to the case of bifluoride formation (5.4.2).

5.4.4 Effect of activity coefficients

The activity coefficient variation has been calculated in ref [32]. This variation has been curve-fitted and the expression as a function of HF concentration (valid up to 2mol/kg of HF concentration) was used in FLUENT® in the form of a User Defined Function (UDF). The expression for HF activity coefficient is (with [HF] in mol/kg)

$$0.0202 \cdot HF^{2} - 0.0962 \cdot HF + 0.9807 \quad (17)$$

And the expression for ionic activity concentration is

$$0.0458 \cdot HF^{2} - 0.146 \cdot HF + 0.901 \quad (18)$$

Inclusion of activity coefficients for HF, H^{+} and fluoride species shows a marginal effect ($<1*10^{(-3)}$ relative difference) on the contours of all chemical species. The ER variation across the wafer is 0.03 nm/min for TOX and 0.22 nm/min for BPSG.

5.5 Conclusions

HF concentration was the most influential parameter on the variation of ER across wafers followed by the HF flow rate. However, since the reaction rate is assumed to be dependent only on the equilibrium concentration of HF, and because the equilibrium HF concentration decreases with the incorporation of various equilibria, the ER decreases. In addition to experimental and numerical errors, the difference between simulated and experimental etch rates may also be due to the specific density of SiO_2 assumed and the fact that the reaction rate pre-exponent has been obtained from curve fitting to the data collected. The base case ER obtained from the curve-fit expression for BPSG is 21 nm/min; this value shows better agreement with the simulation value in terms of center to edge ER variation as indicated in Table 11, than does the situation where activity coefficients were incorporated for the corresponding equilibria.

CHAPTER 6

REACTOR FABRICATION AND EXPERIMENTAL VERIFICATION OF SIMULATION RESULTS

[5]The simulation results described above led to the reactor design shown in Figure 36. In these different reactor views, the inlets for DI rinse, HF solution and dry N_2 along with two outlets for reactor effluent are labeled. In the drying operation, the same tubes used for DI water rinsing and HF flow are used to dry with N_2. A movable sample holder inserted into the bottom reactor head is held in place by viton o-rings. The top reactor head is detachable to allow sample introduction into the reactor. Vacuum is applied through the sample holder so that the wafer is immobilized. Two identical reactors have been fabricated, one in (transparent) polycarbonate to observe the fluid flow (shown in Figure 36) and the other in a chemically resistant polymer for compatibility with HF. A micrometer system for controlling and measuring the gap height between heads has also been implemented as shown in Figure 37.

---

[5] Part of this chapter has been submitted for publication in IEEE Trans. Semicond. Manufac., 2010

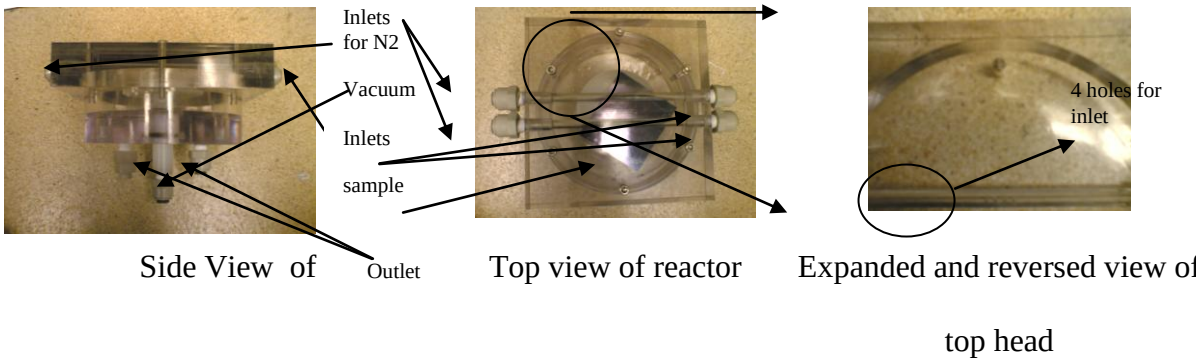

Figure 36 Laboratory reactor constructed from polycarbonate

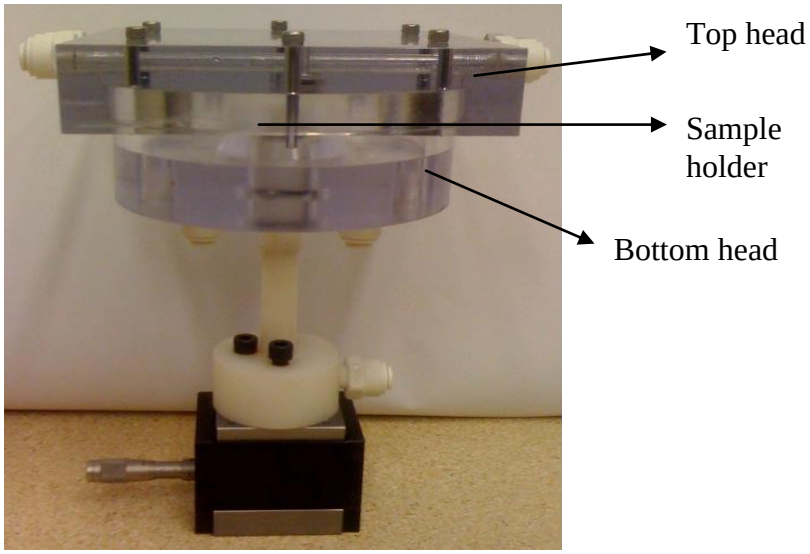

Figure 37 System for measurement of gap height, where the gap is the distance between the top head and the sample holder

6.1 Reactor system

The reactor system schematic is shown in Figure 38 and Figure 39; the entire unit was assembled inside a walk-in fume hood. All tubing that contacts HF is polypropylene. The DI flow rate is gravity driven whereas HF is pumped using a Cole-Parmer Masterflex L/S

peristaltic pump. The height and diameter of the tank required to give a reasonably constant flow rate (1.25 ml/sec – 1.20 ml/sec) for DI water over the rinsing times used (1min-3 min) gives rise to a Differential Algebraic Equation (DAE) system whose index can be greater than one depending upon the degrees of freedom specified. The details of this problem can be found on page 106-108 in Ref [63]. This system was simulated using gPROMS® for the final design. Valves V-DIW-1, V-HF-3 and V-HF-4 are needle valves. These valves are needed to establish resistance in the liquid flow path to achieve the appropriate pressure in the line. All other valves are two way valves. The valves in the DI water line are stainless steel while the valves in the HF line are PFA. F1 is a rotameter (Omega 10-100 CCM). V-N2-1 and V-N2-2 are stainless steel valves in the N_2 line that is used for drying. Vacuum is established with an Alcatel pascal 2005 SD pump.

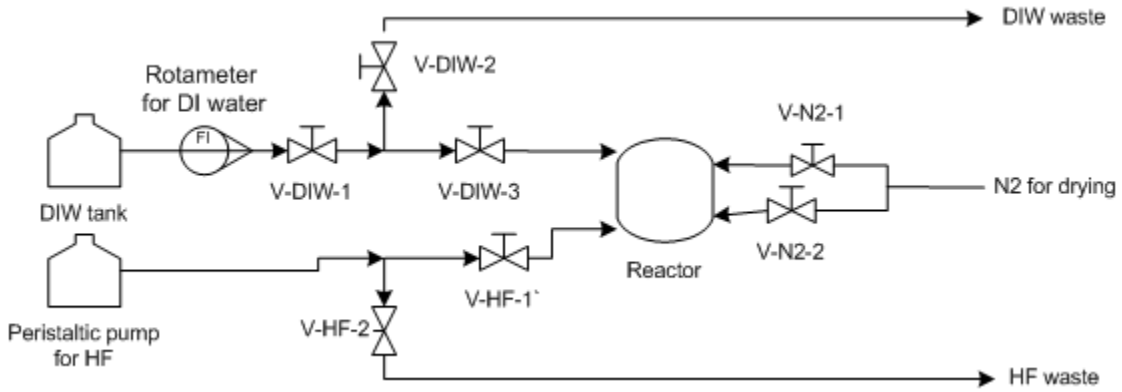

Figure 38 Reactor system top view (showing inlets for HF, DI water and nitrogen)

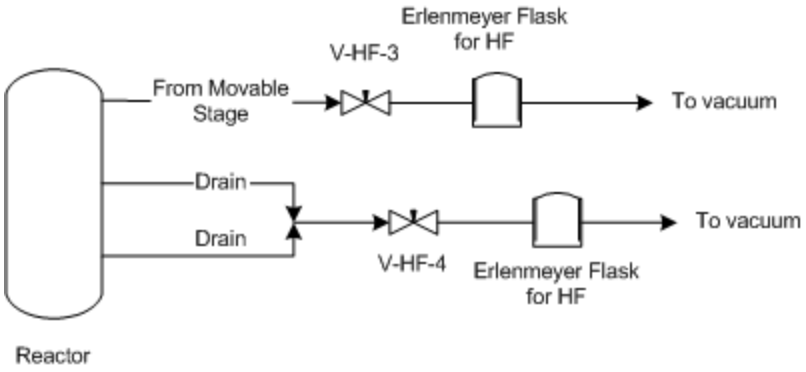

Figure 39 Reactor system side view (showing drain and vacuum)

Figure 40 Partial view of the reactor system configuration – 1

Figure 41 Partial view of the reactor system configuration - 2

Figure 42 Partial view of the reactor system configuration – 3

6.2 Experimental results

The ER of TOX films was studied for a 1:100 concentration of HF in the HF resistant reactor, where the solution flow rate was fixed at 100 ml/min. The wafer was divided into samples that were 9 mm X 9 mm; these could be used for thickness measurements with a Woollam ellipsometer (M2000 VI with WVASE32 software). A wafer was placed inside the reactor and the area directly underneath the inlets for HF was identified so that the measured ER values can be determined as a function of distance from the inlet. The overall size of the square wafer was about 5 cm X 5 cm. The flow distribution was

observed directly by using the polycarbonate reactor and pure water. Since the HF resistant polymer reactor was operated under identical conditions to those used in the polycarbonate reactor, the same flow distribution should be established. The H/D ratio in these tests was 0.65. Two different etch runs were conducted: one used a 6 min reaction time, 2 min rinsing, 2 min drying sequence and the other used a 14 min reaction, 2 min rinsing, 15 sec drying sequence. The side of the wafer facing the nitrogen inlets (top row in Figure 43 and Figure 44) and the one facing the HF/DI water inlet (bottom row) are included in Figure 43 and Figure 44. The wafer was positioned at the center of the holder. In comparison, the etched thickness in nm for samples etched in a beaker is described by the expression 2.81xtime (min) + 0.49. The results for these two runs are summarized in Figure 43 and Figure 44, with the bold numbers indicating that the inlet is exactly at the center of these locations. It is observed that the etch rate variation across the wafer is negligible and the experimental etch rate results agree within ~10% of those predicted by simulations; this value falls within experimental error for these studies.

17.7	18.2	17.0	18.5	18.8
17.9	16.9	**18.4**	**18.9**	19.5
17.8	17.6	**18.5**	**18.4**	19.1
18.4	17.8	18.7	19.1	19.1

Figure 43 Results of a reactor run showing etched thickness in nm at different positions for the 6 min reaction, 2 min rinsing, and 2 min drying sequence. The box represents the wafer (5X5 cm), numbers indicate the etched thickness; the inlet is exactly at the center of locations marked in bold

41.4	41.7	42.0	42.7	42.2
41.1	41.9	**41.2**	**41.9**	41.7
40.9	38.7	**41.2**	**41.7**	42.0
40.7	41.5	40.3	41.3	41.8

Figure 44 Results of a reactor run showing etched thickness in nm at different positions for the 14 min reaction, 2 min rinsing, and 15 sec drying sequence. The box represents the wafer (5X5 cm), numbers indicate the etched thickness; the inlet is exactly at the center of locations marked in bold

Similar experiments for BPSG etching were performed. However, the doping non-uniformity of BPSG films prevented reliable comparison of the experimental vs. calculated etch rate profiles.

6.3 Conclusions

An experimental reactor system has been assembled within a walk-in fume hood and employed to validate the CFD simulations. Experimental etch rate results agree with predictions from the simulations to within experimental error. This reactor design can be used for any other film (for example ZnO as described in the following thesis chapter) with any other wet chemistry (for example HCOOH). The reactor system can be used in a number of different configurations; for example,

1) One that allows the flow of chemistry through only one inlet hole (blocking other holes),
2) One that allows the chemistry and DIW through only one line,
3) One that allows the chemistry and DIW through one line AND allows the flow to occur through only one inlet hole.

The next chapter describes the use of the ZnO-HCOOH system for in-situ reflectometry implementation using option 2 i.e. allows the chemistry and DIW to flow through only one line unless otherwise indicated.

CHAPTER 7

ER MONITOR DEVELOPMENT

In-situ monitoring of optical constants and thickness of thin films is of interest when investigating the kinetics of film formation and etching as well as in process development for the fabrication of integrated circuits (IC), solar cells and microelectromechanical (MEMS) devices [78,79]. One of the most widely used metrology tools for determination of both optical constants and film thicknesses is spectroscopic ellipsometry (SE). This approach has been used extensively in research and development efforts since a number of SE systems are available commercially and the accuracy of this method for thin film analysis and monitoring is high. Although SE is excellent for ex-situ measurements, use of SE as an in-situ sensor is not always feasible for development or production reactors because of the optical configuration required. The need for an advanced data acquisition system in SE increases the cost and limits the ease of implementation for routine measurements. Sometimes, process equipment must be designed around this monitoring system which may obviate use of the specific equipment configuration of interest thereby limiting applicability of this method in film studies. Some of the problems in implementing SE on the prototype reactor developed in the previous work are given the appendix. Nevertheless, process development and manufacturing operations benefit immensely from in-situ, real-time monitoring/tracking of thin film parameters such as film thickness and optical constants. Alternate in-situ methods are therefore needed. Since optical diagnostic techniques ensure non-intrusive monitoring, these approaches are frequently preferred. Furthermore, computer codes to calculate optical constants and thickness from experimental parameters, although often proprietary, are available; users

can treat this approach as a "black box" if desired. Because the theory of propagation of electromagnetic waves in isotropic multilayered systems has been well developed [72-74,80-82], enhanced fundamental insight and understanding of the monitoring process can be achieved.

Spectroscopic Reflectometry (SR) systems have been used previously to monitor optical constants and/or changes in thickness; as illustrations, the reader is referred to [83,84]. For a nonlinear system such as etching of thin films in which the input parameters such as flow rates affect the etch rate in a non-linear fashion, the Extended Kalman Filter (EKF) is generally considered to be the most popular state estimator. EKF has been implemented in deposition and etching processes for thin films [22,23]. A modified Moving Horizon Estimator (mMHE) has also been developed and has recently been applied to film deposition processes using a deterministic process model [85]. To the authors' knowledge, only single or dual wavelength approaches have been used with sensor models for EKF and mMHE as applied to dry etch/deposition conditions.

In this work, the design and implementation of a sensor model for in-situ monitoring of thickness changes from first principles is described; in addition, it uses EKF, RLS and mMHE for multiple wavelength reflectance spectra in a liquid etch process thus better utilizing the experimental data through the use of both sensor and process models., These algorithms are also compared in terms of robustness and computational time with Least Squares (LS) on reflectance spectra, which is widely used in reflectometry for data

analysis. The initial guess for the state estimators are obtained from a Computational Fluid Dynamics (CFD) model described in detail elsewhere [86].

7.2 Ex-situ implementation of SR

Spectroscopic Reflectometry (SR) is an optical method to determine film thickness from film optical parameters that utilizes only the reflectance spectrum from the sample, thereby avoiding the complex optics required for polarization measurements. SR therefore provides a low cost alternative to SE, especially if the films under investigation are isotropic. Despite the advantages, limitations of SR are well-known. For instance, there is a minimum thickness that can be easily measured (for the current system described below, this value is ~400 nm), and the measurement accuracy is less than that of SE [80] (for the current system ~5 nm). A number of SR commercial systems are available. The SR system employed is portable, occupying an area approximately equal to 15 cm x 15 cm as opposed to ~ a square meter by SE, although current SE systems can be much smaller. Thus, SR can be easily incorporated into a fume hood or other hazardous material containment system. The number of points for tracking/monitoring depends only on the beam size (a few mm^2); hence for our reactor (square shape, ~20 cm x 20 cm), at least seven non-overlapping data points are feasible. As briefly mentioned in the introduction, the reactor has been designed with minimal incorporation of feedback from the sensor system, thus considerably simplifying the overall reactor operation (refer to ref. [86] for more details on reactor design)

7.3 Optical system configuration

The optical components for the system described below are available from Ocean Optics (Dunedin, FL); these consist of a tungsten filament light source (LS-1), a fiber optic

probe (R600, consisting of one read fiber and six illumination fibers (with fiber core diameter of 600 μm, and numerical aperture of 0.22 +/- 0.02 which leads to an acceptance angle of 25.4^0 in air) and spectrometer (USB2000). Ocean Optics software (OOIbase32) has been used to acquire interference spectra. (It should be noted that due to the optic probe design, the angle of incidence is slightly off-normal).

The light source used is incoherent; interference will therefore occur only when the thickness of the medium is less than the coherence length of the light [87]. The coherence length, Δl, is approximately given by $\Delta l = \lambda^2 / \Delta\lambda$

where $\Delta\lambda$ is the resolution of the spectrometer. For the nominal resolution of the spectrometer (0.95 nm) and at a nominal wavelength 600 nm, the coherence length is 0.38 mm. Therefore, only interference from the films much thinner than 0.38 mm is detected.

Before implementing the in-situ optical system, the system was tested ex-situ to better understand the limitations. For this purpose, a simple sample stage capable of x-y-z and tilt movement was designed. This configuration was used to obtain the thickness of boro-phospho-silicate glass (BPSG) films on Si (reflectance spectra shown in Figure 45) and thereby permit thickness comparisons with those determined from ellipsometer measurements. The data were taken at essentially the same locations as those of the ellipsometer. In our studies, only normal incidence has been used although this system can, in principle, be used for non-normal incidence. The windows will decrease the intensity of light; however, since the reflected intensity is normalized, these losses are

compensated and thus have no effect on the results obtained. The compensation formulae are given in the appendix.

Figure 45 shows the measured and simulated reflectance spectra with a water film thickness of 0.49 mm. The water thickness is in the range (0.25 mm - 5mm) of gap spacing between reactor top head and wafer surface, and has been shown to be an important quantity for center to edge ER variation[86]). This thickness is achieved by placing two wafers (each of thickness 0.49 mm) next to each other on the top of sample BPSG wafer. The sapphire window rests on these two wafers and the entire system immersed in water. The probe is adjusted perpendicular to the window by using the tilt arrangement. The size of the beam on the wafer is ~ 7 mm.

Figure 45 shows four curves whose characteristics offer insight into the operation of this system.

1. The curves labeled ‘s’ and ‘p’ overlap with each other at normal incidence in agreement with the literature [73] thus validating the model.

2. The curves labeled ‘aligned’ and ‘mis-aligned’ are the experimental reflectance spectra of the same film, except that the z alignment has been made ‘misaligned’ by one turn of the alignment screw in reflectometric set up for the curve labeled ‘aligned’. On a microscopic level, this has the effect of changing the angle of incidence from 90^0 ie. the probe does not rest exactly on the top of sapphire window as shown in Figure 46, but is at an angle ($<1^0$) off normal. These curves show that the reflectance decreases from the true

value (100%) due to changes in reflection coefficient with angle. Also, this angle may be different from the conditions under which background reflectance spectra is acquired due to experimental errors. The same effect was observed in the reflectance measurement for all films. The fact that this was caused by the parallelism of optical planes was confirmed by forming a water film wedge by placing two planar objects of dissimilar heights on the sample wafer. The reflectance spectra degrade as the parallelism diminishes. True parallelism may not be achieved in the in-situ for a number of reasons, including

a. Inaccuracy in drilling the probe placement point inside the reactor top head (Figure 46)

b. Misalignment of optical probe with window

c. Misalignment of translation stage (described in the section on 'in-situ implementation of SR') with the optical probe

3. The reflectance spectrum (curve labeled 'misaligned') was fitted with a simulated spectrum (of s/p wave) using 'lsqcurvefit' routine in MATLAB. This experiment was repeated for several films in the thickness range 200 nm-1000 nm. Results revealed that the actual thickness values as determined by ellipsometry, cannot be determined more accurately than 5 nm with the existing configuration. This is due to several factors such as inaccuracies inherent in the set up (e.g., alignment of probe with window, optic probe design) and noise in the data, and therefore places an upper limit on the accuracy of thickness estimation from in-situ data. The resolution degrades when the film thickness

decreases; our experiments have demonstrated that this SR configuration can be used to measure films of thickness > 400 nm.

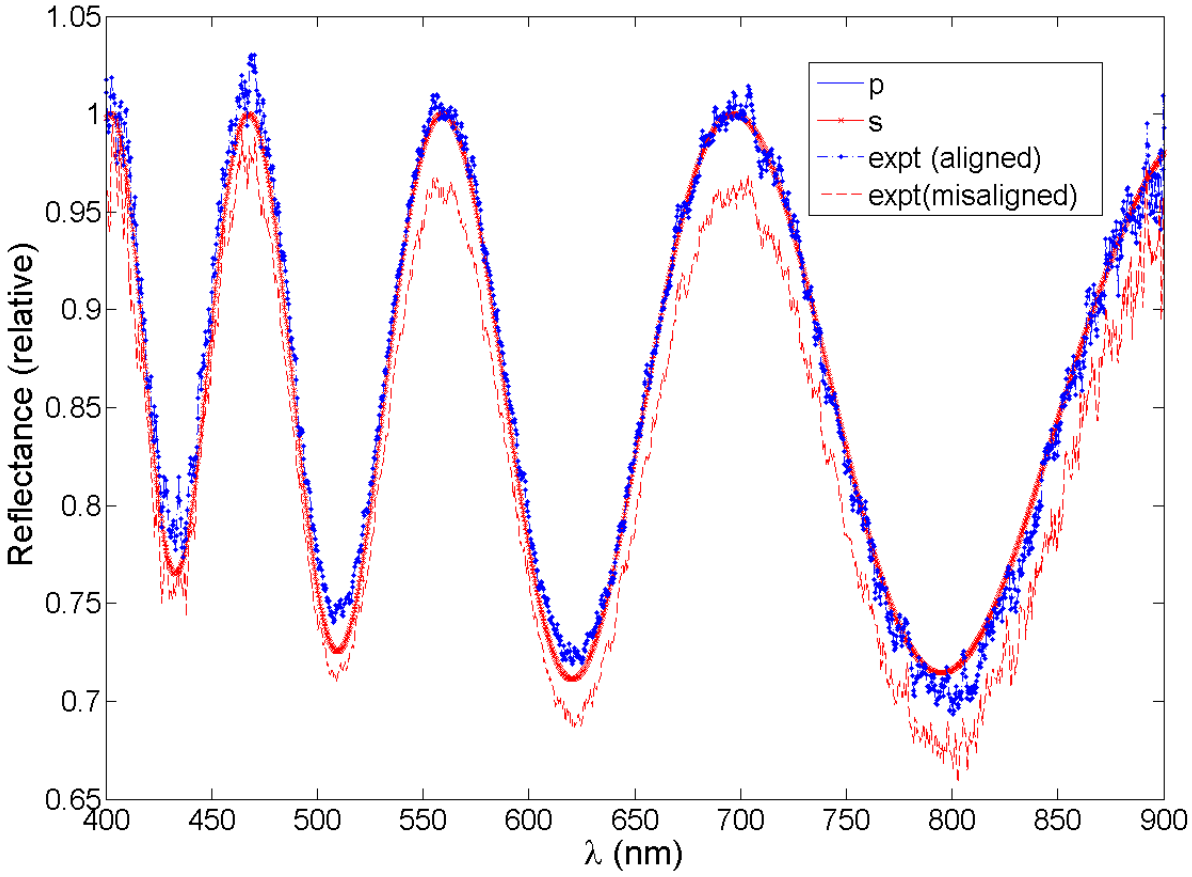

Figure 45 BPSG film (thickness of 955 nm), note that 'p' and 's' curves overlap

7.4 In-situ Implementation of SR

A schematic of the experimental configuration used for in-situ implementation of SR for a short contact time reactor is shown in Figure 46. Recently, Lam Research Corporation (LRC) designed and built a single wafer short contact time reactor for substrate cleaning/etching [66,88-90]. A CFD was used to design a miniaturized, simplified version of this short contact time reactor capable of processing 2x2 cm^2 substrates. The reasons for

this design configuration have been described in detail in a previous publication [86]. Apart from process parameters such as flow rate and concentration, the gap spacing between the reactor top head and the wafer surface (a geometric parameter) has been shown to be an important quantity that establishes the difference between etch rates at the center and at the edge of the wafer. Figure 47 shows a top view of the experimental reactor. The reactor top head is held securely on a support while the wafer stage (shown in part) is moved with a micrometer via a vertical translation stage. Figure 37 shows the micrometer system used to measure spacing of optical surfaces. The accuracy of the micrometer is ~5 microns; hence, the accuracy of the entire system is expected to be 50 microns or less. Taking into account the size of the sapphire windows, there are seven possible geometrical non-overlapping probe placement points near the inlet. One of these points was chosen for probe placement. Sample wafers with known film thickness in the range 400nm-1000nm were measured in order to confirm that the correct thickness, within experimental error, was determined with the SR configuration.

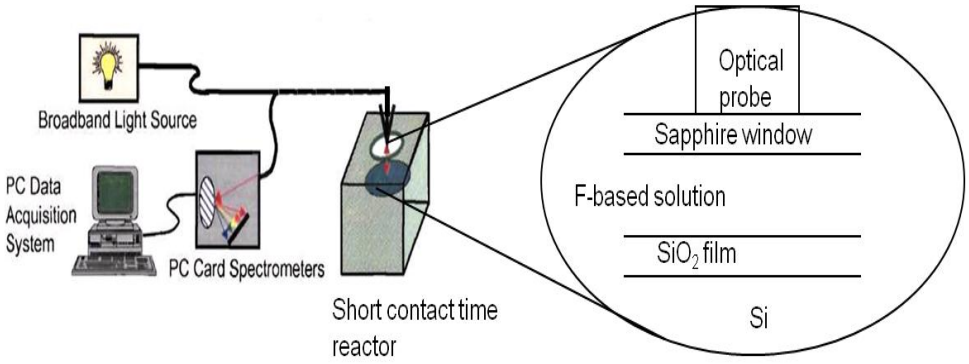

Figure 46 In-situ reflectometric set up (adapted from literature [83])

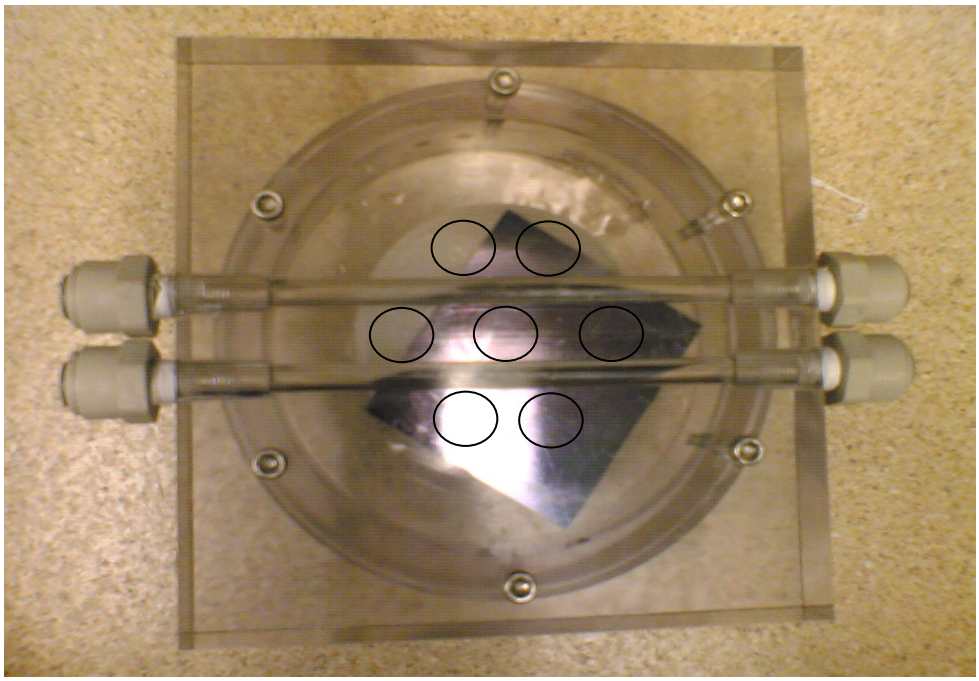

Figure 47 Reactor top head showing some of the possible placement locations for the reflectometric probes

It should be noted that the reflectometric technique implemented here is independent of the type of reactor and thus can be applied to any reactor where in-situ monitoring by ellipsometry is infeasible due to geometrical limitations or economics.

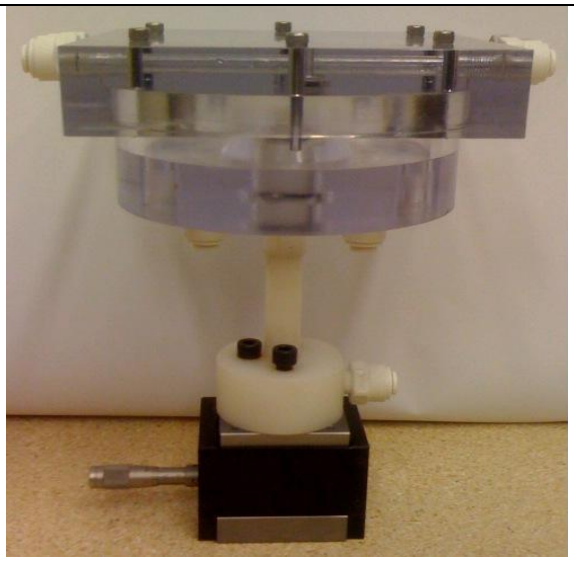

Figure 48 System for measurement of gap height

7.5 Case Study: ZnO Etch Rate measurements

ZnO is gaining popularity as a transparent conductive oxide film because it is non-toxic, chemically stable, inexpensive and abundant. ZnO etches readily in acid solutions even at dilute concentrations leading to uncontrollable etch rates [91]. Recently, wet chemical etching of Ga doped ZnO has been studied using formic acid [92]. Therefore, formic acid was used as an etchant for ZnO to investigate different algorithms for use with SR.

7.6 Experiments

ZnO films of ~600 nm thickness were RF sputter deposited onto a silicon substrate. The conditions for deposition were: base pressure = $2*10^{-5}$ torr, pressure = 6 mTorr, 50% O_2 + 50%Ar, power = 140W, 180 min deposition time at a temperature of 25^0C. The thickness values were measured by ellipsometry before and after the ER experiment, approximately at the same location where the reflectometric probe was placed. The reflectance data for in-situ experiments was acquired every second, although experimental data can be acquired as fast as tens of milliseconds. However, our trial

experiments showed that one second data acquisition speed is sufficient for ER and thickness prediction because of the relatively slow ER). Table 12 shows the conditions for the in-situ experimental and simulations runs.

Table 12 Details of the in-situ experimental and simulation runs

Run	Time reaction (sec)	Formic acid conc (mM)	Flow rate (ml/min)	Initial thickness (nm)	Final thickness (nm)	Initial thickness guess (nm)	Initial ER guess (nm/min)
1	190	2	200	515	430	515	60
2	110	2	300	520/490	470	530	60
3	400	10	100	630	0	630	160

7.7 Validation of RLS, EKF and mMHE

A hypothetical case was simulated in which the initial etch rate (ER) of a ZnO film of starting thickness 900 nm was 30 nm/min. The ER and thickness as a function of time were simulated based on a simple process model. Optical constants of ZnO were determined using ex-situ ellipsometry where data were curve-fit to yield the following Cauchy relationship (λ is in nm)

$$n = 1.8917 + \frac{0.04519}{\lambda^2} + \frac{0.0004612}{\lambda^4} \tag{19}$$

$$k = 0 \tag{20}$$

Optical constants were assumed to be independent of film thickness. The simple process model invoked was

$$\begin{pmatrix} h \\ ER \end{pmatrix}_{t+1} = \begin{pmatrix} 1 & -\Delta t \\ 0 & a \end{pmatrix} \begin{pmatrix} h \\ ER \end{pmatrix}_{t} \tag{21}$$

Where Δt=1 min and 'a' is the parameter used to assess the process model mismatch. For all cases, a value of a=0.99 was used for simulation to generate the optical reflectance spectra that were then analyzed and fit using the various thickness analysis/estimation techniques. The value of 'a' used by the estimators was varied for different estimation cases. There was no sensor noise used in any algorithm. The tuning parameters for both EKF and mMHE were as shown in Table 13 unless otherwise noted. The strategy for choice of these parameters is explained in more detail in the following. For both mMHE and RLS, the unconstrained optimization routine 'fminunc' in MATLAB was used. Constrained optimization routines ('fmincon'in MATLAB) can also be used although a longer computational time is required. The wavelength range was 400 to 925 nm in increments of 25 nm.

Table 13 Tuning parameters for EKF and mMHE algorithms

Matrix	Value
P	$\begin{pmatrix} h_{initial} & 0 \\ 0 & ER_{initial} \end{pmatrix} \cdot 10^{-2}$
Q	$\begin{pmatrix} 1 \cdot 10^{-4} & 0 \\ 0 & 1 \cdot 10^{-4} \end{pmatrix}$

R	Identity matrix (n X n)x10^{-6} where n is number of wavelengths used

Figure 49 shows that all algorithms can predict thickness extremely well. ER estimation is poor initially for EKF, but is improveed as a function of time; by comparison, the estimation for mMHE, LS and RLS is good from inception.

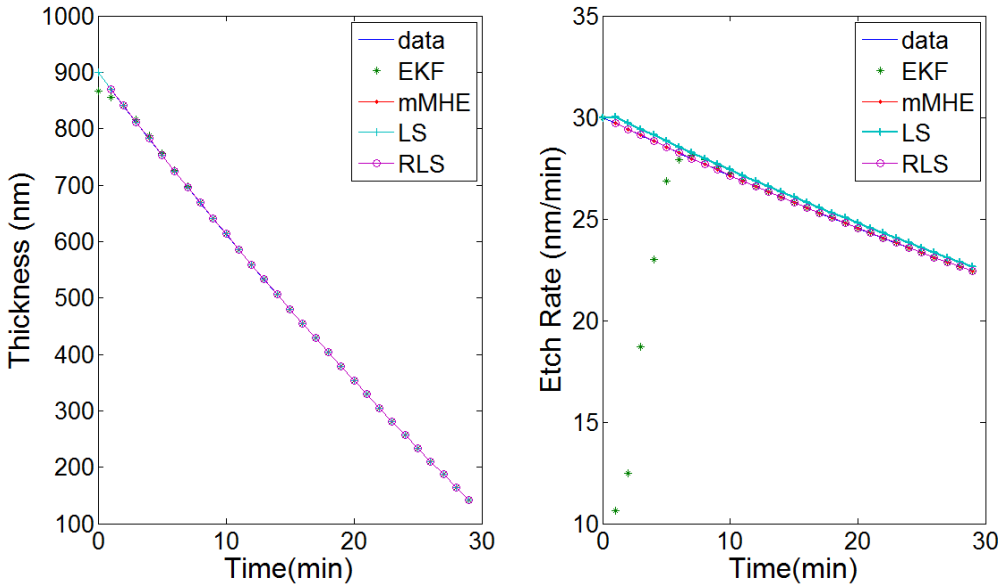

Figure 49 Simulated thickness and ER variation with time for ZnO film, a =0.99 for estimator (no process model mismatch), initial guess = [850, 30], m=2

The value of 'a' was varied over the range from 0.9 to 1 to determine the influence of process model mismatch on the estimator performance. It should be noted that the value of 'a' does not affect LS since it does not depend on the process model used. The e^2 value for LS is given as a reference for the comparison of various estimators and they change because of change in the random initial guess as shown in Table 14. From comparison of Figure 49 and Figure 50, the ER prediction of mMHE and RLS deteriorates with

increasing process model mismatch whereas EKF is relatively insensitive to this change. This is shown by increased deviation from the simulated ER for mMHE/RLS whereas for EKF this deviation is less pronounced. Also, the ER prediction for EKF is underestimated in the beginning of the simulation, which corresponds to an underprediction of the thickness. This large deviation contributes to the higher e^2 value as shown in Table 14 and explained in detail below. The initial guess for these cases was [850, 30].

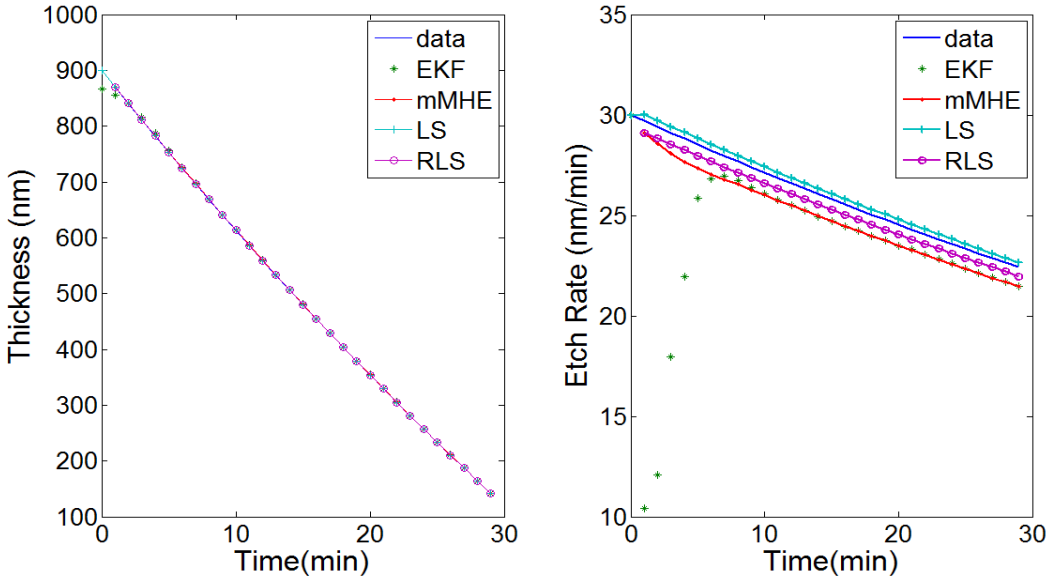

Figure 50 Simulated thickness and ER variation with time for ZnO film, a =0.97 for estimator, initial guess = [850, 30], m=2

To quantify the accuracy of our estimates, same approach as that of [85] was used**.** The initial guess is expressed by $x_{1,p} = x_{i,p} r_p$, where *r* denotes an 2X1 random vector, and *p*=1, 2. Each element of *r* is taken from a Gaussian distribution having a mean of 1 and a standard deviation of 0.05. Consequently, the initial guess is approximately 5% offset from the actual initial state. The estimation error for each element *x* of the state vector was defined as

, $$e^2 = \sum \left[\; x - x_{est} \; / \; \bar{x} \; \right]^2 \quad (22)$$

where $\bar{x}$ is the mean value of the true state and is used to normalize the estimation error so that all states are equally represented. To calculate the total error, e^2 values were summed over all states and over all time steps for five random initial guesses. The results are shown in Table 14 where in general, the error in prediction increases with increasing process model mismatch. The error for EKF is the highest because of the large undershoot in EKF prediction at the start of estimation as noted in previous section and thus have less dependence on value of 'a'. The error for LS is the independent of 'a' since it uses only the sensor model invoked to generate the simulated data and thus changes with only change in initial guess.

Table 14 'e^2' value comparison for different algorithms at various values of 'a' for five random initial guesses, m=2,

	'e^2'			
'a'	EKF	RLS	mMHE	LS
0.99	0.70082	0.0040555	0.0040403	0.083468
0.98	0.5987	0.051961	0.10898	0.13918
0.97	0.74442	0.10653	0.21922	0.05736
0.96	0.71938	15.1044	0.32818	0.07338

The primary advantage and disadvantage of mMHE/EKF compared to LS/RLS is that one must specify P, Q and R matrices based on an understanding of dominant sources of uncertainty in the process. $P_{1/0}$ is the initial covariance matrix, Q is the covariance matrix

for process uncertainty and R is the convariance matrix for sensor model uncertainty. The value of P (10^{-2}diag(x_i)) used indicate that one expects the initial guess to be 10% away from the true value. This value can be adjusted depending on the confidence on the initial thickness and ER values. The initial thickness value can be measured accurately by ellipsometry ex-situ and using the same optical constants relation in reflectometry as that used in ex-situ ellipsometry, the initial thickness estimation can be precise. It is more difficult to obtain an ER estimate under the process conditions of concentration and flow rate. As described in detail below, CFD model is used to obtain a more accurate guess. It is generally difficult to quantify the effect of an incorrect process model. Since process dynamic model of the algorithms assume different value of 'a' than that used in generating the simulated data, the effect of a variation in Q was investigated. Comparison of Figure 50 with Figure 51 demonstrates that the value of Q has less effect than that of an incorrect process model for all algorithms, thereby emphasizing the importance of a correct process model. A small value for R was chosen due to the existence of a well-validated sensor model. (10^{-6} value of variance R represents an error in the third decimal place for sensor model, which is quite small). It is expected that for thinner films, this assumption may need to be modified. Also, as noted in ref [85], as long as tuning matrices correctly specify which aspects of model should be considered with highest confidence and which are less accurate, the exact values of tuning matrices are less important. It should be noted that since R is a tuning (scaling) matrix in the algorithm, its value can affect the optimizer performance as discussed below.

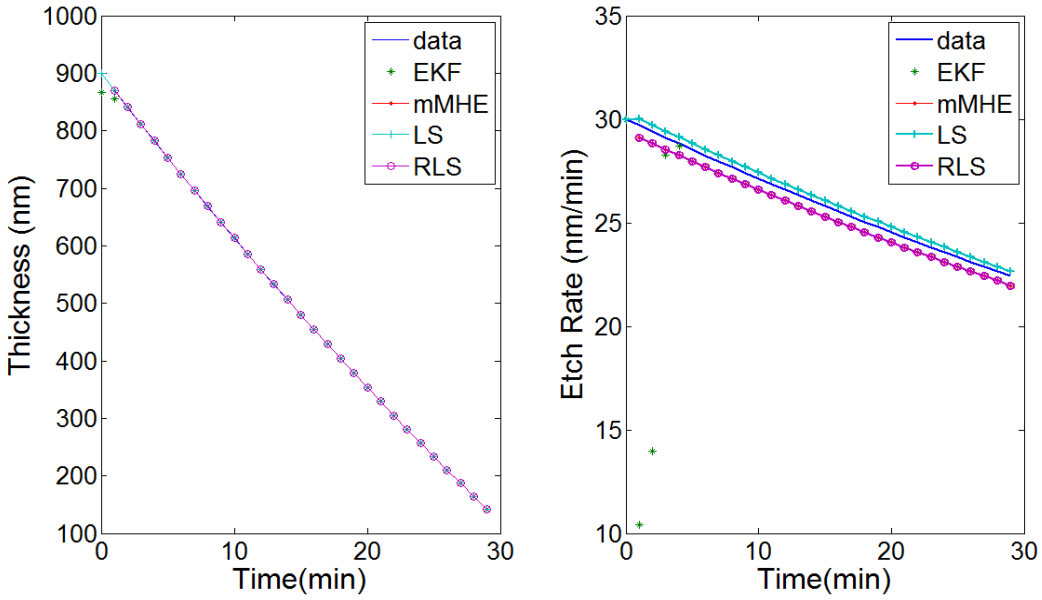

Figure 51 Simulated thickness and ER variation with time for ZnO film, a =0.97 for estimator, initial guess = [850, 30], Q = [1e-4 0, 0 1e0], m=2

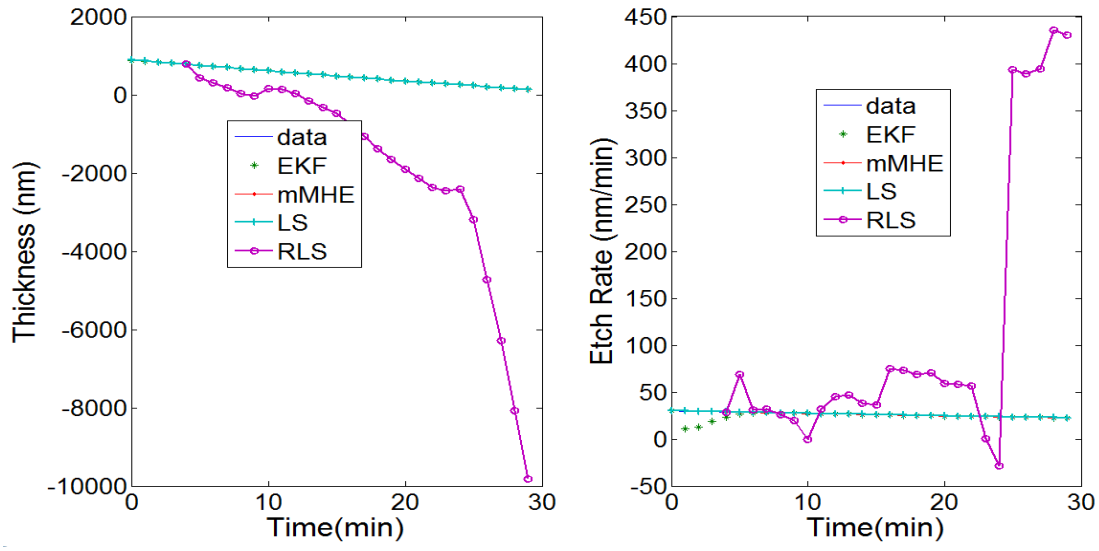

Figure 52 Simulated thickness and ER variation with time for ZnO film a=0.99 P, Q as in **Table 13**, initial guess=[850,30], m=5,

Comparison of Figure 49 and Figure 52 shows that the error in estimation increases with increasing values of m (the horizon size) for RLS. It should be noted that the RLS fails

prematurely whereas the other estimators track the thickness and ER. This may be due to the use of function ‘fminunc’ used for unconstrained optimization[93]. It is expected that the performance of each algorithm can change dramatically with the use of different optimization routines as well as different optimization class (constrained vs. unconstrained).

..

Figure 53 shows the comparison of optimization routines for RLS and mMHE for the same conditions as those shown in Figure 49 for different values of horizon length. (The e^2 (error) value is computed as defined in Table 14). It shows that the errors for RLS are widely different from each other depending on the routine. A comparison of constrained and unconstrained routines shows that although the error for ‘fmincon’ is lower than that of ‘fminunc’ for RLS, magnitude is consistently high for both routines . The error for mMHE using ‘fmincon’ is nearly of the same magnitude as that of RLS using ‘fmincon’. The routine ‘fminsearch’ uses a derivative free method for the unconstrained optimization problems whereas both ‘fminunc’ and ‘fmincon’ use gradient based methods. [93]

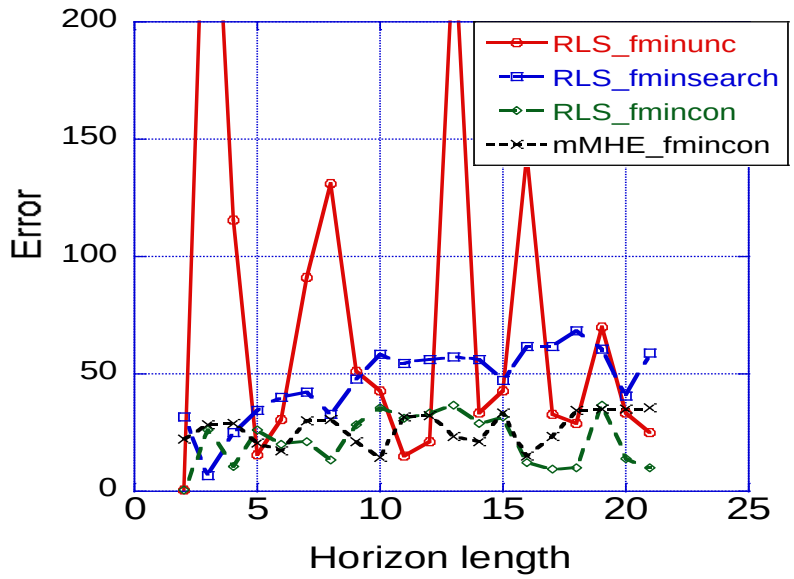

Figure 53 Comparison of error estimates from various algorithms using different optimization routine, $\Delta\lambda$=25 nm, and the initial conditions were [850,30]

Comparison of Figure 53 with Figure 54 shows that for mMHE, the errors for unconstrained routines is much lower than that of constrained routines and errors are almost identical for unconstrained routines using identical conditions as that of Figure 53. It should be noted that the values for 'fmincon' and 'fminunc' at m=2 for RLS in Figure 53 are of the same magnitude as that for mMHE using 'fminunc' in Figure 54. One of the limitations in using 'fmincon' for mMHE is due to the scaling of optimization objective function by the tuning matrix R, a value of 10^{-6} is too low and the objective function is badly scaled. Increasing this value to 10^{-4} (decreasing the confidence in sensor model) decreases the error for mMHE using 'fmincon' by an order of magnitude as shown in Figure 54. This change of R value is the only difference in 'fmincon' using mMHE in Figure 53 and Figure 54. However, the errors are still an higher than that of unconstrained routines.

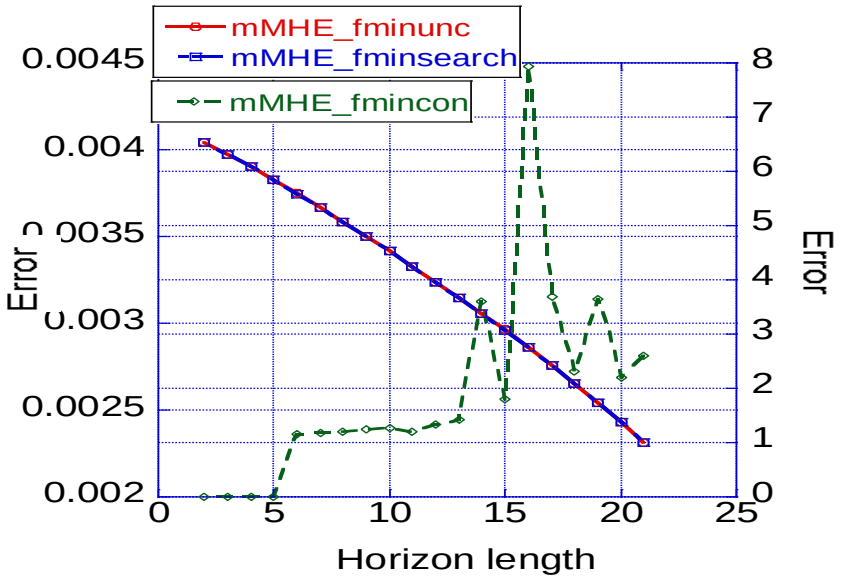

Figure 54 Comparison of error estimates from mMHE using different optimization routine, errors for 'fmincon' are on secondary (right hand) y-axis

To further understand the difference between constrained and unconstrained routines, a simulation was carried out with $\Delta\lambda$=5 nm and initial guess of [890, 30] was used in the estimators. Figure 55 shows that the performance of all routines for mMHE is almost identical. The errors for RLS are much higher than that of mMHE although the horizon length at which RLS starts to fail is higher than that in Figure 53. The errors till m=4 for RLS are of the same magnitude as that of mMHE. It should be noted that the computational time for constrained routines is higher than that of unconstrained routines.

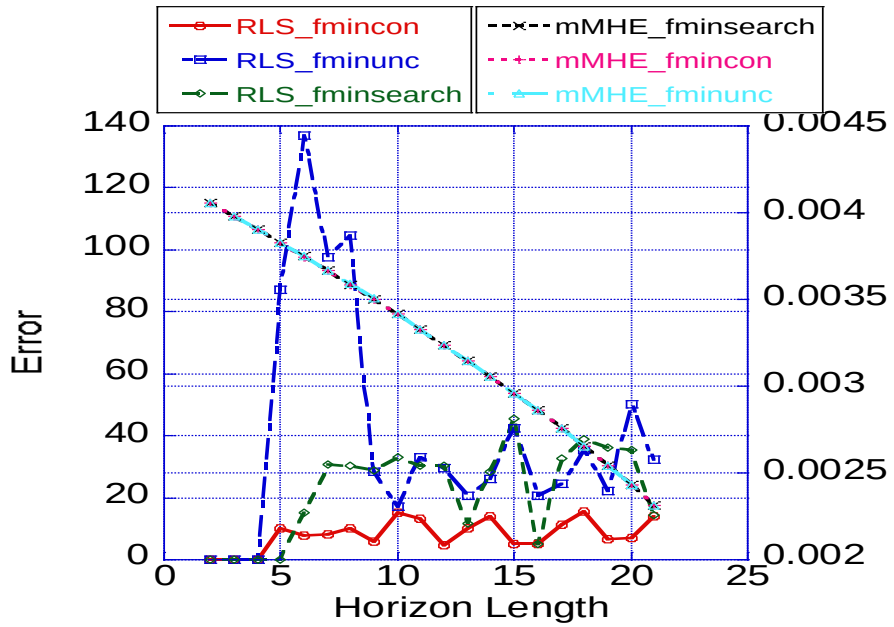

Figure 55 Comparison of error estimates from various algorithms, the values for mMHE are shown on the secondary (right hand) axis, $\Delta\lambda$=5 nm, and the initial conditions were [890,30]

To maintain the consistency of comparison in further validation of our algorithms and in the work that follows, the same unconstrained routine 'fminunc' for both mMHE and RLS and a horizon length of m=2 is used. It should be noted that the choice of horizon length affects accuracy and computational time with increasing horizon length leading to increased computational time. A study of effect of horizon length on e^2 value has been reported previously in ref [85] for a dual wavelength reflectometry where e^2 showed a minima with increase in horizon length. The initial decrease was due to incorporation of priori data, however at longer times, the assumption of a deterministic process model in mMHE is inappropriate, thus e^2 increased . In this work, the e^2 value was nearly constant indicating a deterministic process model. The optimum horizon length is expected to be

different depending upon the system (for example ZnO as compared to other films) as well as the specific etching conditions. This is because of the trade-off of higher computational time introduced by using higher number of wavelengths and longer horizon size at a constant data acquisition rate with the accuracy provided by them as explained in the multi-wavelength experimental section below,.

Comparison of Figure 49 and Figure 56 indicates that the initial guess (incorrect by 10% of the actual value) also plays an important role in the ER/thickness tracking. It is expected that the prediction will deteriorate with increasing process model mismatch and this trend should become worse with an inaccurate initial guess. Again, it should also be noted that the effect of thickness offset in the initial guess is more than that of ER offset. This is expected for a low ER film, since ER enters the process model indirectly through film thickness in the sensor model. The effect of process model mismatch at longer times is manifested in the form of a larger thickness deviation from the true value which leads to larger deviations in the reflectance spectra.

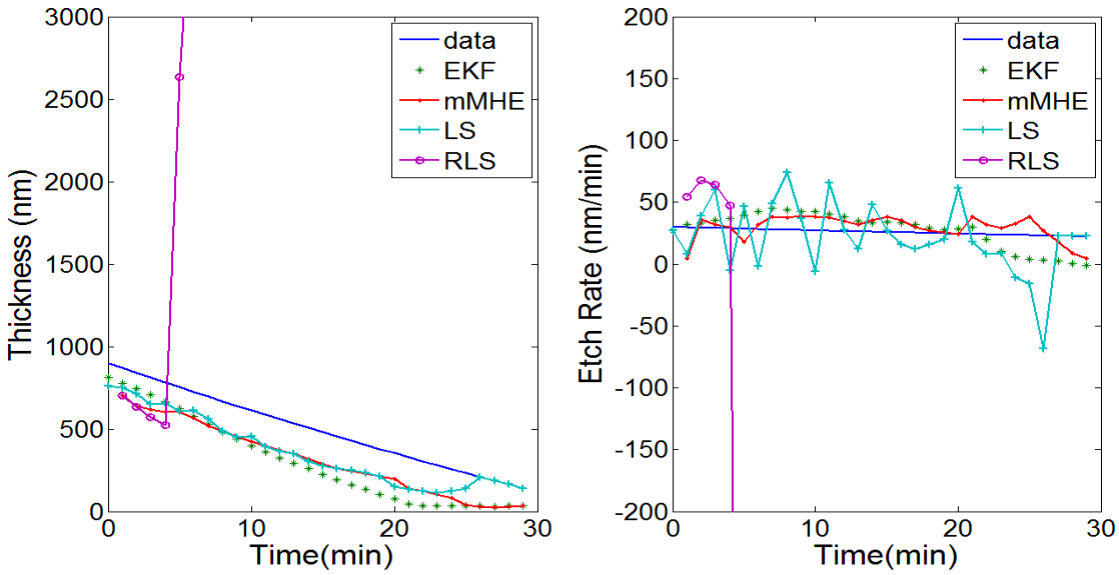

Figure 56 Simulated thickness and ER variation with time for ZnO film, a =0.99 for estimator, (no process model mismatch), initial guess = [820, 27] , m=2

When evaluating data during manufacturing processes, it is generally assumed that the ER is constant with time. While this is a reasonable assumption for a well-characterized process, it can be a very conservative assumption for a new process, especially when the effects of all process parameters are undetermined. It such a case, the process model mismatch combined with an incorrect initial estimate can lead to erroneous predictions. To get a better estimate of initial ER, contours of reaction rate from a CFD model were subsequently used. A CFD model has been developed using the commercial tool Fluent® for the wet etching of various films in the reactor shown in Figure 47. CFD modeling details have been described elsewhere [86]; thus in the following only the information relevant for this study is presented. An improvement relative to the procedure used in this paper would be the implementation of a simplified process model in the estimator model

which can describe this variation. However, this is not a subject that will be addressed in this paper.

7.8 CFD process modeling

Reaction of ZnO with HCOOH is assumed to be described by [91]

$$ZnO + 2HCOOH \rightarrow Zn(HCOO)_2 + H_2O \quad (23)$$

In order to determine the concentration dependence of ER, ZnO wafers of 1cm x 1cm were immersed in a vessel with a stirrer spinning at a particular rpm and a solution with a specified etchant concentration. Thickness values were measured before and after etching using an ellipsometer. Stir rates of 500 rpm, 1000 rpm and 1500 rpm were investigated and the ER (nm/min) plotted against rpm. Even at 1500 rpm, the ER continued to increase indicating that the reaction was still mass transfer limited as shown in Figure 57.

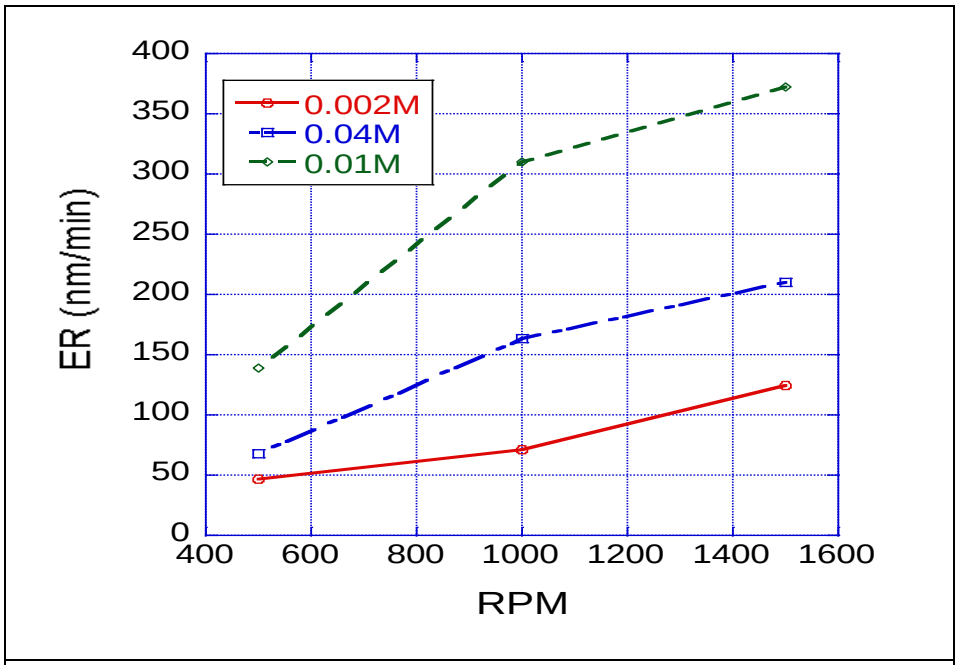

Figure 57 ER variation as a function of rpm and concentration

The etch rate for the reaction in nm/min is changed to the units of kg/(m^2.sec) by multiplying the etch rate in nm/min by the density of ZnO (assumed to be 5000 kg/m^3). A

plot of ER of ZnO in kg-mol/(m^2.sec) vs. concentration of HCOOH in kg-mol/m^3 gave the reaction rate constant (slope) in units of kg-mol ZnO.m/(kg-mol HCOOH.sec). The experimentally determined ER at 1500 rpm as a function of formic acid concentration is shown in Figure 60). The rate expression is written as

$$r_{ZnO}(kgmol/(m^2.\text{sec})) = kC_{HCOOH} \qquad (24)$$

where k is the reaction rate constant and C_{HCOOH} is the concentration of formic acid in kgmol/m^3. It should be noted that the reaction shown is a stoichiometric reaction. First order etch kinetics in formic acid concentration were assumed for the surface reaction of ZnO. As seen from Figure 58, a second order rate expression in C_{HCOOH} gives a negligible and negative dependence on C_{HCOOH} and thus may not be valid. If one assumes that the reaction rate expression is given by

$$r_{ZnO}(kgmol/(m^2.\text{sec})) = kC_{HCOOH}{}^{n} \qquad (25)$$

A log-log plot of C_{HCOOH} with the reaction rate should give 'n' (the order of reaction) as the slope of a linear plot. As shown in Figure 59, the slope is 0.72 which is closer to first order kinetics.

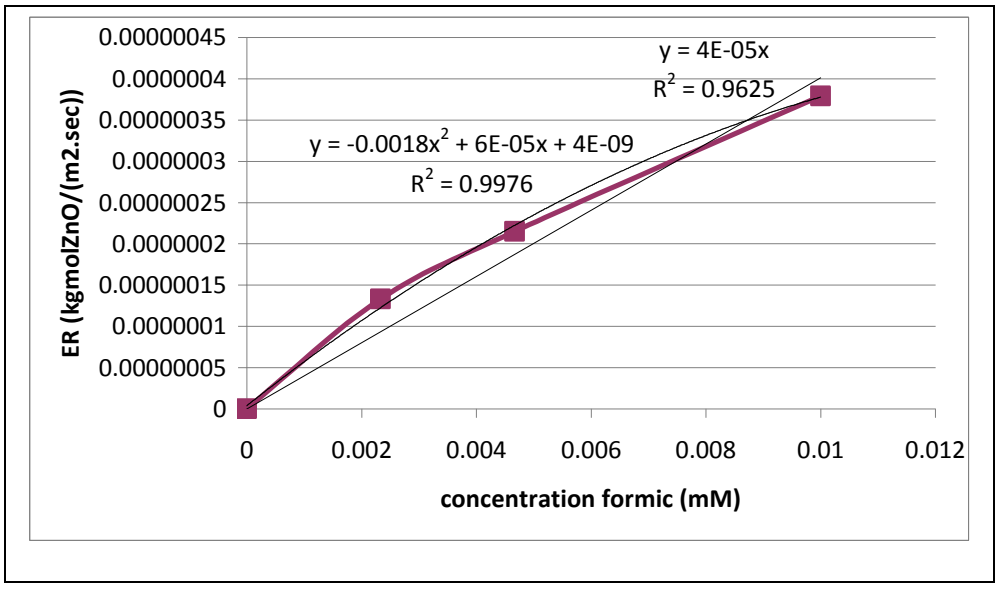

Figure 58 reaction kinetics determination, both first order and second order fit to the data is shown

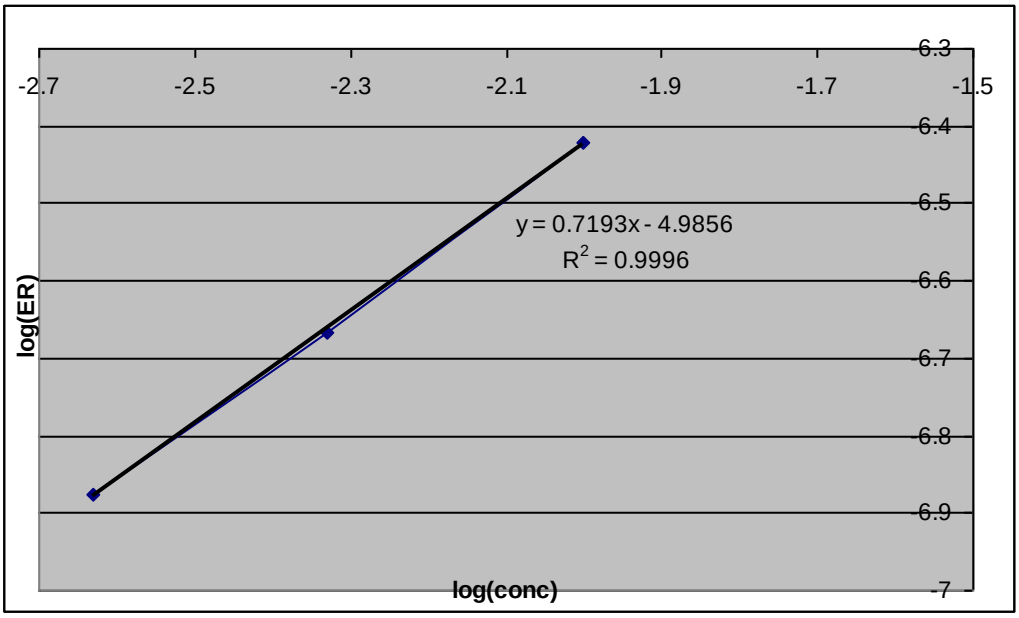

Figure 59 Log-log plot of C_{HCOOH} with reaction rate

The observation that ZnO etching is mass transfer limited for a range of acids and concentrations is in agreement with previous reports [92,94].

The commercial CFD modeling software, Fluent has been used in this study. In Fluent, a reaction mixture is defined to be composed of species that are involved in the reaction(s) under consideration. Pure substance properties for ZnO and HCOOH were obtained from [95]. The properties of zinc formate were estimated using Joback's method [96].

Mass diffusivity of all species is assumed to be 5x $10^{-5}cm^2$/sec which is the order of magnitude diffusivity for liquids [97] The density of the mixture is calculated from a

volume-weighted mixing law while the viscosity is calculated from mass-weighted mixing laws. In the species transport model, inlet diffusion was activated. The mass deposition source of the wall surface reactions is invoked to take into account the effect of surface mass transfer in the continuity equation. An energy balance is included in the simulations with standard state enthalpy and entropy of ZnO, HCOOH and water obtained from [98]. The required properties of $Zn(HCOO)_2$ are estimated from previously published data [96].

Figure 61 shows the simulated ER profile, where the geometry simulated is one-quarter of a two inch diameter wafer. For these simulations, the ratio of the diameter of the inlet (D) to the spacing between the reactor top head and the wafer surface (H) was 0.5, which corresponds to the experimental values for our reactor. The influence of this ratio on ER contours has been described previously (11) and so will not be repeated here. The value shown by the probe placement contour as indicated in this figure was used as the initial guess by EKF, RLS and mMHE as described in the next section. It should be noted that the ER variation from center to edge of the wafer is non-linear; therefore, an initial guess obtained from an average of these two values will be erroneous. Similar procedures to those described above were used for other experimental runs.

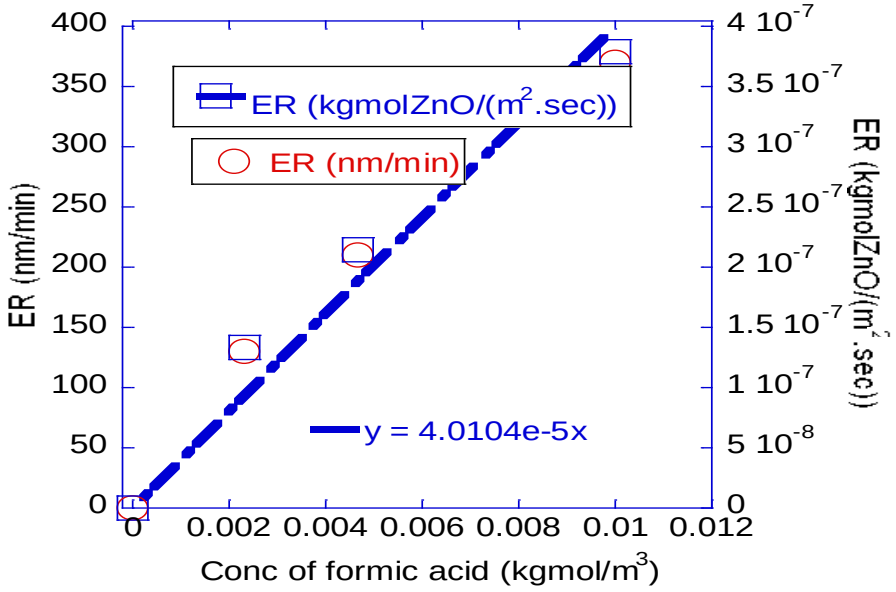

Figure 60 Reaction rate determination at 1500 rpm, the red circle is ER in nm/min, the blue square is ER in Kgmol ZnO/(m^2.sec) and the regression line is the best fit for the ER in Kgmol ZnO/(m^2.sec) vs. C_{HCOOH} plot

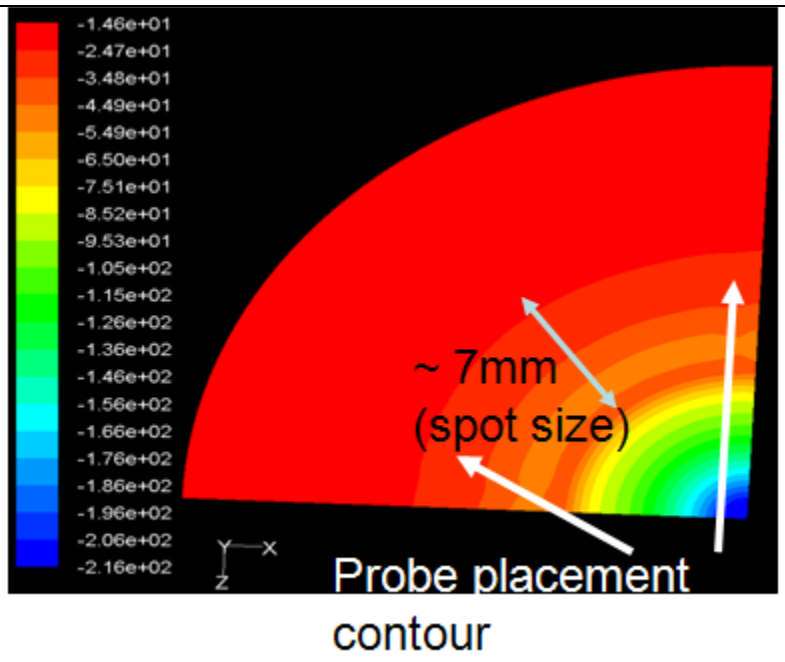

Figure 61 ER contours for run 1 in nm/min

7.9 In-situ experiments

For all cases investigated, the process model was assumed to be

$$\begin{pmatrix} h \\ ER \end{pmatrix}_{t+1} = \begin{pmatrix} 1 & -\Delta t \\ 0 & 1 \end{pmatrix} \begin{pmatrix} h \\ ER \end{pmatrix}_{t} \tag{26}$$

and initial values of the thickness were obtained from ex-situ ellipsometry. Initial guesses are as listed in **Table 12** and the tuning matrices are given in **Table 13**. From the reflectance spectra acquired each second, data was extracted at a time interval of Δt which is indicated in the simulation results along with the horizon length used for each simulation. It should be noted that the data can be acquired from spectrometer as fast as tens of milliseconds. r

7.9.1 Dual wavelength results

The wavelengths considered are [450, 650]. From the experimental relative reflectance spectra, only values corresponding to these wavelengths were extracted. Figure 62 presents thickness and ER variation for the dual wavelength studies for run 1, and shows that all the algorithms fail to track thickness and ER. It is noted that this trend may change depending upon the set of wavelengths selected. Nevertheless, the conclusions do not change since two wavelengths are not able to capture the oscillations in reflectance spectra. Since the best set of wavelengths is not known beforehand and a large number of wavelengths are available in SR, more wavelengths should be included for improved estimation.

Single wavelength ER monitors are also used, however, as noted in [83], this method has several disadvantages. One of the point applicable here is the lack of a flat region in the reflectance versus time spectra, (since thickness has not reached to zero) hence maxima/minima can not be assigned peak numbers.

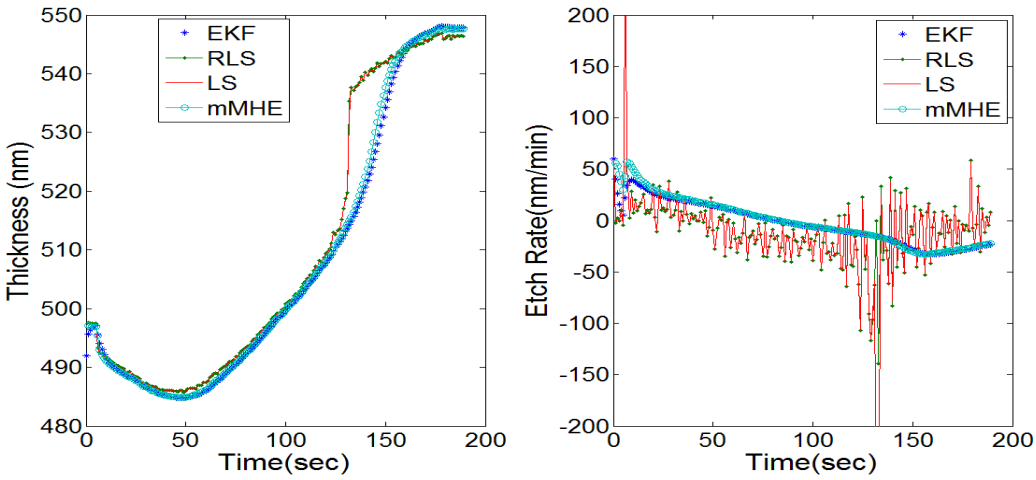

Figure 62 In-situ ER and thickness variation with time for ZnO film (run 1), dual wavelength [450 650], m=2, Δt =7 sec

7.9.2 Multiwavelength results

The wavelength range studied was between 400 nm and 925 nm with an interval of 25 nm. Figure 66 to Figure 68 shows the thickness and ER variation with time as determined by the different algorithms. Results indicate that there is good agreement among the values for thickness and that the predictions are good in-spite of the fact that the initial guess in ER was far from the true value as indicated in **Table 12**. The ER prediction is, however, different for each of them, although EKF quickly recovers to the actual ER value after an initial guess which is about twice that of the actual value. This also shows the sensitivity of EKF to the initial guess values. Figure 68 shows that mMHE fails to predict the thickness and ER after ~300 sec; for other algorithms, this time is ~350 sec. As discussed in the section on in-situ implementation of SR, our sensor system cannot accurately track thickness values <300 nm and therefore contributes to both incorrect thickness and ER prediction.

In all three cases, (Figure 66 to Figure 68), the mMHE /EKF predicts thickness and ER values reasonably well and its response is less oscillatory than that of LS/RLS. However, the computation time for mMHE is about an order of magnitude higher than that for EKF as shown in Table 15 on a 2 GHz, 2.038 GB RAM system. The computational time is crucial in systems such as photoresist dissolution where the rates of dissolution are very fast (~order of magnitude higher). The choice of Δt depends upon the computational time

involved (which in turn is decided by the algorithm used and the specific parameters therein), rate of data acquisition and film ER. It should be noted that the decision of which algorithm to use should then be based on sampling rate and the number of wavelengths required. Also, since mMHE/RLS relies particularly on the accuracy of the process model, its prediction is poor if the quality of process model is poor. For real time applications, it is desirable that the computational time is an order of magnitude lower than rate of data acquisition (Δt =7 sec in Table 15). From Table 15, it is seen that at 5 nm resolution in wavelength, the total computational time for mMHE is an order of magnitude less than the total run time (400 sec) with the inherent assumption that the computational time scales linearly with the run time.

Table 15 Comparison of total computation time in sec for total span of run 3 for all algorithms, m=2, Δt =7 sec,

$\Delta\lambda$ (nm)*	EKF	RLS	mMHE	LS
50	0.388	6.642	8.102	4.5109
25	0.4806	7.8925	10.4106	5.044
8	0.99956	15.767	23.478	8.288
5	1.7185	23.20793	38.8594	11.6595

*The wavelength spacing is not constant between two consecutive wavelengths due to data acquisition from spectrometer and the numerical value is an approximation

From Figure 63, it is seen that the change in minima at ~415 nm at an interval of Δt=7 sec is ~ 5nm which can be detected at a resolution of $\Delta\lambda$=5nm. This approximate criteria

was also used as a means of selection of Δt before any estimation study was carried out. It should be noted that in a typical reflectance spectra, the maxima are more widely separated at higher wavelength region.

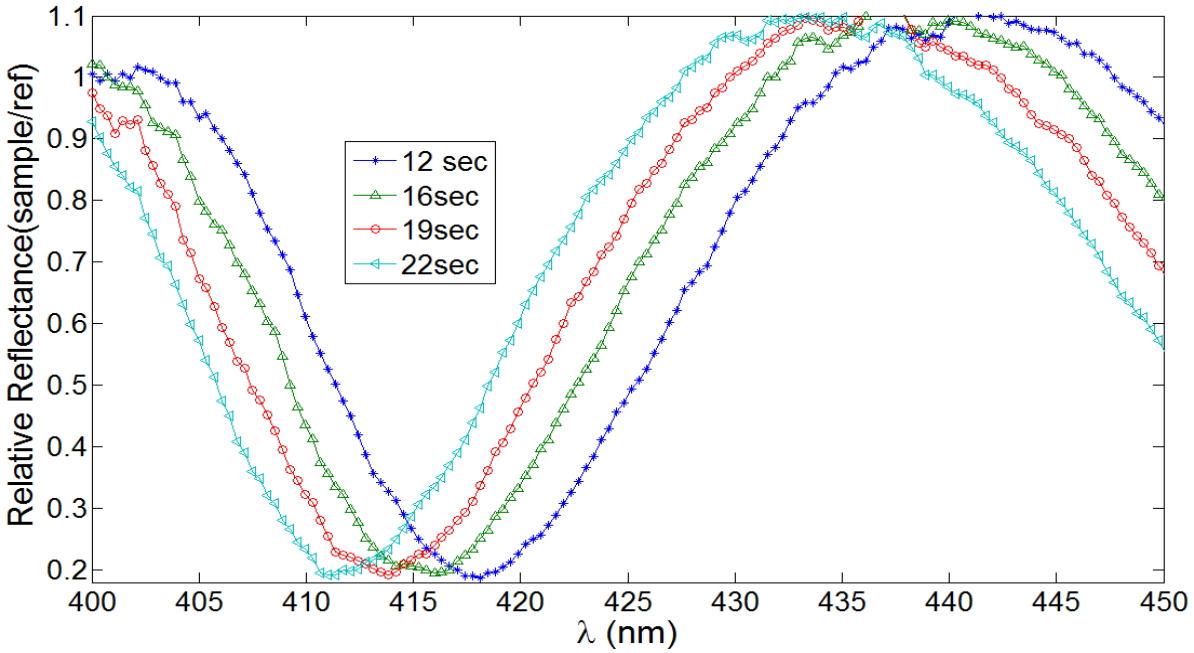

Figure 63 In-situ relative reflectance spectra (run 3) at different times from the start of the run for 400-450 nm range

Figure 64 shows that with increase in Δt, the prediction of ER by EKF starts to smoothen out although the maximum amplitude of oscillations is <4nm/min. In order to get a better match between the ER prediction at, say, t=100 sec for both Δt=1sec and 10 sec, one needs to use a higher wavelength resolution. This is shown in Figure 65 where Δλ = 5nm gives a better match for various Δt. These results are representative for all other estimators and they are not shown here for brevity.

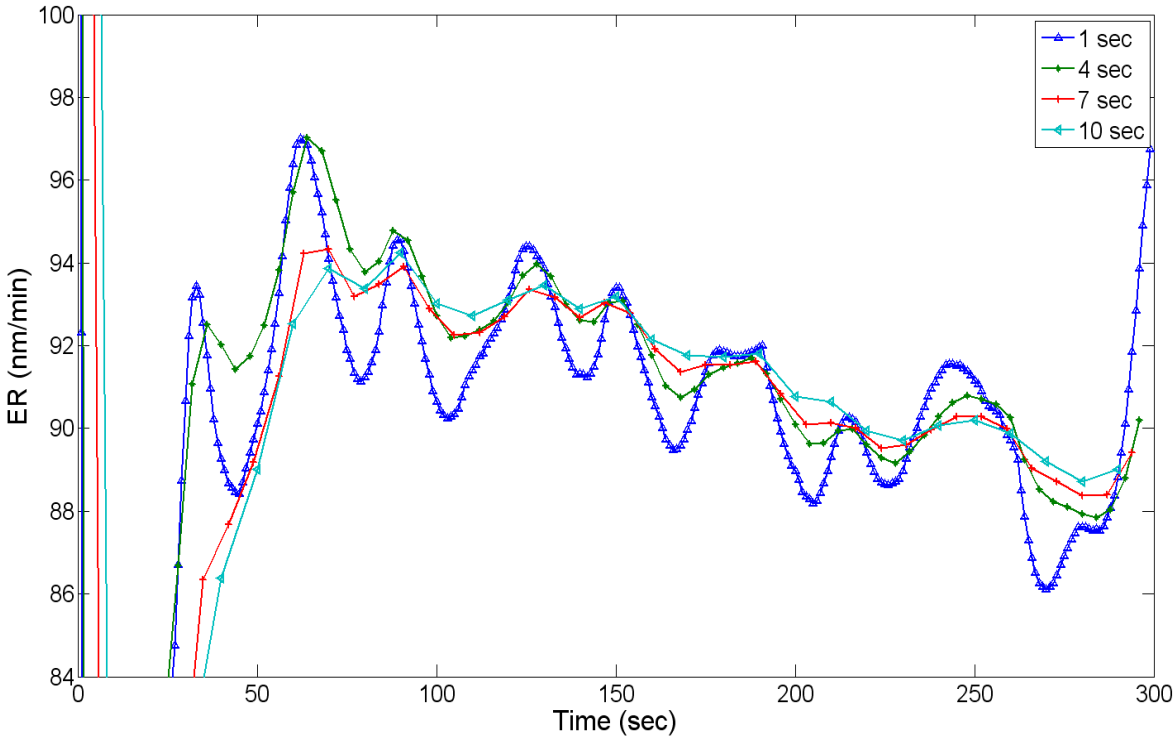

Figure 64 In-situ ER estimation by EKF with time for ZnO film (run 3), multiwavelength, $\Delta\lambda$ = 25nm

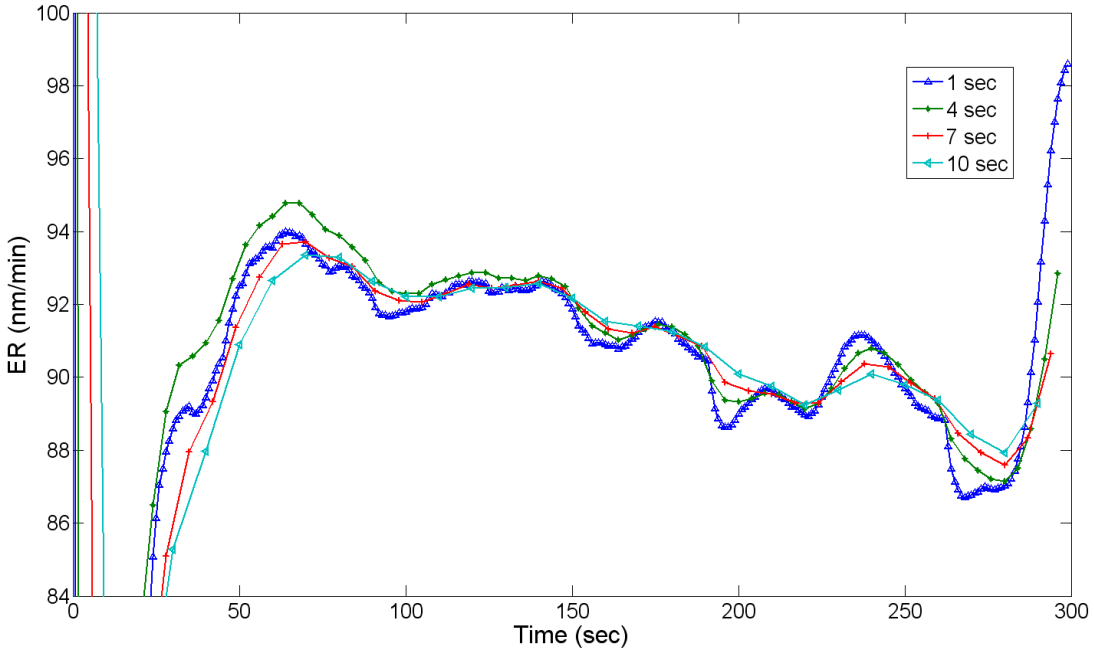

Figure 65 In-situ ER estimation by EKF with time for ZnO film (run 3), multiwavelength, $\Delta\lambda = 5nm$

Comparison of Figure 68 and Figure 69 indicates that the variation in ER prediction for LS/RLS can be decreased by using larger number of wavelengths in the simulation (with a corresponding increase in the computation time as shown in Table 15). This variation in ER arises from the variation in thickness, which in turn is due to the inability to incorporate a sufficient number of wavelengths to capture the reflectance spectra, thereby causing the algorithms to reach local minima. This variation in thickness is not visible in Figure 68 but becomes apparent as Figure 68 is enlarged. EKF/mMHE can eliminate this variation with a significantly lower number of wavelengths. It also shows that the variation in ER in Figure 68 for times<250 sec is an artifact introduced by the LS/RLS algorithms. The same conclusion is reached when simulations are carried out for run 1 and run 2; for brevity purposes, these figures/tables are not shown here.

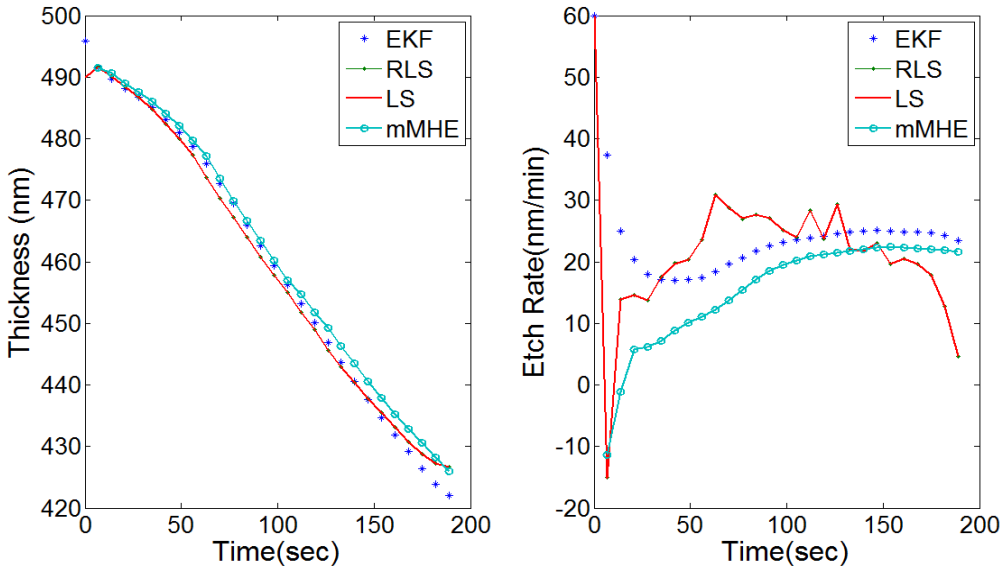

Figure 66 In-situ ER and thickness variation with time for ZnO film (run 1), multiwavelength, m=2, Δt =7 sec

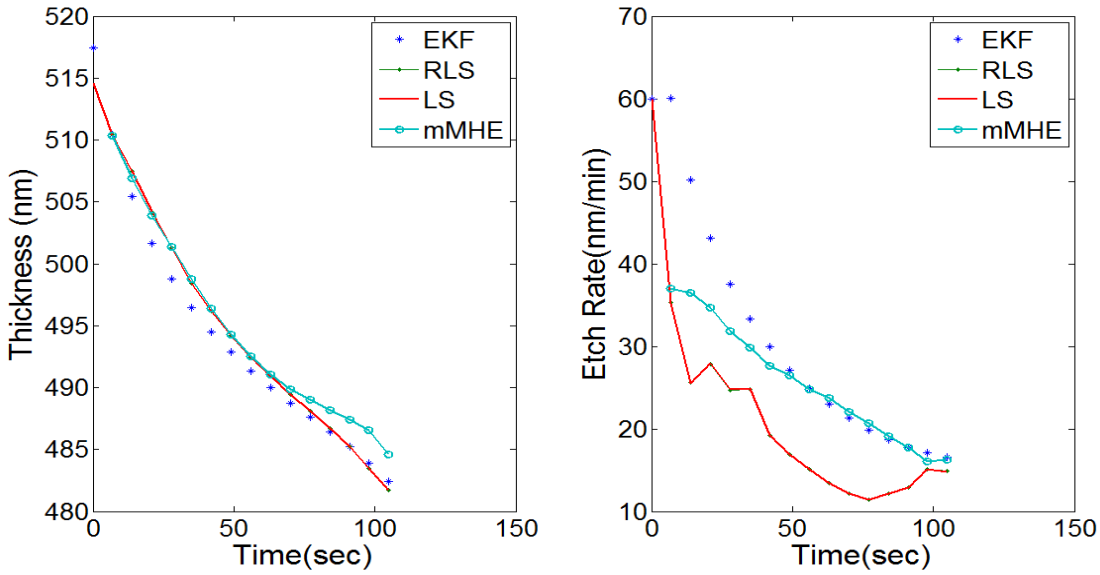

Figure 67 In-situ ER and thickness variation with time for ZnO film (run 2), multiwavelength, m=2, Δt =7 sec

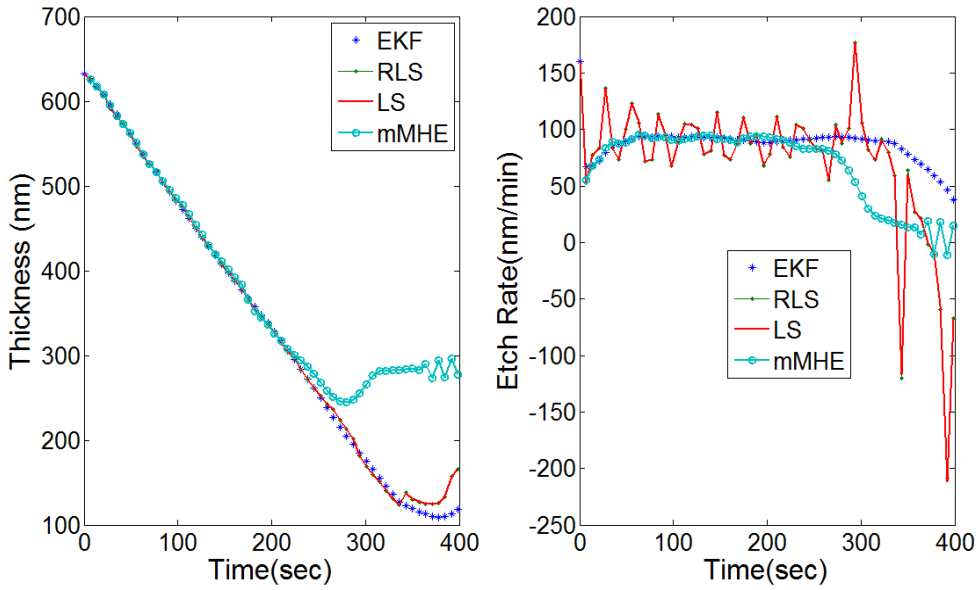

Figure 68 In-situ ER and thickness variation with time for ZnO film (run 3), multiwavelength (wavelengths in increment of 25 nm in the range 400-900 nm), m=2, Δt =7 sec

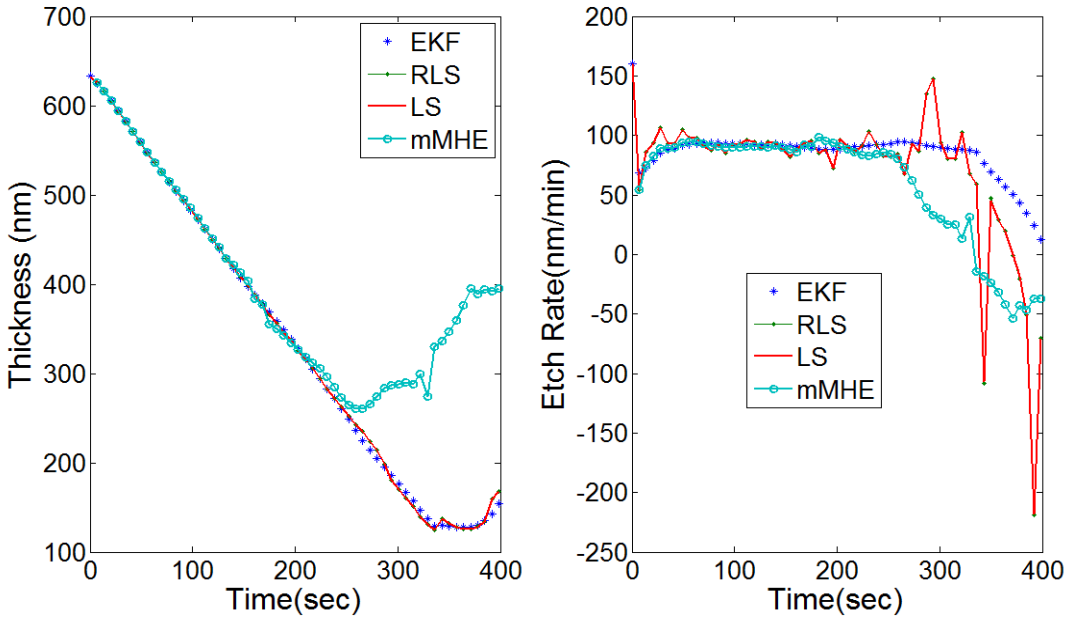

Figure 69 In-situ ER and thickness variation with time for ZnO film (run 3), multiwavelength (wavelengths in increment of 5 nm in the range 400-900 nm), m=2, Δt =7 sec

The thickness was assumed to decrease linearly starting at the initial thickness value as predicted by LS and ending at zero thickness for run 3. The difference between this value and the thicknesses predicted by LS at various wavelength spacing in the interval 400-900 nm is plotted in Figure 70. These results again indicate that as a larger number of wavelengths are used in the LS estimation, the oscillations in prediction decrease. A typical reflectance spectrum (such as Figure 45) has its extrema closely spaced at lower wavelengths indicating a finer wavelength spacing should be used in this region whereas a constant wavelength spacing has been used in this study. It should be noted that one does not have an independent measure for the estimation of 'true' ER in this study unless another independent technique is used in-situ. That is, the underlying assumption in this analysis is that the larger number of wavelengths used in the LS algorithm should lead to the true ER profile.

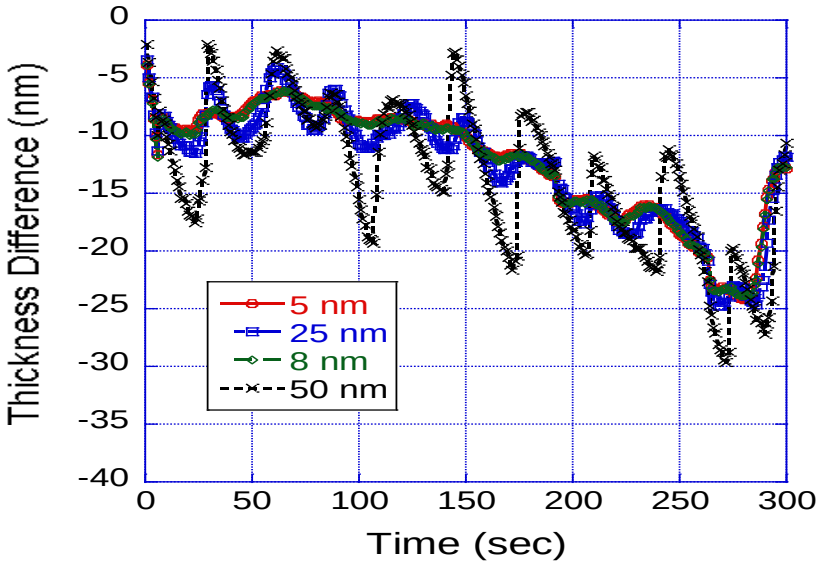

Figure 70 Difference in the thickness values predicted by LS for run 3 and an assumed straight line thickness decay starting at the initial thickness for time= 0 sec predicted by LS and ending at zero thickness. The different legends indicate the wavelength spacing used in the range 400-900 nm in the prediction of LS

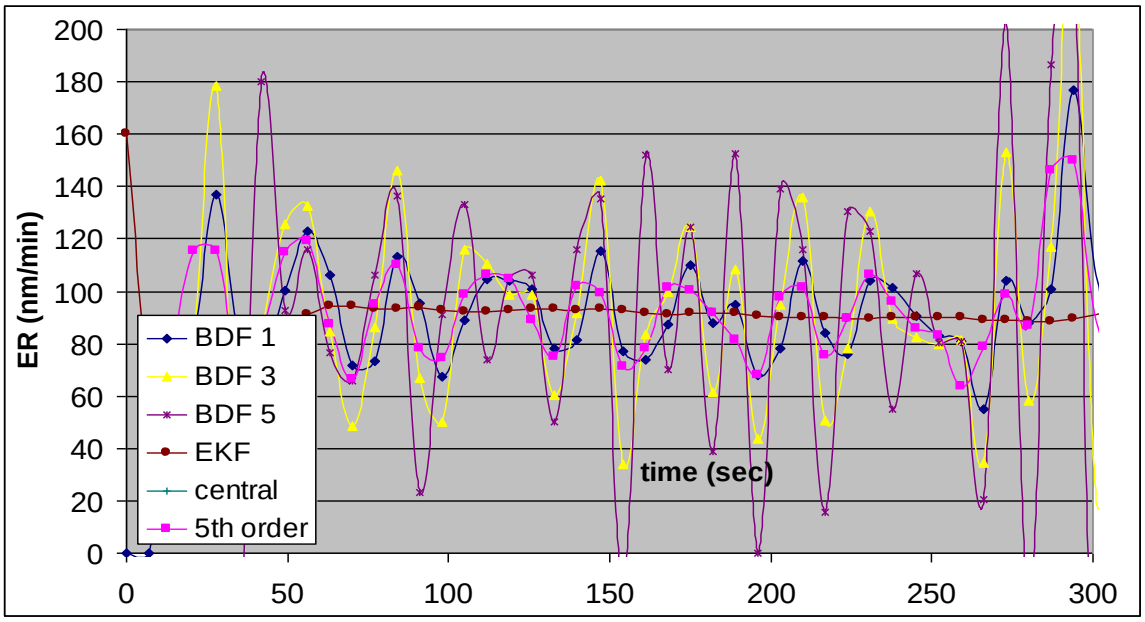

Figure 71 ER calculated for run 3 by various difference approximations and comparison with EKF, the thickness data is from LS in Figure 68

Figure 71 compares the ER calculated by various difference approximations (since it does not assume a process model) and their comparison with EKF. The ER prediction by LS depends on how one chooses to calculate it. The figure shows that the errors magnifies with higher order Backward Difference Formulae (BDF) and central order difference or a five point slope formula tend to smoothen out the oscillations in ER values. These formulae are given in the appendix. It also shows that difference formulae cannot

completely smoothen the ER oscillations due to the oscillations in thickness values in contrast with EKF.

Variations in ER observed at times >300 sec may be due to the inherent non-uniformity in the deposited film thickness. Specifically, a two inch wafer showed a variation of ~50 nm from one edge of the wafer to the other. The diameter of the incident probe is ~7 mm. The thickness non-uniformity over this area gives rise to various reflectance spectra which get superimposed, the sensor model uses this resultant spectra in its estimations which degrades the sensor model accuracy. In addition, there may be flow non-uniformity across the wafer surface. For run 3, the wafer was etched until the film was completely removed. For the probe area under the beam, part of the area is covered by the film while the remaining area had its film removed. Obviously, this situation leads to inaccuracies in etch end point prediction.

Table 16 compares the mean thickness and ER values at the end of run for five initial guesses for the different algorithms. RLS and LS prediction for all runs were compared and it was found that the two algorithm predictions are in good agreement at lower value of 'm'. At longer horizon size, RLS smoothens out the variations in LS predictions. Both thickness and ER predictions are different from each other for run 3 because of a lower thickness value, which is consistent with our earlier discussion regarding inherent problems in the optics system for lower thickness values. Also, EKF and mMHE predictions are closer to each other at this low horizon size since EKF algorithm is essentially a subset of mMHE at m=1.

Table 16 Mean of five runs for ER and thickness values at the end of each run, m=2, Δt =1 sec,

	State	EKF	RLS	mMHE	LS
Run 1	Thickness (nm)	464.3844	426.6762	461.2300	426.6798
	ER (nm/min)	3.8268	23.1405	11.4356	22.9141
Run 2	Thickness (nm)	469.5799	480.5210	461.7553	480.5249
	ER (nm/min)	25.8161	20.3547	34.6571	20.9655
Run 3	Thickness (nm)	198.83	165.48	192.19	165.2645
	ER (nm/min)	7.8	-50.31	-0.07105	-0.6262

It is noted that the ER measured is different than the one predicted by our CFD model. This may be due to inaccuracies in the estimation of heat effects (the standard state enthalpy and entropy of zinc formate has been estimated). Also, ZnO etching in formic acid proceeds by formation and widening of columnar pores at defect sites [92], and this fact has not been taken into account in the simulations.

It is clear from comparison with the dual wavelength approach that the use of multiwavelengths offers more robust estimation for both thickness and ER although this is achieved at the cost of increased computational time.

7.10 Conclusions

The reflectometric technique has been shown to be a suitable in-situ method for thickness and etch rate measurements in a wet etching environment. It offers a cost-effective alternative to more rigorous techniques, is easy to set up and troubleshoot. It can also be implemented at a non-normal angle of incidence, although with a difficult-to-achieve alignment. The sensor model has been developed from first principles and been implemented under both ex-situ and in-situ conditions.

The EKF, RLS and mMHE has been extended to the use of multiple wavelengths, thereby supplying improved optical spectra for ER prediction. The advantages over the dual wavelength approach using these state estimators have been described. The initial guess has been obtained using a more rigorous CFD model although a simple process model has been used in the state estimator. It has been shown that both EKF and mMHE are less oscillatory than RLS/LS in the prediction of thickness and ER and more robust when a smaller number of wavelengths are used, in addition, the computational time for EKF is less than that of mMHE/RLS. For no restrictions on computational requirements, LS should be the method of choice whereas in the case of faster etching systems, with the availability of a better process model, EKF should be starting point. The choice of algorithm is thus based on sampling rate for data collection, process model uncertainty and the number of wavelengths required.

CHAPTER 9

CONCLUSIONS

Achievement of adequate selectivity during the etching of different film materials when they are present in different areas on a device or in a stack is critical to the yield and reliability of devices in IC fabrication. Aqueous HF solutions have been the mainstay of silicon-based device process technology, but they possess very limited ability to achieve the selectivity levels needed for current and future ICs, MEMS and nanostructured devices. Tetrabutylammonium-based salts in an aqueous-organic solvent have therefore been investigated to allow more etch rate (ER) control and hence selectivity of BPSG ER / Thermal oxide ER (TOX). Water concentration plays an important role in establishing the ER. The specific organic solvent, THF and DMSO in this work, also plays a role although the importance is less than that of water content. Results have demonstrated that the solvent dielectric constant is not the only factor that establishes ER and that the differences in ER behavior of these two solvents can be explained in terms of relative basicity. NMR studies show that solvation of anions correlates with the observed oxide ERs. The use of organic fluoride-based salts in these mixed solvent systems allows etch selectivities of BPSG/TOX <1.9 to be achieved.

In order to precisely control film loss during cleaning or etching processes in IC and MEMS fabrication, a fundamental understanding of the overall integrated process is essential. Since etch chemistry and the various process parameters are interactive

components of an etch recipe or sequence, even an optimum chemistry can yield a suboptimal clean process. An integrated reactor for cleaning/wet-etching, rinsing, and drying was designed and fabricated based on computational fluid dynamics (CFD) simulations. These simulations also included the effects of reaction kinetics. The simulations established that HF concentration was the most influential parameter determining the variation of ER across the wafer followed by the HF flow rate. An experimental reactor system that was compatible with HF was assembled. Experiments conducted in this reactor showed that the reactor can be operated over a large range of process conditions and established the conditions under which uniform ERs can be achieved across the wafer for different films investigated. Simulation results agree with experimental ones within experimental error (~10%).

An optical reflectometric technique has been designed and fabricated to allow in-situ monitoring of ERs in a liquid (wet) etching environment. This system offers a cost-effective alternative to more rigorous techniques such as spectroscopic ellipsometry, is easy to set up and troubleshoot. This technique can also be implemented at a non-normal angle of incidence, although proper alignment can be difficult to achieve.

A sensor model has been developed from first principles and has been applied under both ex-situ and in-situ etch conditions. Various algorithms, including EKF and mMHE, have been implemented to facilitate data taking and control schemes for process monitoring. The dual wavelength approach to data collection has been extended to multiple wavelengths in order to supply improved optical spectra for ER prediction. The

advantages over dual wavelength approach using these state estimators have been described. The initial guess has been obtained using a more rigorous CFD model although a simple process model has been used in the state estimator. It has been shown that both EKF and mMHE are better state estimators than RLS when there is sensor model uncertainty due to incorporation of both process and sensor model; however, the computational time for EKF is less than that of mMHE. The choice of mMHE or EKF should be based on sampling rate of data collection, process model uncertainty and the number of wavelengths required.

CHAPTER 10

FUTURE WORK

9.1 Measurement of flow velocities in short contact time reactor using Laser Doppler Anemometry (LDA)

At higher Reynolds number (>2000), due to the transition into the turbulent regime, the flow distribution will be different from that described in Chapter 4 on reactor design. Although these flow dynamics can be simulated, the approach will involve solving k-ε equations under reactive flow conditions. One way to validate the model under such conditions is to measure velocities in the reactor at various points. LDA is a non-destructive technique for measuring the direction and speed of fluid motion. Polystyrene particles could be used as tracer particles. Since the HF chemistry compatible reactor is opaque to the light beam, the polycarbonate reactor could be used for these studies with water as a fluid. Light entrance paths for this reactor will have to be incorporated by drilling holes through the reactor head. As described previously, it can be assumed that the flow velocities in the HF chemistry compatible reactor and polycarbonate reactors will be identical under identical flow rates since most of the properties of interest for flow simulations (viscosity, density etc.) are essentially the same for water and dilute HF. (The heat of reaction is not sufficient to raise the fluid temperature substantially) ($>1^0$ C). The flow velocities measured can be compared with CFD simulations. After agreement is attained for the velocities, the reaction kinetics obtained from the experiments described above can be entered in the CFD simulations so that the distribution of chemical species

over the wafer surface can be calculated. The in-situ measured thicknesses by interferometry can then be correlated with this distribution.

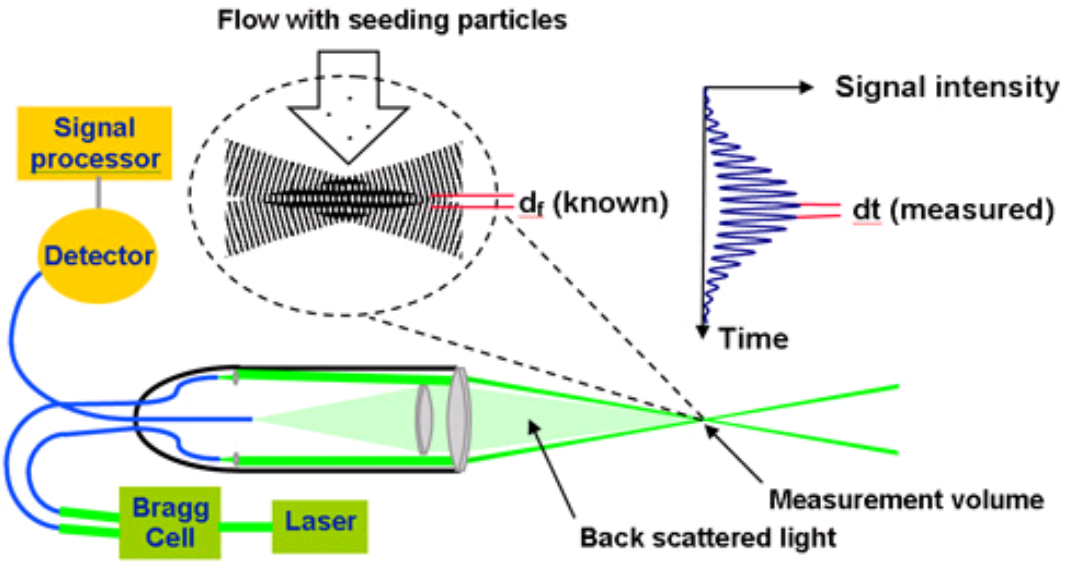

Figure 72 Schematics for LDA measurement[99]

9.2 Surface bonding structure using FTIR

A critical component of the etch process is the reaction/interaction of solution etchant species with the film surface. Attenuated total reflection FTIR (ATR-FTIR) has been used extensively to probe changes in chemical bonding structures that occur on a solid surface due to reactions between the solid and a gas or a liquid [100,101]. In order to identify the surface species formed in various solvent/salt mixtures, ATR-FTIR can be performed using a silicon internal reflection reactor system. An ATR-FTIR reactor has been built from PolyVinylideneFluoride (PVDF) to ensure compatibility with HF-based solutions, and can be used under flow and non-flow conditions. SiO_2 films can be grown or deposited on the Si waveguide. The specific solvent interactions with the Si surface can be used as a baseline for the FTIR measurements. This approach will mitigate mass

transfer limited effects when used under the flow conditions and will assist transfer of products away from the reaction site if etch products inhibit continued etching.

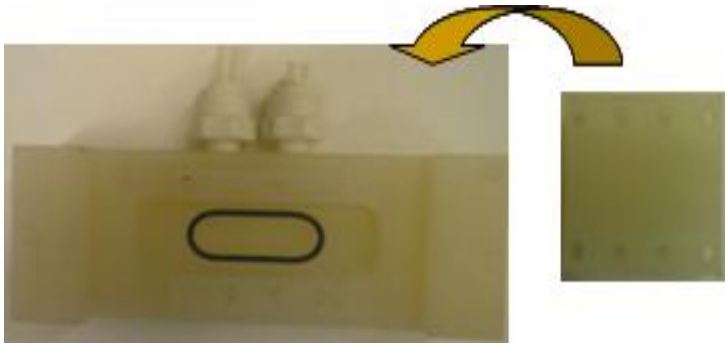

Figure 73 HF compatible cell for FTIR studies

9.3 2-D NMR techniques

2-D NMR techniques can yield more detailed information about the chemical environment of species in solution. For example, if a species is solvated, the diffusion coefficient is different from the pure species since the entire entity (solute and the solvation cloud) must transport as a unit. Diffusion Ordered SpectroscopY (DOSY) can be used to determine the difference in diffusion coefficients[102]. Diffusion measurements are carried out by observing the attenuation of the NMR signals during a pulsed field gradient experiment. The degree of attenuation is a function of the magnetic gradient pulse amplitude (G) and occurs at a rate proportional to the diffusion coefficient (D) of the molecule. Assuming that the signal at a given (fixed) chemical shift f belongs to a single sample component A with a diffusion constant D_A, then

$$S(f,z) = S_A \; f \; \exp \; -D_A Z \qquad (27)$$

where $S_A(f)$ is the spectral intensity of component A in zero gradient ('normal' spectrum

of A), D_A is the diffusion coefficient of A and Z encodes the different gradient amplitudes used in the experiment. Depending on the type of experiment, there are various formula for Z in terms of the amplitude G of the applied gradient and one or more timing parameters such as Δ (time between two pulse gradients, related to echo time) and δ (gradient pulse width). In the original Tanner-Stejskal method using two rectangular gradient pulses, for example,

$$Z = \gamma^2 G^2 \delta^2 \left(\Delta - \delta / 3 \right) \tag{28}$$

9.4 Simplification of CFD model

A CFD model takes into account the effect of all process parameters such as flow rate and concentration in addition to the effect of geometric parameters. The process model for in-situ implementation in this thesis is a constant ER model without taking these effects into account. In a manufacturing environment, the process model used should be between these two extremes. The simplification to a rigorous CFD model should lead to a non-dimensional 2D model in cylindrical co-ordinates as described in Leal[103],.

9.5 Cleaning effectiveness of various fluoride based solutions with N_2/IPA etching and drying

It is well-known that the presence of IPA is important for wafer drying due to the Marangoni effect [20,104-106]. The etch rate and cleanliness of wafer surfaces (as characterized by surface analyses such as XPS) dried in the reactor using different compositions of IPA in N_2 should be compared with those resulting from drying surfaces in a beaker. Since the Marangoni drying process has been modeled in detail, see for ex. [66-70], this model could be incorporated into the CFD simulations It is known that the

presence of IPA also decreases the etch rate of HF solutions.[104] Since the original short contact time reactor developed by Lam uses an IPA/N_2 blanket with the etch chemistry [39,64-66], the effect of addition of IPA to HF solutions can be studied to determine differences between the presence of IPA vapor and liquid phases during drying operations.

APPENDIX A: Zeta potential and streaming potential measurements

Since SiO_2 in contact with electrolyte solutions forms charged surface species, zeta potential and streaming potential measurements [107-109] were attempted. It was expected that correlation of these results with etch rate and species concentrations might generate insight into differences in surface interactions and thus etch behavior in various dilute F-based aqueous and organic salt solutions. However, a number of difficulties were encountered with these measurements.

1) Traditionally, zeta/streaming potential measurements are performed in <100mM solutions. The range of solution concentrations of interest for HF based solutions is 0.1 – 4 M. Unfortunately, current solution theory is not well developed for this range.
2) For 0.1 M solutions, the thickness of the electrical double layer is about 10 nm. For more concentrated solutions, this value will be even less.
3) Zeta potentials are traditionally measured for a colloidal system. The electrokinetic cell needed for the measurements in this work will require a custom design complete with the necessary connections and pumping system compatible with HF. Moreover, the colloidal particles have to be compatible with HF in order to decouple the reaction mechanism from adsorption of charges onto the particle surface.
4) For a system that measures zeta and streaming potentials and subsequently infers surface conductivity from these measurements, the channel width has to be very small (~ 50 μm). To build a system with variable width, a micrometer system compatible with fluoride-based species has to be designed. Alternately, channels fabricated from PDMS may be used, so that by applying techniques used in soft lithography, these channels can be constructed easily. However, PDMS absorbs moisture and the

channels collapse as observed in initial studies conducted in our laboratory using a 1:100 HF solution.

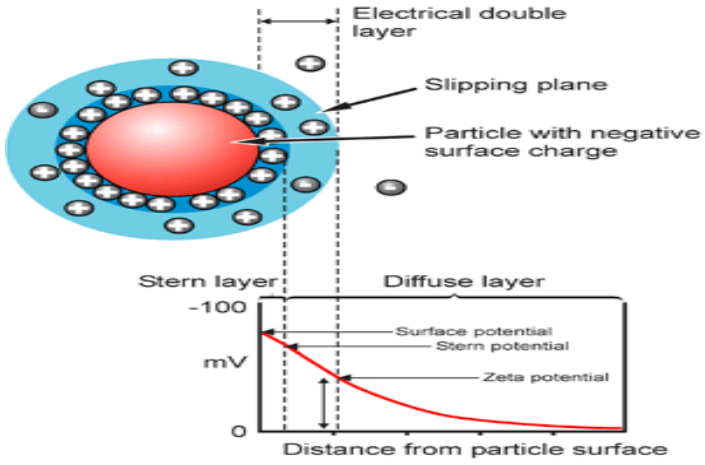

Figure 74 Electrical double layer around a particle[110]

APPENDIX B: Conductivity measurements

Measurement of solution ionic conductivity is a direct and convenient method to investigate ion behavior and solvation properties in electrolyte solutions. For fully dissociated electrolytes in dilute solutions, the theory is well developed and ion behavior can be predicted. Initial conductivity studies used equilibria (1) and (2) to characterize HF solutions up to 0.3 M [111]. However, the acidity of HF solutions increases dramatically with an increase in HF concentration. HF is a weak acid in very dilute solutions, but pure HF behaves as a super acid [29,112,113]. Even at relatively low HF concentrations, extent of dissociation increases significantly with HF concentration [29,112], apparently due to progressive solvation of F^- by molecular HF ($nHF+F^- \leftrightarrow (HF)_nF^-$).

Conductivity measurements have been used to characterize both anhydrous [114-116] and dilute HF solutions [13]. For HF solutions at extremely low concentrations (0.0001- 1 M HF) these measurements assisted the correlation of particular chemical species with SiO_2 etch rate; the authors classified the dissociation state of HF in these solutions into three regions as a function of initial HF concentration [11]. For use of HF solutions in the concentration range 0.1 - 4 M; equilibria involving $(HF)_nF^-$ must therefore be considered.

A conductivity cell has been fabricated as follows. Two platinum flag electrodes (5X5 mm) are spot welded to Pt wires that serve as the electrical leads for conductivity measurements. The Pt wires are inserted through a polypropylene rod to give mechanical strength. The electrode spacing is 0.7 cm; electrodes are sealed at the wetted end by 3M quick seal. This cell is calibrated to obtain the cell constant using KCl solution. If needed,

the platinum electrodes can be platinized to increase the surface area using hexachloroplatinic acid. An electrochemical impedence spectroscopy (EIS) system has been assembled for conductivity measurements. The conductivity cell is connected to a 4284 ECR Agilent meter and the results were analyzed using Labview. Basic background theory and results are given in the following text. The equivalent circuit of the conductivity cell can be represented as shown in Figure 75.

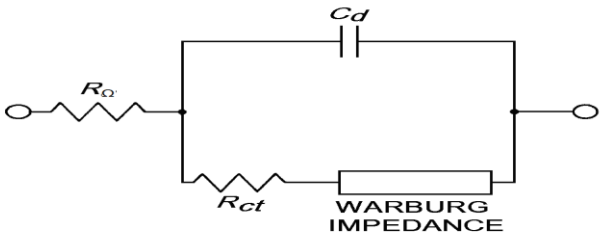

Figure 75 Equivalent circuit of a conductivity cell [117]

The Warburg impedence and R_{ct} in series can also be represented by an equivalent impedence Z_f or a series combination of resistance R_s and capacitance C_s.

The measured total impedence of this equivalent circuit, is expressed as a series combination of $Z_{Re} = R_B$ and $Z_{Im} = 1/(wC_B)$ and is given by [117]

$$Z_{\mathrm{Re}} = R_{\Omega} + \frac{R_s}{A^2 + B^2} \tag{29}$$

where

$$A = \frac{C_d}{C_s} + 1 \tag{30}$$

$$B = wR_sC_d \tag{31}$$

$$Z_{\text{Im}} = \frac{\frac{B^2}{wC_d} + \frac{A}{wC_s}}{A^2 + B^2} \tag{32}$$

However,

$$R_s = R_{ct} + \frac{\sigma}{\sqrt{w}} \tag{33}$$

$$C_s = \frac{1}{\sigma\sqrt{w}} \tag{34}$$

which gives,

$$Z_{\text{Re}} = R_{\Omega} + \frac{R_{ct} + \frac{\sigma}{\sqrt{w}}}{C_d\sigma\sqrt{w} + 1^{\ 2} + w^2 C_d{}^2 \left(R_{ct} + \frac{\sigma}{\sqrt{w}} \right)^2} \tag{35}$$

$$Z_{\text{Im}} = \frac{wC_d \left(R_{ct} + \frac{\sigma}{\sqrt{w}} \right)^2 + \frac{\sigma}{\sqrt{w}}\ \sqrt{w}C_d\sigma + 1}{C_d\sigma\sqrt{w} + 1^{\ 2} + w^2 C_d{}^2 \left(R_{ct} + \frac{\sigma}{\sqrt{w}} \right)^2} \tag{36}$$

Hence a plot of Z_{Re} vs. w will give the value of R_Ω at very high values of w. The plot of Z_{Im} vs. Z_{Re} at $Z_{Re} = 0$ gives the value of $R_\Omega + R_{ct}/2$. Hence using equations (35) and (36), C_d and σ can then be determined.

APPENDIX C: Procedure for operation of reactor

It should be noted that the reactor can be operated with some of the holes closed for flow (with tape) or when all holes are eligible for conducting flow

Normal operating procedure (all holes eligible for conducting flow)

1. Before the start of experiments
    1.1. Valves H4 and H5 are adjusted from previous runs so that there is no formation of air bubbles in the system and no splashing of liquid over the top head of the reactor.
    1.2. Open the reactor top head and start the vacuum pump. Make sure that there is no trapped liquid inside the drain line.
    1.3. Turn off the vacuum pump, put the wafer in place (by matching the marking on the wafer with the reactor inlet holes) and close the reactor lid.
    1.4. Start the vacuum pump.
2. Etching procedure
    2.1. Open valves H3 and H1. Adjust the flow rate of HF using the rotameter.
    2.2. Close valve H3 and open valve H2 slowly so that liquid can be clearly seen entering the reactor. The stop clock is started when the valve is opened fully. Steps 2.3 and 2.4 are to be followed during the etching time.
    2.3. Open valves W2 and W4. Adjust the flow rate of DIW using the rotameter.
    2.4. Close W4.
    2.5. W1 is to be manipulated only when there is air bubble formation in the water line. From initial runs it was observed that a similar valve is not needed in the HF line.

2.6. When the required time of reaction is reached, follow the rinsing procedure step 1 after closing H2 immediately.

3. Rinsing procedure

3.1. At the end of etching step, when valve H2 is closed, immediately open valve W3 so that the rinsing time is monitored properly.

3.2. Close H1.

3.3. When the rinsing time ends, start immediately the drying procedure after closing W3.

4. Drying procedure

4.1. Close valve W2. Open valves N1 and N2. This should clear liquid in most of the parts of the distributor.

4.2. Open valves W3 and H2. Make sure that W2 and H1 are closed.

4.3. Open valves W4 and H3. Let the trapped liquid inside the line go to the waste.

4.4. Close W3, H2, W4 and H3.

4.5. After drying for a specified amount of time, close N1 and N2.

5. After the experiment

5.1. Take the wafer out. Wipe away all liquid coating the reactor walls.

Issues with the reactor operation

1. There is some trapped liquid in the reactor after the end of the drying operation. It is assumed that this liquid is only DI water at the end of rinsing operation.
2. The drying time is not sufficient for the wafers. Wafers were taken out of the reactor and then dried. The drying time cannot be increased for more than few minutes since there can be water marks left on the wafer.

Other modes of operation

1. Performing experiments without use of the vacuum pump

   In this case, the flow through the drain is gravity driven. The reactor must be at an elevation such that there is sufficient head for the liquid to flow. Other procedures remains the same as described above.

2. Performing experiments with both HF and DIW in the same line (sequential flow of these solutions).

   The schematic for this case is shown in Figure 76. The procedure remains the same as that described previously.

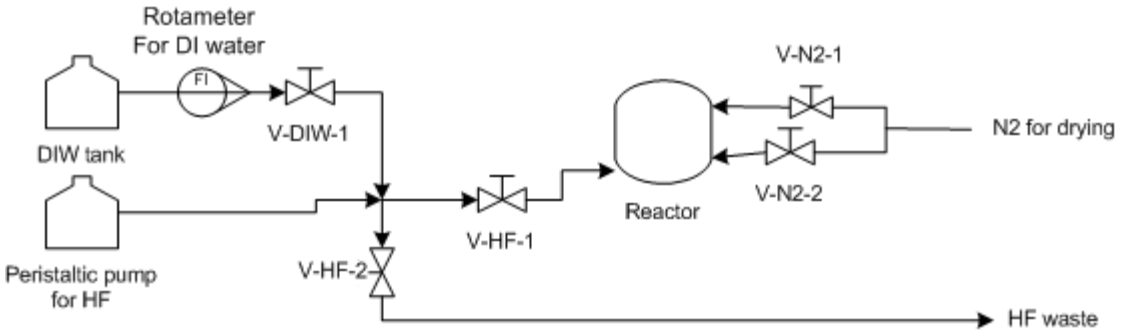

Figure 76 Running both HF and DIW in the same line (sequential flow)

APPENDIX D: Procedure for running the FLUENT® simulations

An extensive procedure for running the FLUENT® simulations for all the cases studied is described in the FLUENT® user's guide. A simplified description of this procedure is given here.

1. Open FLUENT® model in 3ddp format.
2. Click on (File→ open→ case and data) to open the simulation case and data files.
3. Click on (Grid→ check) to check the grid. There should not be a negative volume for any element.
4. Click on (define→ model→ solver) to select the appropriate solver setting. The default has been already chosen in this case.

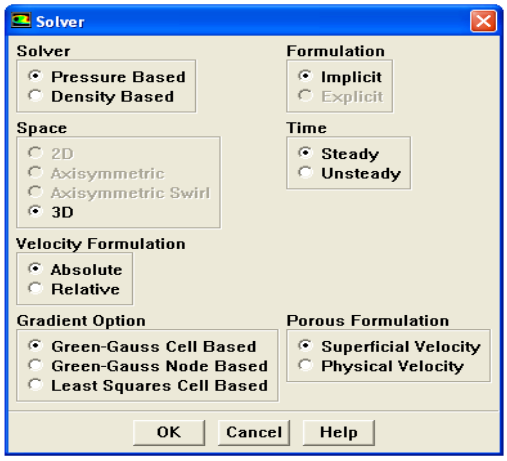

Figure 77 Solver configurations chosen

5. Click on (define→ model→ species→transport and reaction). The default options are already chosen.

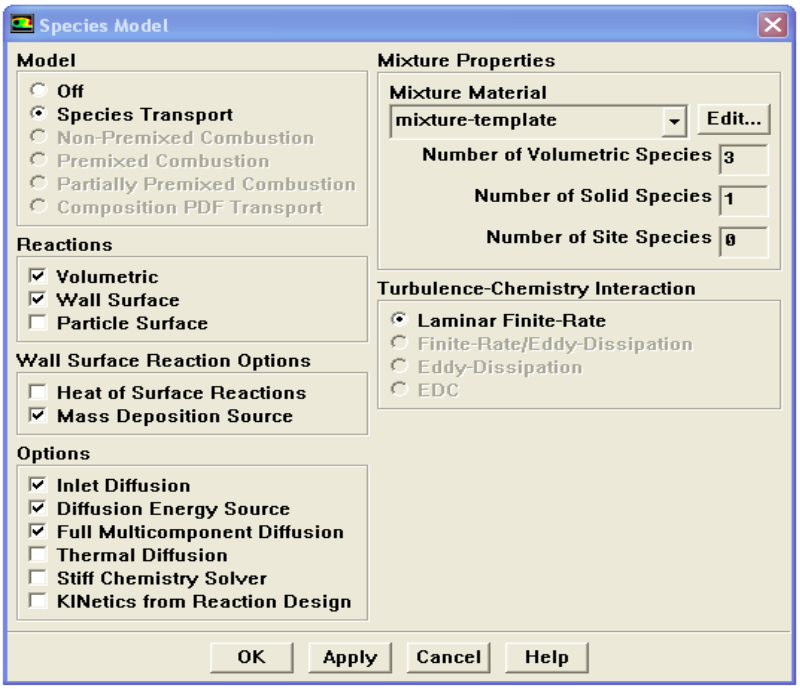

Figure 78 Species model configurations

6. Click on (define→ materials). The default options are already chosen for all the physical property values.
7. Click on (define→ materials→ mixture species) to check that appropriate species have been chosen. Default values are already set.
8. Click on (define→ materials→ reactions) to check that appropriate species have been chosen. Default values are already set.

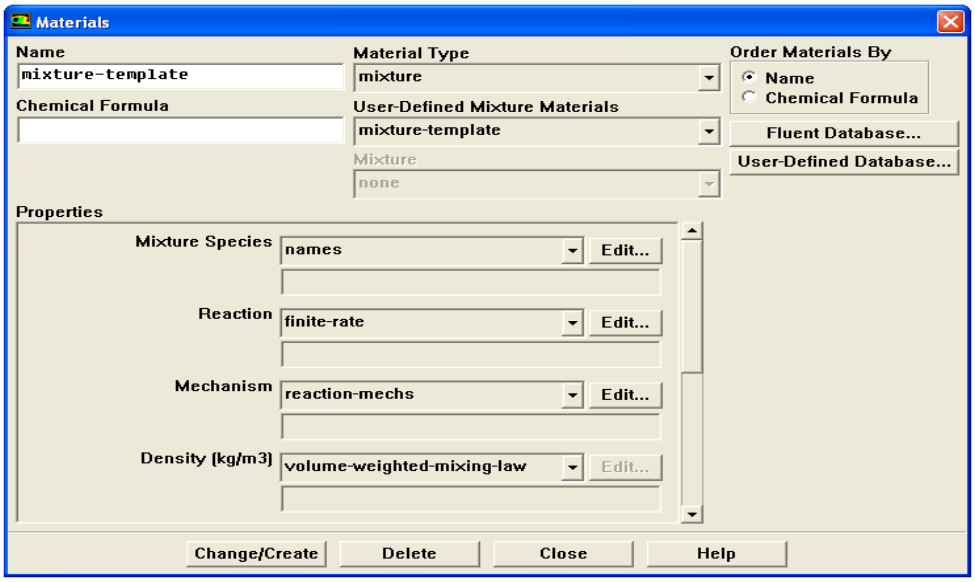

Figure 79 Materials panel

9. Click on (define→ operating conditions) to check that appropriate species have been chosen. Default values are already set.

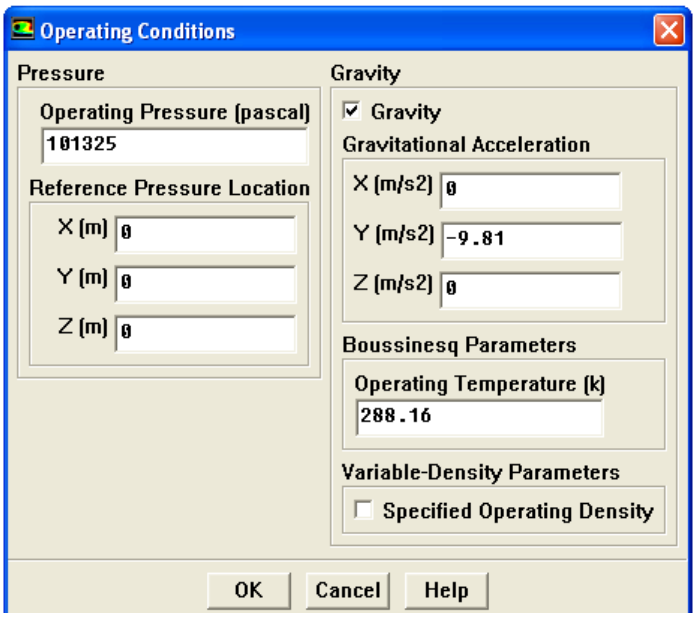

Figure 80 Operating conditions specifications panel

10. Click on (define→ Boundary conditions) to check that appropriate boundary conditions have been chosen. Default values are already set.

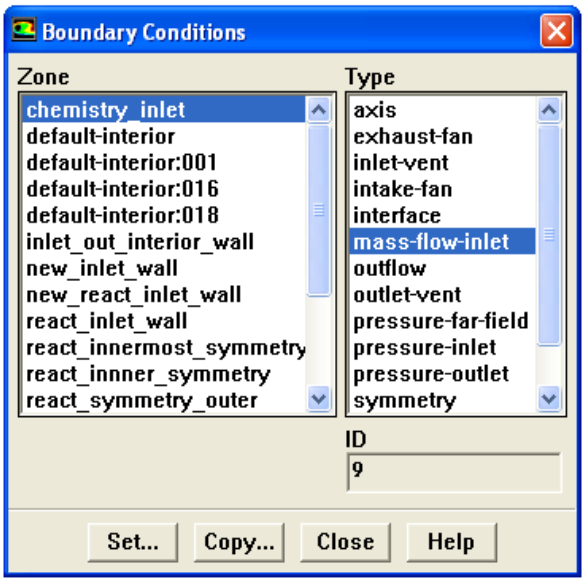

Figure 81 Boundary conditions specifications panel

11. Click on (solve→controls→ solution) to check that appropriate values have been chosen. Default values are already set.

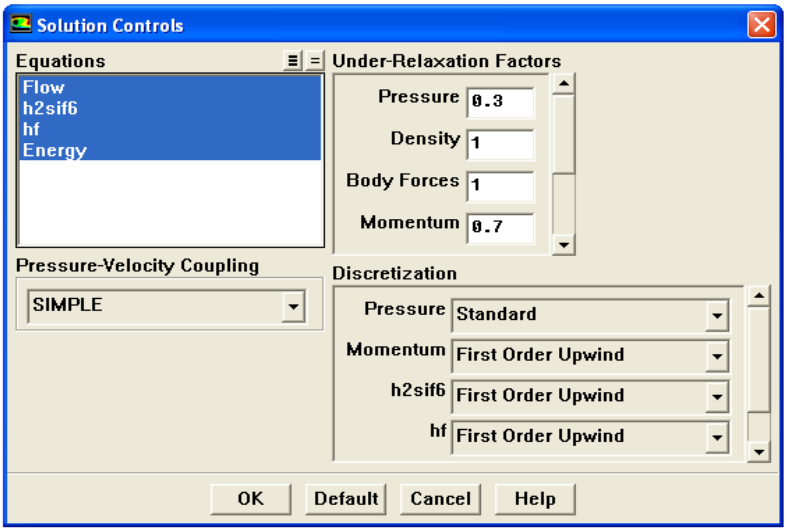

Figure 82 Solution controls specifications

12. Click on (solve→iterate→iterate) to solve the case. Since the solution is already converged one, it should again show converged residuals within one iteration.

APPENDIX E: Sensor model description

The theory of electromagnetic wave propagation in multilayered systems employs a matrix method instead of the method of summation because the latter method becomes cumbersome after a two layer system. The following optical model has been adapted from that described in literature [72] with most notations unchanged. Only the most important equations needed for MATLAB programming are presented here. The symbols used to describe the optical system invoked for this model (which will be shown schematically in Figure 83) are as follows.

1. Subscript +/- denotes the direction in which the wave travels with respect to the surface normal.
2. Subscript m denotes the m^{th} medium through which the wave travels.
3. Subscript s/p denotes the direction of polarization.
4. Subscript x/y denotes the x or y component.
5. E and H denote the electric and magnetic vectors, respectively.
6. n is the real part of complex refractive index

It should be noted that the same model has also been derived in a number of ways [72-74,80-82]. The widely used approach that is easy to program is presented here.

The formulae for s and p polarized reflectance ($r_{m,p}$ and $r_{m,s}$) and transmission ($t_{m,p}$ and $t_{m,s}$) coefficients are given as follows. For p polarization

$$t_{m,p} = \frac{2n_{m-1}\cos\varphi_{m-1}}{n_{m-1}\cos\varphi_m + n_m\cos\varphi_{m-1}} \tag{37}$$

$$r_{m,p} = \frac{n_{m-1}\cos\varphi_m - n_m\cos\varphi_{m-1}}{n_{m-1}\cos\varphi_m + n_m\cos\varphi_{m-1}} \tag{38}$$

and for s polarization

$$t_{m,s} = \frac{2n_{m-1}\cos\varphi_{m-1}}{n_{m-1}\cos\varphi_{m-1} + n_m\cos\varphi_m} \tag{39}$$

$$r_{m,s} = \frac{n_{m-1}\cos\varphi_{m-1} - n_m\cos\varphi_m}{n_{m-1}\cos\varphi_{m-1} + n_m\cos\varphi_m} \tag{40}$$

The forms of equations for the p and s components are identical so that the suffix p or s from the Fresnel coefficient may be dropped.

With

$$\delta_m = \chi_m d_m \tag{41}$$

$$\chi_m = \frac{2\pi n_m\cos\varphi_m}{\lambda} \tag{42}$$

The recurrence relation for the electric vectors E can be written as

$$\begin{pmatrix} E^+_{m-1} \\ E^-_{m-1} \end{pmatrix} = \frac{1}{t_m}\begin{pmatrix} e^{i\delta_{m-1}} & r_m e^{i\delta_{m-1}} \\ r_m e^{-i\delta_{m-1}} & e^{-i\delta_{m-1}} \end{pmatrix}\begin{pmatrix} E^+_m \\ E^-_m \end{pmatrix} \tag{43}$$

For a system of n layers, this becomes

$$\begin{pmatrix} E^+_0 \\ E^-_0 \end{pmatrix} = \frac{C_1 C_2 \ldots . C_{n+1}}{t_1 t_2 \ldots . t_{n+1}}\begin{pmatrix} E^+_{n+1} \\ E^-_{n-1} \end{pmatrix} \tag{44}$$

where

$$C_m = \begin{pmatrix} e^{i\delta_{m-1}} & r_m e^{i\delta_{m-1}} \\ r_m e^{-i\delta_{m-1}} & e^{-i\delta_{m-1}} \end{pmatrix} = \begin{pmatrix} a & b \\ c & d \end{pmatrix} \tag{45}$$

Since there is no negative-going wave in the $(n+1)^{th}$ medium, one can set $E_{n+1}^{-} = 0$.

The reflectance R and the transmittance T are given by

$$R = \frac{E^{-}_{o} \quad E^{-}_{o}{}^{*}}{E^{+}_{o} \quad E^{+}_{o}{}^{*}} = \frac{cc^{*}}{aa^{*}} \tag{46}$$

$$T = \frac{E^{+}_{n+1} \quad E^{+}_{n+1}{}^{*}}{E^{+}_{o} \quad E^{+}_{o}{}^{*}} = \frac{t_1 t_2 \ldots . t_{n+1} \quad t_1 t_2 \ldots . t_{n+1}{}^{*}}{aa^{*}} \tag{47}$$

where * denotes complex conjugate.

The ellipsometric parameters ψ and Δ are then given as

$$\tan\psi = \frac{\left|R^{p}\right|}{\left|R^{s}\right|} \text{ and } \frac{R^{p}}{R^{s}} = \tan\psi e^{j\Delta} \tag{48}$$

It should be noted that since a different nomenclature has been used among different literature sources for Δ, the Verdet convention was selected(see [81], pg 77) for the codes.

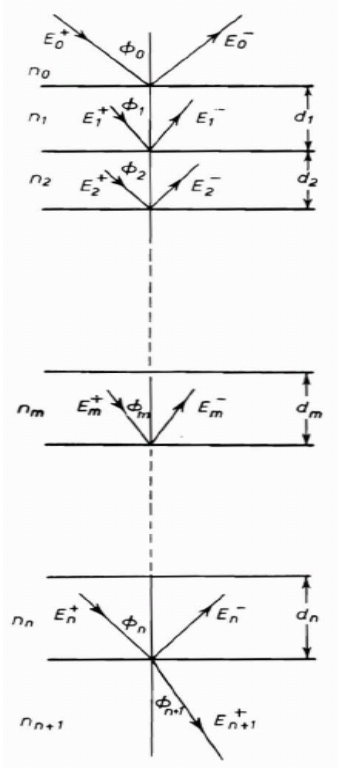

Figure 83 Schematic diagram used to find the multiple beam interference pattern, (from [72])

APPENDIX F: Sensor model Validation

The model implemented is described in brief in the Appendix and is the same as that used by commercial SE system providers; in the current study, it has been implemented in MATLAB. This model is capable of simulating a large number of different film configurations and characteristics, which include

1. Polarised interference patterns from films
2. Interference from any number of plane, parallel films of arbitrary thickness
3. Multiple angles of incidence
4. Dispersion relations for *n* and *k* (variation of *n* and *k* with wavelength)
5. Multiple wavelengths
6. Any ambient system (e.g., water or air)
7. Ellipsometric parameter ψ and Δ, polarized reflection and transmission coefficients for films
8. Prediction of thickness and/or *n* and *k* relationships for any number of films

However, there are some limitations of this model. Specifically,

1. The model is applicable only for isotropic films.
2. Large computational time is required for a large number of films layers.
3. There may be convergence problems when the *n* and *k* relationship is unknown.

This model has been validated for several reported studies on the SiO_2/Si system [73,80,81]. Figure 84 shows one example for the ψ and Δ trajectory for a film with n=1.46 (i.e., SiO_2)

and k=0 on a Si substrate at a wavelength of 6328 A and an angle of incidence of 70^0; this data is in agreement with the reported literature values. (The solid line is only a guide to eye, in that it simply connects the simulated data points).

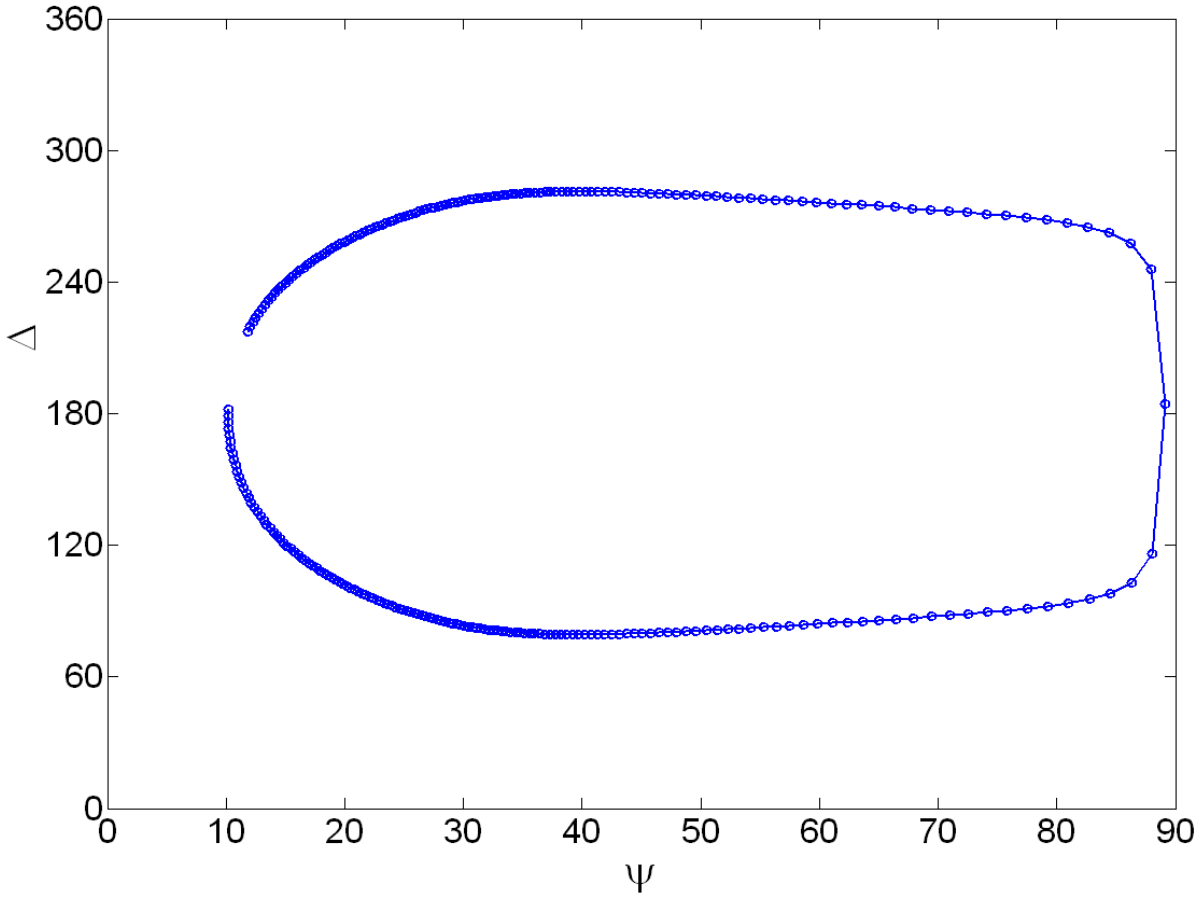

Figure 84 Simulated trajectories for a film with n=1.46 (i.e., SiO_2) on a Si substrate at a wavelength of 6328 A and an angle of incidence of 70^0)

The data reported in literature for Si, SiO_2 and water [75,118,119] were fitted to the following function to obtain a dispersion relation in a limited range of wavelengths from 400 nm-900 nm. This relationship is used for the ex-situ and in-situ implementation as given in sections 1.2 and 1.3.

$$n_{si} = 936.599 * \exp(-\lambda / 64.63) + 3.7737 \quad (49)$$

$$k_{si} = 1.5428 * 10^{-12} * \exp(-\lambda / 13.50164) + 0.04021 \quad (50)$$

$$n_{SiO_2} = \sqrt{1.3 + \frac{0.81996 \cdot \lambda^2}{\lambda^2 - 0.010808} - 0.01082 \cdot \lambda^2} \quad (\lambda \text{ in } \mu m) \quad (51)$$

$$k_{SiO_2} = 0 \quad (52)$$

Also, in the results and discussion, a normal incidence and multiple wavelengths are used.

APPENDIX G: ZnO optical constants

A ZnO sample film was fitted using point-by-point fit in M-2000 Woollam ellipsometer. The refractive index value was then curve fitted using various model including Cauchy. Figure 85 shows the comparison.

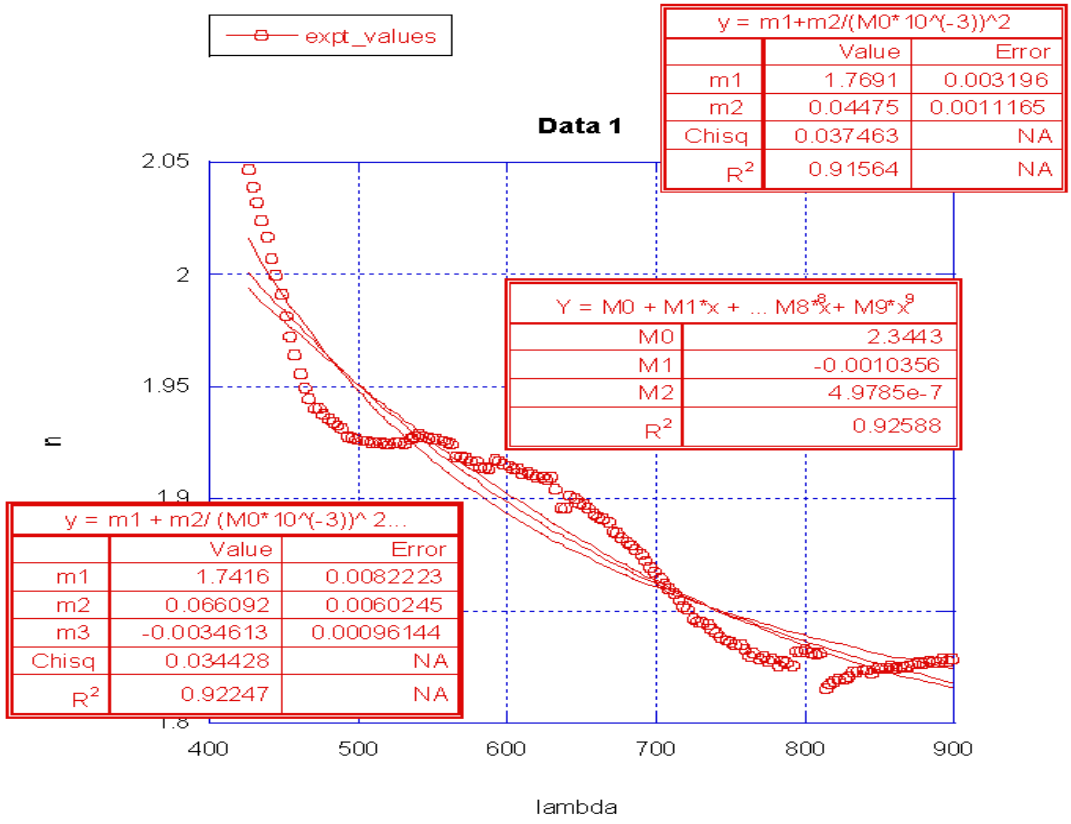

Figure 85 Comparison of various optical constant models for a ZnO sample film

It is noted that the fit using second order polynomial value is marginally better than using a three parameter Cauchy model. However, there are other samples for which the Cauchy fit is better (in the MSE value as fitted using ellipsometer) than using a polynomial

optical-constant model. Hence a standard Cauchy model was chosen. It is also noted that the value of constant ‘A’ in Cauchy model can vary for ZnO film from 1.8 to 1.92.

APPENDIX H: Details of the algorithms

The analytical expressions for LS, RLS, EKF and mMHE are well-documented [22,85]. Therefore, only a brief overview of each of these methods is presented. The MATLAB® code kindly provided by [85] has been adapted for this study..

Extended Kalman Filter (EKF)

For a nonlinear system, $x_{k+1} = f\ \ x_k\ \ + w_k$, and $y_k = g\ \ x_k\ \ + v_k$ and the Extended Kalman Filter (EKF) equations are

$$P_{k|k-1} = \left(\left. \frac{\partial f}{\partial x} \right|_{\hat{x}_{k-1}} \right) P_{k-1|k-1} \left(\left. \frac{\partial f}{\partial x} \right|_{\hat{x}_{k-1}} \right)^T + Q \tag{53}$$

$$\hat{x}_{k|k-1} = f\ \ \hat{x}_{k-1} \tag{54}$$

$$G_k = P_{k|k-1} \left(\left. \frac{\partial g}{\partial x} \right|_{\hat{x}_{k|k-1}} \right)^T \left[\left(\left. \frac{\partial g}{\partial x} \right|_{\hat{x}_{k|k-1}} \right) P_{k|k-1} \left(\left. \frac{\partial g}{\partial x} \right|_{\hat{x}_{k|k-1}} \right)^T + R \right]^{-1} \tag{55}$$

$$P_{k|k} = \left[I - G_k \left(\left. \frac{\partial g}{\partial x} \right|_{\hat{x}_{k|k-1}} \right) \right] P_{k|k-1} \tag{56}$$

$$\hat{x}_{k|k} = \hat{x}_{k|k-1} + G_k \left[y_k - g\ \ \hat{x}_{k|k-1}\ \ \right] \tag{57}$$

where Q and R are the covariance matrix of *w* and *v*, respectively. G_k is the Kalman gain at time *k*. $P_{k|k-1}$ and $P_{k|k}$ are the a-priori and a-posteriori error covariance matrices, respectively. *x* and *y* are the state and output variables respectively and x_k is the state at time-step *k.*

In the case of reflectance data, y is the measured relative reflectance, function f is the simple process model, function g is the sensor model described in the appendix on sensor

model and x is a vector of two elements, thickness and ER. It is noted that both in the simulation as well as experimental study, no process/sensor noise was added in this work.

Recursive Least Squares (RLS)

Given a sequence of reflectance measurements in a window from k-m+1 to k, the optimum solution of x_k, x_k^{opt} can be obtained by solving the following optimization problem

$$x_k^{opt} = \min_{x_{k-m+1}} \sum_{l=k-m+1}^{k} v_l^T v_l \tag{58}$$

where $v_l = y_l - g(x_l)$ the error between the sensor model prediction and the reflectance measurement at time l; as a result, the optimal solution can change depending upon the window size. In this study, a window size for RLS the same as that for mMHE was used. It also noted that there is no tuning matrix R for the case of RLS in this work.

Modified Moving Horizon Estimator (mMHE)

Mathematically, given a sequence of measurements in a horizon starting from k-m+1 to k, the initial state in this horizon x_{k-m+1} can be estimated by solving the following minimization problem

$$x^e{}_{k-m+1}{}^T P^{-1}{}_{k-m+1|k-m} x^e{}_{k-m+1} + \sum_{l=k-m+1}^{k} v^T{}_l R^{-1} v_l \tag{59}$$

$$x^e{}_{k-m+1} = x_{k-m+1} - x_{k-m+1|k-m} \tag{60}$$

$$v_l = y_l - g \quad f^{\,l-\ k-m+1} \quad x_{k-m+1} \tag{61}$$

The measurement-correction terms in EKF are

$$L_{k-m+1} = P_{k-m+1|k-m} C_{k-m+1|k}{}^{T} \quad C_{k-m+1|k} P_{k-m+1|k-m} C_{k-m+1|k}{}^{T} + R \quad ^{-1} \tag{62}$$

$$x_{k-m+1|k-m+1} = x_{k-m+1|k-m} + L_{k-m+1} \quad y_{k-m+1} - g \quad x_{k-m+1|k} \quad - C_{k-m+1|k} \quad x_{k-m+1|k-m} - x_{k-m+1|k} \tag{63}$$

$$P_{k-m+1|k-m+1} = \quad I - L_{k-m+1} C_{k-m+1|k} \quad P_{k-m+1|k-m} \tag{64}$$

The measurement-prediction terms in EKF are

$$x_{k-m+2|k-m+1} = f \quad x_{k-m+1|k} \quad + A_{k-m+1|k} \quad x_{k-m+1|k-m+1} - x_{k-m+1|k} \tag{65}$$

$$P_{k-m+2|k-m+1} = A_{k-m+1|k} P_{k-m+1|k-m+1} A^{T}{}_{k-m+1|k} + Q \tag{66}$$

$$C_{k-m+1|k} = \left. \frac{\partial g \quad x}{\partial x} \right|_{x = x_{k-m+1|k}} \tag{67}$$

$$A_{k-m+1|k} = \left. \frac{\partial f \quad x}{\partial x} \right|_{x = x_{k-m+1|k}} \tag{68}$$

where $f^{\,l-\ k-m+1} \quad x_{k-m+1}$ means that the process model f is applied to x_{k-m+1} for $l - (k - m + 1)$ times to calculate the state at time l.

Least square (LS)

For least squares, the MATLAB function ‘lsqcurvefit’ was used for thickness determination at each time step (ie. unlike the previous methods, only the current measurement at time k is used to estimate the thickness at time k). The ER was calculated from the difference in thickness values ie. the ER is calculated as follows.

, $$ER_t = \frac{h_t - h_{t-1}}{\Delta t} \tag{69}$$

Where h_t is the current thickness value and h_{t-1} is the previous thickness value.

In all simulation results, the first value for ER is the same as initial guess used for other algorithms.

APPENDIX I: Difference formulae

The formulae has the form [120]

, $$hy'_n = \sum_{j=0}^{k} \alpha_{kj} y_{n-j} \tag{70}$$

where the coefficients $\{\alpha_{kj}\}$ are

BDF Coefficients							
Order k	α_{k0}	α_{k1}	α_{k2}	α_{k3}	α_{k4}	α_{k5}	α_{k6}
1	1	-1					
2	3/2	-2	1/2				
3	11/6	-3	3/2	-1/3			
4	25/12	-4	3	-4/3	¼		
5	137/60	-5	5	-10/3	5/4	-1/5	
6	49/20	-6	15/2	-20/3	15/4	-6/5	1/6

For central difference [121]

, $$y' = \frac{y(x+h) - y(x-h)}{2h} \tag{71}$$

For a five point slope formala

, $$f'(x) = \frac{-f(x+2h) + 8f(x+h) - 8f(x-h) + f(x-2h)}{12h} \tag{72}$$

APPENDIX J: Problems in in-situ ellipsometry implementation

For an estimate of reaction rate, standard and more accurate techniques like ellipsometry cannot be used in our case because of many problems. If gap height can be increased, the following issues can be somewhat addressed although not completely.

1. Non-normal incidence of the light beam through the optical window. This changes the polarisation state of light at the interface between window and the fluid. Taking this into account is quite complicated.

2. Window material: Fused silica may frost because of HF based materials. Sapphire is resistant but it is birefringent. It will make issue of 1) even more complicated.

3. There might be bubble in the reactor walls if the widow is kept at normal incidence to the light beam.

4. To avoid bubble, there has to be an exhaust, drilled upto the reactor volume. However, to make the reactor operation bubble free, vacuum has been used for the drain. This will hamper the reactor operation.

5. Light beam intensity- A smaller size beam spot can be used to decrease the stringent requirement on the window size. The ellipsometer at GaTech gives a beam size of about 4 mm (circular) near 70 degrees angle of incidence. This size increases (because it is elliptical) when the beam is incident on the sample ie. a lot of intensity has to be thrown away. It can be somewhat tolerated by increasing revolution/sec of the polariser.

6. The widow will have to be fused instead of separate windows for light entrance and exit. There are difficulties in the fabrication of such a window, apart from its cost.

APPENDIX K: Raw compensation formulae

The compensation formulae in the reflection mode are as follows

, $$\%R = \frac{S_\lambda - D_\lambda}{R_\lambda - D_\lambda} \quad (73)$$

Where

S_λ sample intensity and wavelength λ

D_λ Dark intensity and wavelength λ

R_λ Reference intensity and wavelength λ

APPENDIX L: Matlab file for sensor model

```
clear all;clc;

lambda=400:900;

n_a(1)     = 0.81996;
n_b(1)     = 0.10396;
n_c(1)     = 0.01082;
offset_sio2     = 1.3;

%k_a(1)     =  -0.009611;
%k_b(1)     = 0.007182;
%k_c(1)     = 0.000999;

pre_exponent_si_k = 1.5428*10^(-12); %pre_exponent for k for si=
exponent_si_k = 13.50164;
offset_si_k =   0.04021;

pre_exponent_si_n = 936.599; %pre_exponent for k for si=
exponent_si_n = 64.63;
offset_si_n =  3.7737;

number_of_layers = 2; %% last layer is the substrate, o th is ambient,
1 is sio2 and 2 is silicon here
sio2 = 1; % put the number of sio(=1)2 here,
si =2; % put the number of si(=2) layer here
ambient = 2;% ;air =1 , water = 2;
%incidence_angle_increment = 0.1;
%incidence_angle_range = 10;

refrac_index = ones(number_of_layers,length(lambda));
k = ones(number_of_layers,length(lambda));

if (ambient==1)
    n0       = ones(1,length(lambda));%
    k0       = 0;
elseif (ambient==2)
    n0       = 1.33;
    k0       = 0;
end

complex_n0 = n0 + i*k0;

%k(sio2:)  = k_a(1) + k_b(1)./(lambda * 10^(-3)).^2 +k_c(1)./(lambda *
10^(-3)).^4;
k(sio2,:)  = 0;
refrac_index(sio2,:)  = sqrt(offset_sio2 + n_a(1)*(lambda * 10^(-
3)).^2./((lambda * 10^(-3)).^2 - n_b(1)^2) - n_c(1)*(lambda * 10^(-
3)).^2);

refrac_index(si,:) = pre_exponent_si_n * exp(-lambda/exponent_si_n) +
offset_si_n;%n_si_cal;%
%k(si,:) = 0;
```

```
k(si,:) = pre_exponent_si_k * exp(-lambda/exponent_si_k) +
offset_si_k;%k_si_cal;%

%for j=2:number_of_layers %% for more than/other than sio2/si system
define
%the values here
%    refrac_index(j,:) =
%   k(j,:) =
%end

angle_layer = zeros(number_of_layers-1,length(lambda));% angle of
incidence in degrees
thickness_range = 1;%271;% change this value for using multiple
thicknesses
angle_range =1;
for L=1:1:1%thickness_range
    for M=1:1:1%angle_range
        total_matrix_p = eye(2,2);
        total_matrix_s = eye(2,2);
        total_fresnel_transmission_coe_p = 1;
        total_fresnel_transmission_coe_s = 1;

        angle_zero = 0;%(M-1);%M*75;% angle of incidence for 1st
interface in degrees. measured from the vertical
                           %The rest will be calculated from snell's
law, check that the angle is not complex.
        thickness(1) = 970;  % in nm
        %%%%%%%%%%defining the values for first layer, based on air as
zeroth
            complex_refrac_index(1,:) = refrac_index(1,:) + i*k(1,:);
            %%%%%%%%%%%%%%%%%%%%%%%%%%%%very important
            angle_layer(1,:) =
asind(real(complex_n0.*sind(angle_zero)./complex_refrac_index(1,:)));
%% snell's law, angle in degrees check this step,
            %%%%%%%%%%%%%%%%%%%%%%%%%%%%very important

            % for p polarization;
            den_p(1,:) = complex_n0.*cosd(angle_layer(1,:)) +
complex_refrac_index(1,:).*cosd(angle_zero);
            r_p(1,:)    = (complex_n0.*cosd(angle_layer(1,:)) -
complex_refrac_index(1,:).*cosd(angle_zero))./den_p(1,:);
            t_p(1,:)    = 2*complex_n0*cosd(angle_zero)./den_p(1,:);
            % for s polarization;
            den_s(1,:) = complex_n0.*cosd(angle_zero) +
complex_refrac_index(1,:).*cosd(angle_layer(1,:));
            r_s(1,:)    = (complex_n0.*cosd(angle_zero) -
complex_refrac_index(1,:).*cosd(angle_layer(1,:)))./den_s(1,:);
            t_s(1,:)    = 2*complex_n0*cosd(angle_zero)./den_s(1,:);

            alpha(1,:)=
2*3.14*k(1,:).*thickness(1).*cosd(angle_layer(1,:))./lambda;
            gamma(1,:)=
2*3.14*refrac_index(1,:).*thickness(1).*cosd(angle_layer(1,:))./lambda;
            exp_delta_complex(1,:) =
exp(alpha(1,:)).*exp(i*gamma(1,:));
```

```
            % for p polarization;
            a_p(1,:)    = ones(1,length(lambda));
%exp_delta_complex(j-1,:) =1 for j=1;
            b_p(1,:)    = r_p(1,:)*1;
%exp_delta_complex(j-1,:) =1 for j=1;
            c_p(1,:)    = r_p(1,:).*1./1;
%exp_delta_complex(j-1,:) =1 for j=1;
            d_p(1,:)    = ones(1,length(lambda));
%exp_delta_complex(j-1,:) =1 for j=1;
            total_fresnel_transmission_coe_p =
total_fresnel_transmission_coe_p.*t_p(1,:);
            % for s polarization;
            a_s(1,:)    = ones(1,length(lambda));
%exp_delta_complex(j-1,:) =1 for j=1;
            b_s(1,:)    = r_s(1,:)*1;
%exp_delta_complex(j-1,:) =1 for j=1;
            c_s(1,:)    = r_s(1,:).*1./1;
%exp_delta_complex(j-1,:) =1 for j=1;
            d_s(1,:)    = ones(1,length(lambda));
%exp_delta_complex(j-1,:) =1 for j=1;
            total_fresnel_transmission_coe_p =
total_fresnel_transmission_coe_s.*t_s(1,:);

        %%%%%%%%%Values definition for air over

            for j=2:number_of_layers
                complex_refrac_index(j,:) = refrac_index(j,:) +
i*k(j,:);

                %%%%%%%%%%%%%%%%%%%%%%%%%%%%very important
                angle_layer(j,:) = asind(real(complex_refrac_index(j-
1,:).*sind(angle_layer(j-1))./complex_refrac_index(j,:))); %% snell's
law, angle in degrees
                %%%%%%%%%%%%%%%%%%%%%%%%%%%%very important

                %plot(lambda,angle_layer(j,:),'-b');
                % for p polarization;
                den_p(j,:) = complex_refrac_index(j-
1,:).*cosd(angle_layer(j,:)) +
complex_refrac_index(j,:).*cosd(angle_layer(j-1));
                r_p(j,:)    = (complex_refrac_index(j-
1,:).*cosd(angle_layer(j,:)) -
complex_refrac_index(j,:).*cosd(angle_layer(j-1)))./den_p(j,:);
                %figure;plot(lambda,r_p(j,:),'-b');
                t_p(j,:)    = 2*(complex_refrac_index(j-
1,:).*cosd(angle_layer(j-1)))./den_p(j,:);
                % for s polarization;
                den_s(j,:) = complex_refrac_index(j-
1,:).*cosd(angle_layer(j-1)) +
complex_refrac_index(j,:).*cosd(angle_layer(j,:));
                r_s(j,:)    = (complex_refrac_index(j-
1,:).*cosd(angle_layer(j-1)) -
(complex_refrac_index(j,:).*cosd(angle_layer(j)))))./den_s(j,:);
                %figure;plot(lambda, r_s(j,:),'-ro');
                t_s(j,:)    = 2*(complex_refrac_index(j-
1,:)*cosd(angle_layer(j-1)))./den_s(j,:);
```

```
            end

        if number_of_layers >2
            for j = 2:number_of_layers - 1
                    alpha(j,:)=
2*3.14*k(j,:).*thickness(j).*cosd(angle_layer(j,:))./lambda;
                    gamma(j,:)=
2*3.14*refrac_index(j,:).*thickness(j).*cosd(angle_layer(j,:))./lambda;
                    exp_delta_complex(j,:) =
exp(alpha(j,:)).*exp(i*gamma(j,:));
            end
        end

        for j = 2:number_of_layers
                %for p polarization
                a_p(j,:)    = exp_delta_complex(j-1,:);
                b_p(j,:)    = r_p(j,:).*exp_delta_complex(j-1,:);
                c_p(j,:)    = r_p(j,:).*1./exp_delta_complex(j-1,:);
                d_p(j,:)    = 1./exp_delta_complex(j-1,:);
                total_fresnel_transmission_coe_p =
total_fresnel_transmission_coe_p.*t_p(j,:);
                %for s polarization
                a_s(j,:)    = exp_delta_complex(j-1,:);
                b_s(j,:)    = r_s(j,:).*exp_delta_complex(j-1,:);
                c_s(j,:)    = r_s(j,:).*1./exp_delta_complex(j-1,:);
                d_s(j,:)    = 1./exp_delta_complex(j-1,:);
                total_fresnel_transmission_coe_s =
total_fresnel_transmission_coe_s.*t_s(j,:);
        end

        for n=1:length(lambda)
            for j=1:number_of_layers
                %for p polarization
                form_matrix_p = [a_p(j,n) b_p(j,n);c_p(j,n) d_p(j,n)];
                total_matrix_p = total_matrix_p*form_matrix_p;
                %for s polarization
                form_matrix_s = [a_s(j,n) b_s(j,n);c_s(j,n) d_s(j,n)];
                total_matrix_s = total_matrix_s*form_matrix_s;
            end
            %for p polarization
            capital_a_p(n) = total_matrix_p(1,1);
            capital_b_p(n) = total_matrix_p(1,2);
            capital_c_p(n) = total_matrix_p(2,1);
            capital_d_p(n) = total_matrix_p(2,2);
            %for s polarization
            capital_a_s(n) = total_matrix_s(1,1);
            capital_b_s(n) = total_matrix_s(1,2);
            capital_c_s(n) = total_matrix_s(2,1);
            capital_d_s(n) = total_matrix_s(2,2);

            %for p polarization
            reflection_coe_p(n)      = capital_c_p(n)/capital_a_p(n);
            transmission_coe_p(1,n)  =
total_fresnel_transmission_coe_p(1,n)/capital_a_p(n);
```

```
            reflectance_p(n)         =
reflection_coe_p(n)*conj(reflection_coe_p(n));
            transmittance_p(n)       =
transmission_coe_p(1,n)*conj(transmission_coe_p(1,n));

            total_matrix_p = eye(2,2);
            %for s polarization
            reflection_coe_s(n)      = capital_c_s(n)/capital_a_s(n);
            transmission_coe_s(1,n)  =
total_fresnel_transmission_coe_s(1,n)/capital_a_s(n);
            reflectance_s(n)         =
reflection_coe_s(n)*conj(reflection_coe_s(n)) ;
            transmittance_s(n)       =
transmission_coe_s(1,n)*conj(transmission_coe_s(1,n));

            total_matrix_s = eye(2,2);
        end



            %reflectance_upper = ((complex_refrac_index(2,:)-
1)./(complex_refrac_index(2,:)+1)).^2;% for air
            reflectance_upper=((complex_refrac_index(2,:)-
1.33)./(complex_refrac_index(2,:)+1.33)).^2;%for water
            %reflectance_lower = ((complex_refrac_index(2,:)-
(complex_refrac_index(1,:).^2))./(complex_refrac_index(2,:)+(complex_re
frac_index(1,:)).^2)).^2;
            reflectance_back =reflectance_upper;

            %for p polarization
            relative_reflectance_p = reflectance_p./reflectance_back;
%% remember that this is also a function of angle of incidence and
thickness!
           %for s polarization
            relative_reflectance_s = reflectance_s./reflectance_back;%%
remember that this is also a function of angle of incidence and
thickness!
            complex_rho = reflection_coe_p./reflection_coe_s;

            tan_of_psi_p = abs(reflection_coe_p);
            psi_p_in_deg = 180*(atan(tan_of_psi_p))/pi;
            tan_of_psi_s = abs(reflection_coe_s);
            psi_s_in_deg = 180*(atan(tan_of_psi_s))/pi;

            tan_of_psi = abs(complex_rho);
            psi_in_deg = 180*(atan(tan_of_psi))/pi;

            delta_p_deg_angle = 180/pi*angle(reflection_coe_p);%%%%
angle, atan2 and difference delta are the same
            delta_s_deg_angle = 180/pi*angle(reflection_coe_s);
            delta_in_deg_angle = 180/pi*angle(complex_rho);

    end % for M = angle of incidence
end % for L = thickness of sio2 layer

%%% uncheck this when using multiple wavelengths
```

```
figure
plot(lambda,relative_reflectance_p,'-b',lambda,
relative_reflectance_s,'r');
xlabel('\lambda');ylabel('reflectance (absolute)');
legend('p','s')
```

Matlab file for EKF

```
function [Xest,Yest,P]=ekf(x1,T,Y,pmfun,smfun,P1,R,Q,lambda)
% EKF   Implement EKF algorithm.

Xest=[]; Yest=[]; P=[];
my_size=size(Y);
len_time = my_size(2);
%for i=1:length(Y)
for i=1:len_time
    % measurement update

    Cj=numjac(smfun,x1,lambda);
    %Gk=P1*Cj'*inv(Cj*P1*Cj'+R);
    B=P1*Cj';
    Gk=B/(Cj*P1*Cj'+R);
    xk=x1+Gk*(Y(:,i)-feval(smfun,x1,lambda));
    Pk=P1-Gk*Cj*P1;
    yk=feval(smfun,xk,lambda);
    % model prediction
%    if i~=length(Y)
    if i~=len_time
        Aj=numjac(pmfun,xk,T(i+1)-T(i));
        x1=feval(pmfun,xk,T(i+1)-T(i));
        P1=Aj*Pk*Aj'+Q;
    end
    % save solution
    Xest=[Xest xk];
    Yest=[Yest yk];
    P=[P Pk];

end

% subfunction
function J=numjac(fun,x,varargin)
n=length(x);
a=feval(fun,x,varargin{:});
a=a(:);
hopt=2*sqrt(eps);
for k=1:n
    del=zeros(n,1);
    del(k)=1;
    b=feval(fun,x+hopt*del,varargin{:});
    b=b(:);
    J(:,k)=(b-a)/hopt;
end
```

Matlab file for mMHE

```
function [Xest,Yest]=mmhefminunc_my(x1,T,Y,pmfun,smfun,N,P1,R,Q,lambda)
% MMHEFMINUNC   Implement mMHE algorithm using fminunc.

close all
Xest=[]; Yest=[]; P=[];

% initialize options for optimization
%options = optimset('fminunc');
options = optimset('fminsearch');
options = optimset(options, 'LargeScale', 'off','TolFun',1e-
10,'TolCon',1e-10);

for i=N:length(T)
    % data in current window
    xdata=T(i)-T(i-N+1:i);
    ydata=Y(:,i-N+1:i);
    % optimization

%xopt=fminunc(@mmheobj,real(x1),options,real(xdata),ydata,pmfun,smfun,r
eal(x1),P1,R,lambda);

xopt=fminsearch(@mmheobj,real(x1),options,real(xdata),ydata,pmfun,smfun
,real(x1),P1,R,lambda);
    % reconstruct state and output

    xmmhe=xopt; Xmmhe=xmmhe;
    Ymmhe=feval(smfun,xmmhe,lambda);
    for j=1:length(xdata)-1
        xmmhe=feval(pmfun,xmmhe,xdata(j)-xdata(j+1));
        Xmmhe=[Xmmhe xmmhe];
        ymmhe=feval(smfun,xmmhe,lambda);
        Ymmhe=[Ymmhe ymmhe];
    end
    % save solution
    Xest(:,i)=Xmmhe(:,N);  % save estimated state %% note the big
difference
    Yest(:,i)=Ymmhe(:,N);  % save calculated output
    % EKF update
    xs=xopt;                    % xs is the first smoothed estimate,
x(k-m+1|k)
    Cj=numjac(smfun,xs,lambda);        % Jacobian matrix at xs for
sensor model
    Gk=(P1*Cj')/(Cj*P1*Cj'+R);
    %Gk=P1*Cj'*inv(Cj*P1*Cj'+R); % P1 is P(k-m+1|k-m)
    %ydata(:,1);
    %i
    xk=x1+Gk*(ydata(:,N)-Ymmhe(:,N)-Cj*(x1-xs));    % xk: x(k-m+1|k-
m+1), x1: x(k-m+1|k-m)
    Pk=P1-Gk*Cj*P1;   % pekf: P(k-m+1|k-m+1)
    P=[P Pk];
    % model prediction
        Aj=numjac(pmfun,xs,xdata(1)-xdata(2));
```

```
        x1=feval(pmfun,xs,xdata(1)-xdata(2))+Aj*(xk-xs);      % update
x1
        P1=Aj*Pk*Aj'+Q;
end

% subfunction
function f=mmheobj(xi,xdata,ydata,pmfun,smfun,x1,P1,R,lambda)
x1e=xi-x1; % initial state error
%f=x1e'*inv(P1)*x1e;
f=(x1e'/P1)*x1e;
x=xi;
v=ydata(:,1)-feval(smfun,x,lambda);
%f=f+v'*inv(R)*v;
f = f + (v'/R)*v;
for i=1:length(xdata)-1
    x=feval(pmfun,x,xdata(i)-xdata(i+1));
    v=ydata(:,i+1)-feval(smfun,x,lambda);
    %f=f+v'*inv(R)*v;
    f = real(f + (v'/R)*v);
end

% subfunction
function J=numjac(fun,x,varargin)
n=length(x);
a=feval(fun,x,varargin{:});
a=a(:);
hopt=2*sqrt(eps);
for k=1:n
    del=zeros(n,1);
    del(k)=1;
    b=feval(fun,x+hopt*del,varargin{:});
   %b=feval(fun,x+hopt,varargin{:});
    b=b(:);
    J(:,k)=(b-a)/hopt;
end
```

Matlab file for RLS

```
function [Xest,Yest]=rlsfminunc_my(x1,T,Y,pmfun,smfun,N,lambda)
% RLSFMINUNC   Implement RLS algorithm using fminunc.

close all
Xest=[]; Yest=[];

% initialize options for optimization
%options = optimset('fminunc');
options = optimset('fminsearch');
options = optimset(options, 'LargeScale', 'off','TolFun',1e-
10,'TolCon',1e-10);

for i=N:length(T)
    % data in current window
    xdata=T(i)-T(i-N+1:i);
    ydata=Y(:,i-N+1:i);
```

```
    % optimization

%xopt=fminunc(@rlsobj,real(x1),options,real(xdata),ydata,pmfun,smfun,la
mbda);

xopt=fminsearch(@rlsobj,real(x1),options,real(xdata),ydata,pmfun,smfun,
lambda);

%xopt=lsqnonlin(@rlsobj,x1,[],[],options,xdata,ydata,pmfun,smfun,lambda
);
    % reconstruct state and output
    xrls=xopt;
    Xrls=xrls;
    Yrls=feval(smfun,xrls,lambda);
    for j=1:length(xdata)-1
        xrls=feval(pmfun,xrls,xdata(j)-xdata(j+1));
        Xrls=[Xrls xrls];
        yrls=feval(smfun,xrls,lambda);
        Yrls=[Yrls yrls];
    end
    % save solution
    Xest(:,i)=Xrls(:,N);    % save estimated state
    Yest(:,i)=Yrls(:,N);    % save calculated output
    % update x1
    x1=Xrls(:,N);% note the change
end

% subfunction
function f=rlsobj(xi,xdata,ydata,pmfun,smfun,lambda)
x=xi;
v=ydata(:,1)-feval(smfun,x,lambda);
f=v'*v;
for i=1:length(xdata)-1
    x=feval(pmfun,x,xdata(i)-xdata(i+1));
    v=ydata(:,i+1)-feval(smfun,x,lambda);
    f=real(f+v'*v);
end
```

APPENDIX M: Coherance length effect

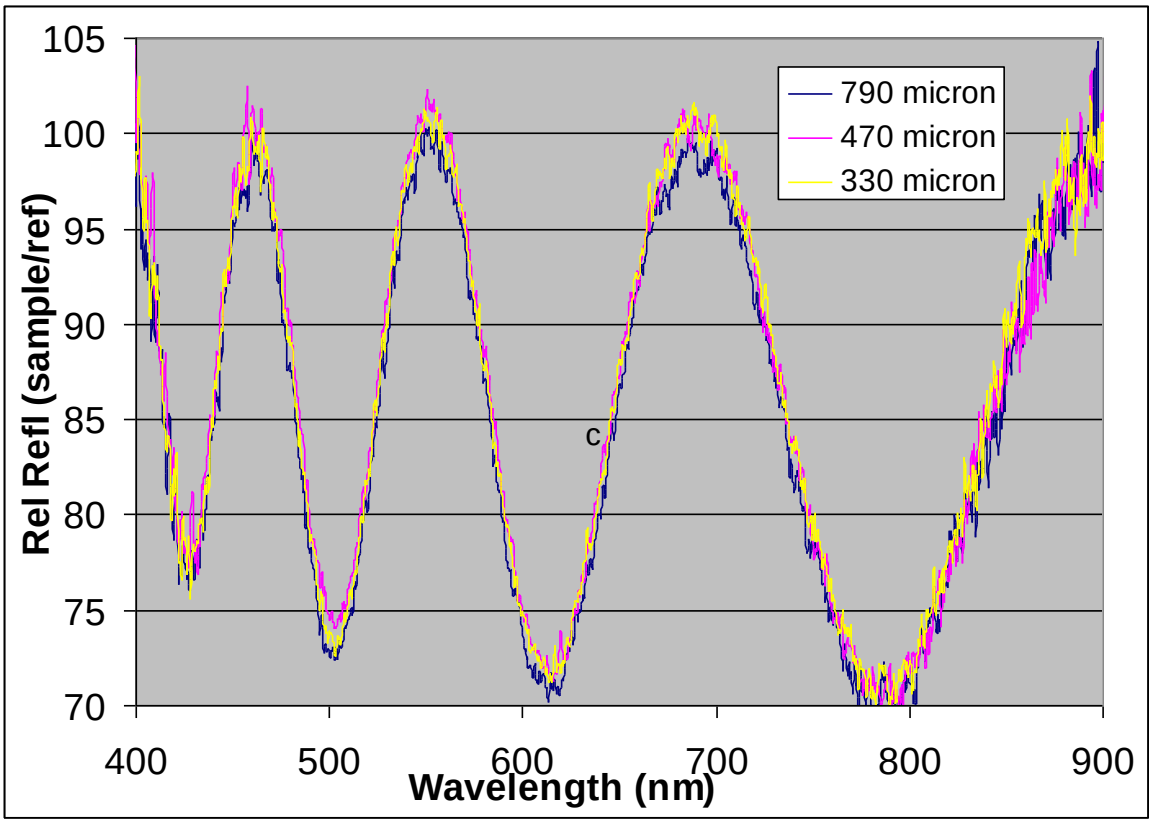

Figure 86 effect of water layer thickness on reflectance spectra for SiO2 film on Si

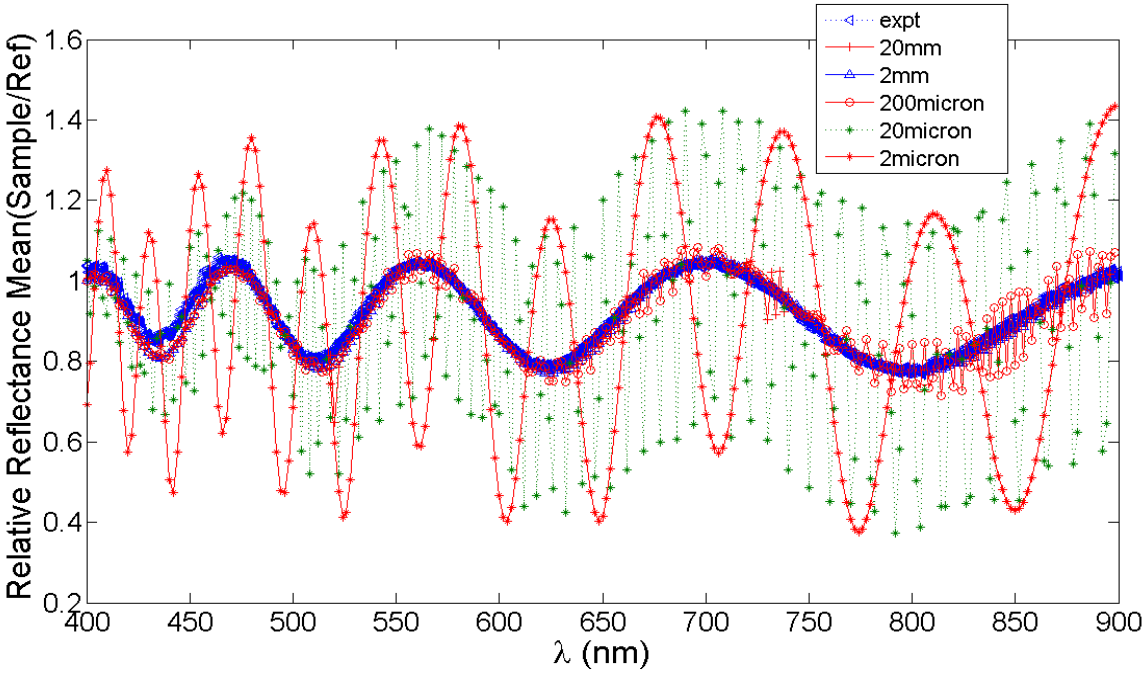

Figure 87 effect of water layer thickness, relative reflectance values are computed at every 0.01nm interval and then averaged over 2 nm window, reference is a water layer of 20 mm thickness over Si

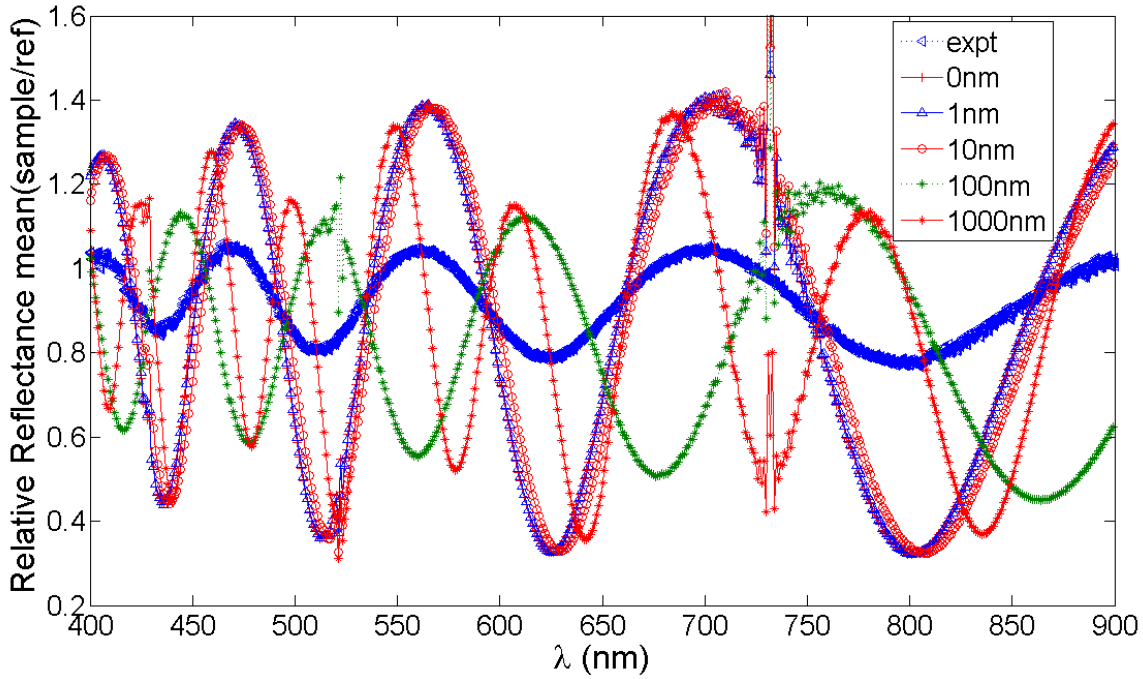

Figure 88 effect of water layer thickness, relative reflectance values are computed at every 0.01nm interval and then averaged over 2 nm window, reference is a water layer of 20 mm thickness over Si

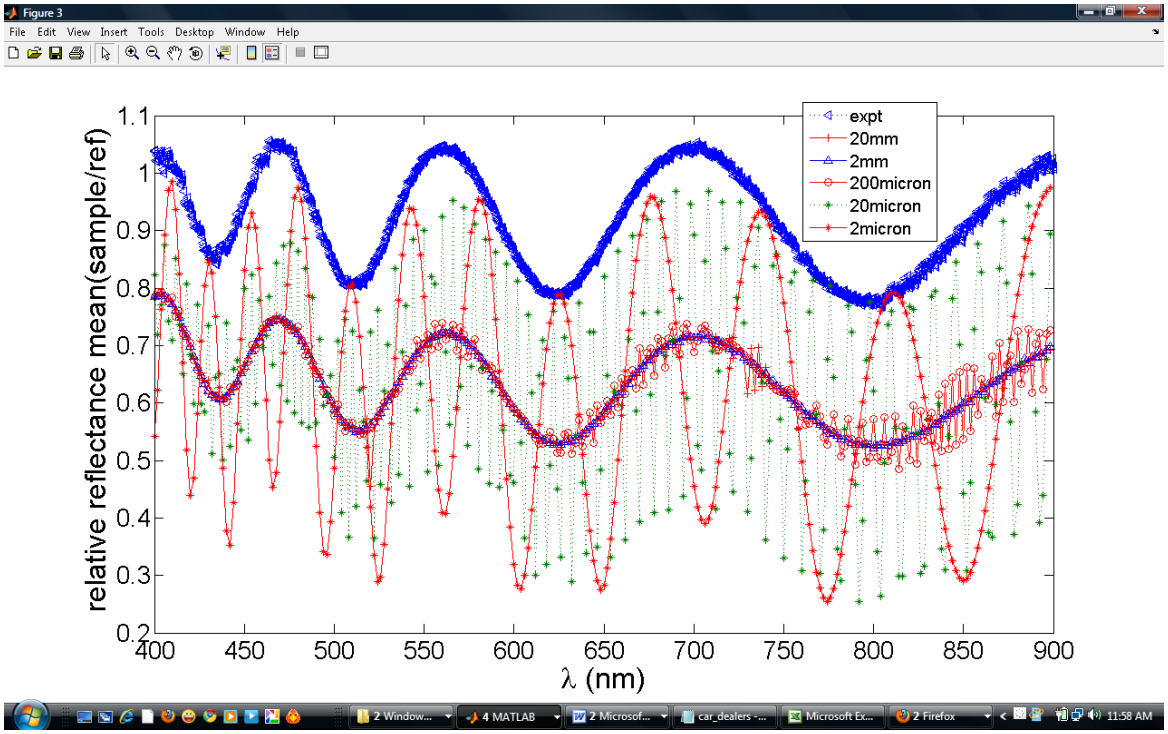

Figure 89 effect of water layer thickness, relative reflectance values are computed at every 0.01nm interval and then averaged over 1 nm window, reference is bare Si

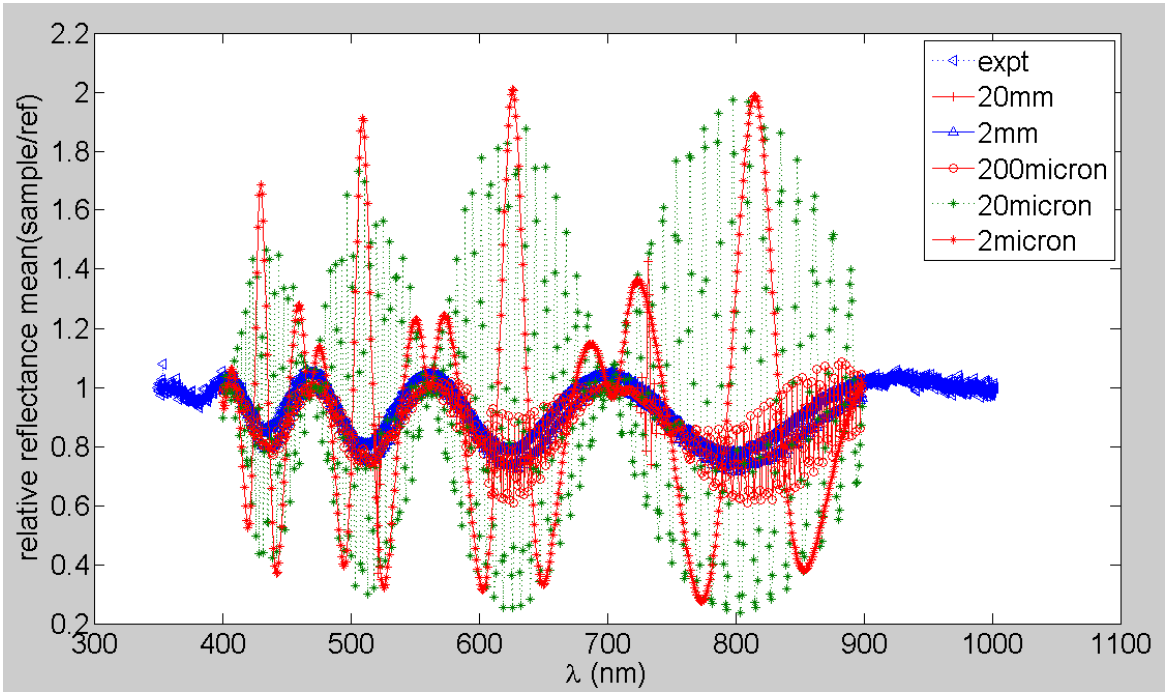

Figure 90 effect of water layer thickness, relative reflectance values are computed at every 0.01nm interval and then averaged over 1 nm window, reference is water layer of the same thickness for which absolute reflectance values are calculated

APPENDIX N: Arbitrary profile generation by estimators

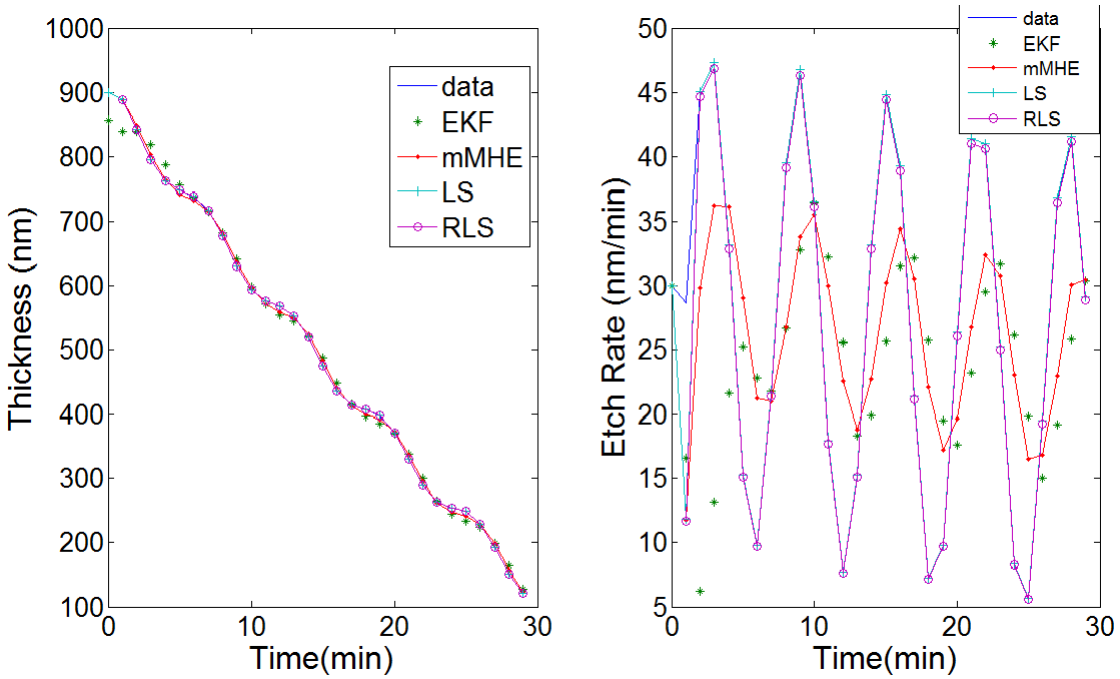

Figure 91 Simulated thickness and ER variation with time for ZnO film with thickness varying sinusoidally, a =0.99, for estimator, initial guess = [850, 30] , m=2

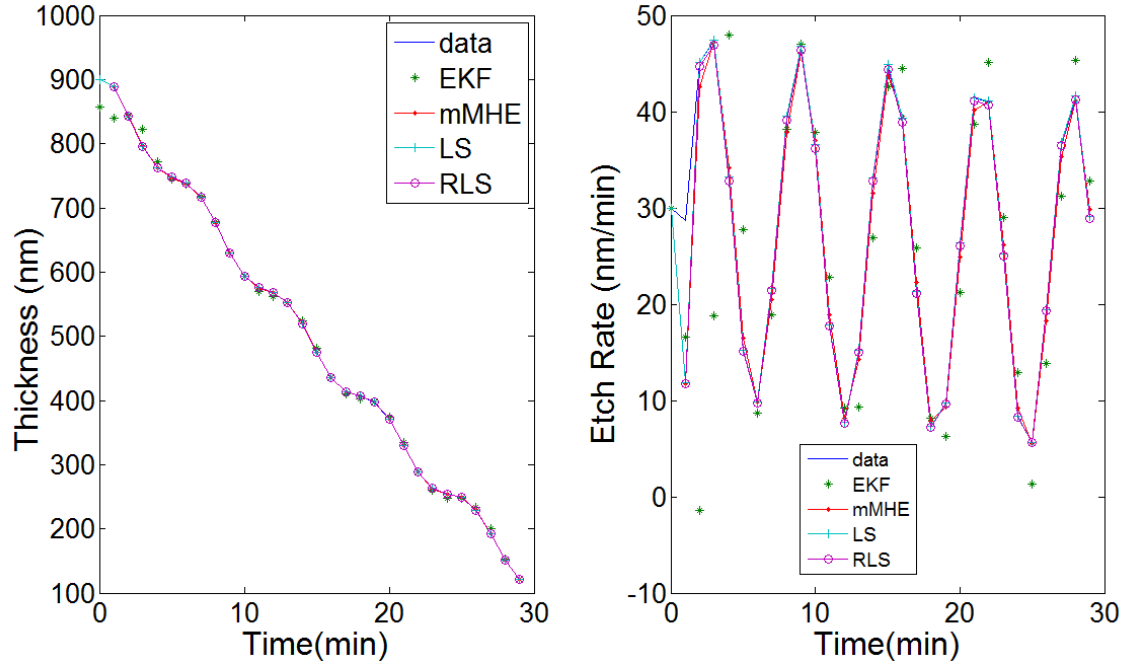

Figure 92 Simulated thickness and ER variation with time for ZnO film with thickness varying sinusoidally, a =0.99, for estimator, initial guess = [850, 30] , m=2, Q = [1e-4 0, 0

1e0],

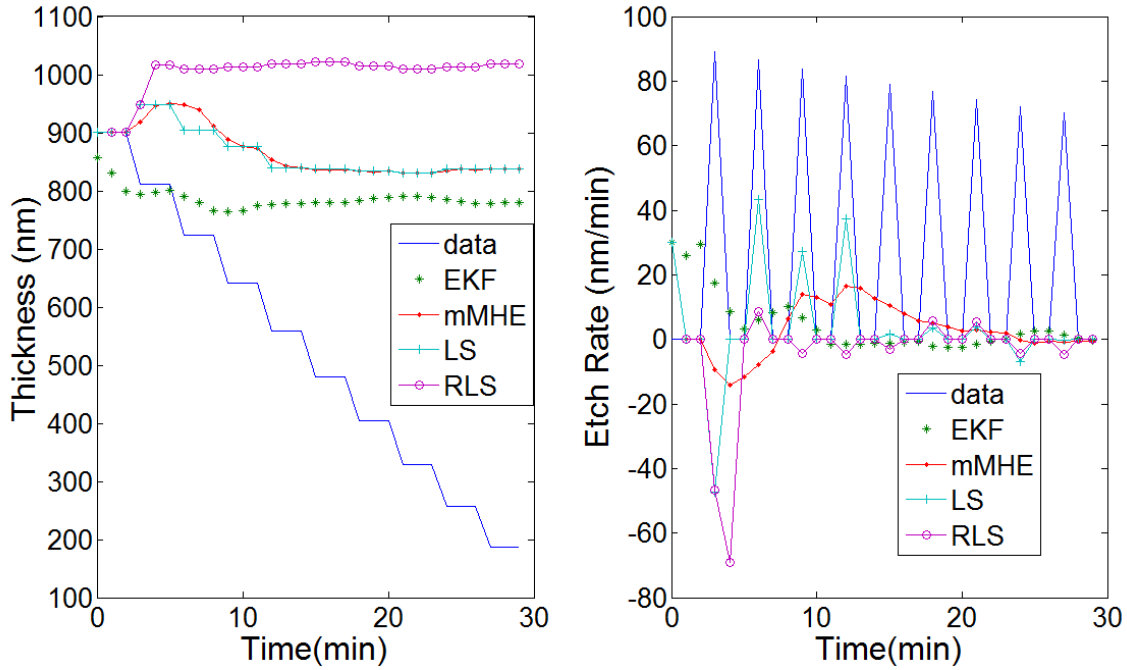

Figure 93 Simulated thickness and ER variation with time for ZnO film with thickness varying in staircase manner, a =0.99 for estimator, initial guess = [850, 30] , m=2

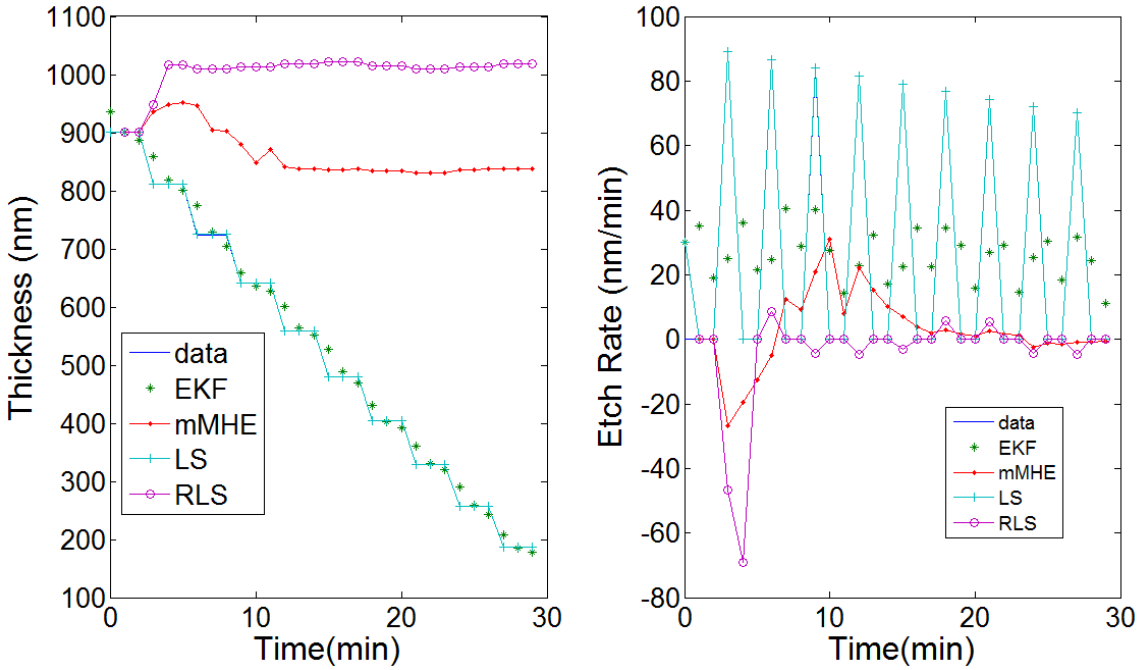

Figure 94 Simulated thickness and ER variation with time for ZnO film with thickness varying in staircase manner, a =0.99 for estimator, initial guess = [950, 30] , m=2, and initial guess for LS is 0.95*previous thickness value

REFERENCES

(1) www.itrs.net Accessed Jan, 15, 2010.

(2) http://www.ausairpower.net/OSR-0700.html Accessed Jan, 15, 2010.

(3) *Cleaning and Surface Conditioning Technology in Semiconductor Device Manufacture*; Hattori, T.; Novak, R. W.; Ruzyllo, J.; Besson, P.; Mertens, P., Eds.; The Electrochemical Society: Pennington, 2007; Vol. 11.

(4) Levitin, G.; Hess, D. W. In *Handbook for Cleaning/Decontamination of Surfaces,* ; Johansson, I., Somasundaran, P., Eds. 2007.

(5) Reinhardt, K. A.; Kern, W. *Handbook of Silicon Wafer Cleaning Technology*; 2 ed.; William Andrew, Norwich, NY, 2008.

(6) www.en.wikipedia.org Accessed Jan, 15, 2010.

(7) Monk, D. J.; Soane, D. S.; Howe, R. T. *Thin Solid Films* 1993, *232*, 1.

(8) Monk, D. J.; Soane, D. S.; Howe, R. T. *J. Electrochem. Soc.* 1993, *140*, 2339.

(9) Kikuyama, H.; Waki, M.; Kawanabe, I.; Miyashita, M.; Yabune, T.; Miki, N.; Takano, J.; Ohmi, T. *J. Electrochem. Soc.* 1992, *139*, 2239.

(10) Somashekhar, A.; O'Brien, S. *J. Electrochem. Soc.* 1996, *143*, 2885.

(11) Kikuyama, H.; Waki, M.; Miyashita, M.; Yabune, T.; Miki, N.; Takano, J.; Ohmi, T. *J. Electrochem. Soc.* 1994, *141*, 366.

(12) Kern, W.; Deckert, C. A. In *Thin Film Processes*; Vossen, J. L., Kern, W., Eds.; Academic Press, New York: 1978, p 401.

(13) Kikyuama, H.; Miki, N.; Saka, K.; Takano, J.; Kawanabe, I.; Miyashita, M.; Ohmi, T. *IEEE Trans. Semicond. Manufacturing* 1991, *4*, 26.

(14) Spierings, G. A. C. M. *J. Mat. Sci* 1993, *28*, 6261.

(15) Knotter, D. M. *J. Am. Chem. Soc.* 2000, *122*, 4345.

(16) Kern, W. In *Handbook for Cleaning/Decontamination of Surfaces*; Johansson, I., Somasundaran, P., Eds.; Elsevier: 2007, p 3.

(17) Gale, G. W.; Small, R. J.; Reinhardt, K. A. In *Handbook for Cleaning/Decontamination of Surfaces*; Johansson, I., Somasundaran, P., Eds.; Elsevier: 2007, p 201.

(18) Mucha, J. A.; Hess, D. W.; Aydil, E. S.; Thompson, L. F., Willson, C. G., Bowden, M. J., Eds.; ACS Professional Reference Book, Washington: 1994, p 377.

(19) Hess, D. W.; Reinhardt, K. A. In *Handbook for Cleaning/Decontamination of Surfaces*; Johansson, I., Somasundaran, P., Eds.; Elsevier: 2007, p 355.

(20) Behr, F. E.; Rajtar, P. E.; Zazzera, L. A.; Parent, M. J.; Theiss, S. K.; Weaver, B. L. US patent No. 6492309 B1.

(21) Wojtczak, W. A.; Dewulf, D.; Collins, S.; Sachem, Inc. (Austin, TX)

(22) Xiong, R. T.; Wissmann, P. J.; Gallivan, M. A. *Comput Chem Eng* 2006, *30*, 1657.

(23) Vincent, T. L.; Khargonekar, P. P.; Terry, F. L. *J Electrochem Soc* 1997, *144*, 2467.

(24) Middlebrooks, S. A.; Rawlings, J. B. *Ieee T Semiconduct M* 2007, *20*, 114.

(25) Judge, J. S. *J. Electrochem. Soc.* 1971, *118*, 1772.

(26) Kikuyama, H.; Miki, N.; Saka, K.; Takano, J.; Kawanabe, I.; Miyashita, M.; Ohmi, T. *IEEE Trans. Semicond. Manufacturing* 1990, *3*, 99.

(27) Proksche, H.; Nagorsen, G.; Ross, D. *J. Electrochem. Soc.* 1992, *139*, 521.

(28) Kunii, Y.; Nakayama, S.; Maeda, M. *J. Electrochem. Soc.* 1995, *142*, 3510.

(29) Braddy, R.; McTigue, P. T.; Verity, B. *J. Fluorine Chem.* 1994, *66*, 63.

(30) Giguere, P. A.; Turrell, S. *J. Am. Chem. Soc.* 1980, *102*, 5473.

(31) Warren, L. J. *Anal. Chim. Acta.* 1971, *53*, 199.

(32) Kolasinski, K. W. *J. Electrochem. Soc.* 2005, *152*, J99.

(33) *Cleaning Technology in Semiconductor Device Manufacture VII*; Verhaverbeke, S.; Truman, K., Eds.; Electrochemical Society Proceedings, 2001; Vol. 2001-26.

(34) Born, H. H.; Prigogine, M. *J. Chim. Phys.* 1979, *79*, 538.

(35) Kline, W. E.; Fogler, H. S. *J. Coll. Int. Sci.* 1981, *82*, 93.

(36) White, L. K. *Thin Solid Films* 1981, *79*, L73.

(37) Zhang, X. G. *Electrochemistry of Silicon and Its Oxide*; Kluwer, New York, 2001.

(38) Osseo-Asare, K. *J. Electrochem. Soc.* 1996, *143*, 1339.

(39) Woods, C.; Garcia, J. P.; de Larios, J. U. S. Patent No. 7,198,055, April 3, 2007.

(40) Christe, K. O.; Wilson, W. W. *J. Fluorine Chem.* 1990, *46*, 339.

(41) Watanabe, D.; Momota, H.; Kezuka, T.; Kanemura, T.; Itano, M.; Riley, D.; Barnett, J. In *Semiconductor Pure Water and Chemicals Conference Proceedings* 2003.

(42) Rafols, C.; Herodes, K.; Beltran, J. L.; Bosch, E.; Roses, M. *J. Electroanal. Chem.* 1997, *433*, 77.

(43) Anthony, J. L.; Brennecke, J. F.; Holbrey, J. D.; Edward J. Maginn; Mantz, R. A.; Rogers, R. D.; Trulove, P. C.; Visser, A. E.; Welton, T. In *Ionic Liquids in Synthesis.*; P. Wasserscheid, Welton, T., Eds.; Wiley-VCH Verlag GmbH & Co. KGaA: 2002.

(44) Christe, K. O.; Wilson, W. W. *Journal of fluorine chemistry* 1990, *47*, 117.

(45) Speight, J. G. *Lange's Handbook of Chemistry* 16th edition ed.; McGraw-Hill, 2005.

(46) Wyman, J., Jr.; Ingalls, E. N. *J. Am. Chem. Soc.* 1938, *60*, 1182.

(47) Gross, P. M., Jr.; Taylor, R. C. *J. Am. Chem. Soc.* 1950, *72* 2075.

(48) Sinyakov, Y. I.; Gorbanev, A. I.; Povarov, Y. M.; Kessler, Y. M. *Russ. Chem B+* 1961, *10*, 1410.

(49) Rosenfarb, J.; Baker, R. J. *J. Phys. Chem.-US* 1978, *82*, 329.

(50) Reichardt, C. *Solvent effects in organic chemistry*; Verlag chemie GmbH: Weinheim, 1979.

(51) Kumbharkhane, A. C.; Helambe, S. N.; Lokhande, M. P.; Doraiswamy, S.; Mehrotra, S. C. *Pramana J. Phys.* 1996, *46*, 91.

(52) Yang, L.-J.; Yang, X.-Q.; Huang, K.-M.; Jia, G.-Z.; Shang, H. *Int J Mol Sci.* 2009, *10*, 1261.

(53) Schneider, H. *Electrochim. Acta* 1976, *21*, 711.

(54) Verhaverbeke, S.; Teerlinck, I.; Vinckier, C.; Stevens, G.; Cartuyvels, R.; Heyns, M. M. *J. Electrochem. Soc.* 1994, *141*, 2852.

(55) Moakes, G.; Daemen, L. L.; Gelbaum, L. T.; Leisen, J.; Marecek, V.; Janata, J. *J. Phys. Chem. B* 2007, *111*, 7312.

(56) Haque, R.; Reeves, L. W. *J. Am. Chem. Soc.* 1967, *89*, 250.

(57) Shashkov, S. N.; Kiselev, M. A.; Tioutiounnikov, S. N.; Kiselev, A. M.; Lesieur, P. *Physica B* 1999, *271*, 184.

(58) Marcus, Y. *J. Chem. Thermodyn.* 2007, *39*, 1338.

(59) Mitsumori, K.; Haga, N.; Kasama, Y.; Takahashi, N.; Imaoka, T.; Ohmi, T.; Novak, R. E., Ruzyllo, J., Hattori, T., Eds.; Electrochemical Society Proceedings: 1999; Vol. 99-36, p 37.

(60) *Cleaning Technology in Semiconductor Device Manufacture VI*; Heyns, M.; Bearda, T.; Cornelissen, I.; DeGendt, S.; Loweenstein, L.; Mertens, P.; Mertnes, S.; Meuris, M.; Schaekers, M.; Teerlinck, I.; Vos, R.; Wolke, K., Eds.; Electrochemical Society Proceedings, 1999; Vol. 99-36.

(61) Ruzyllo, J.; Hattori, T.; Novak, R. E.; Mertens, P.; Besson, P. In *Cleaning and Surface Conditioning Technology in Semiconductor Device Manufacture*; Hattori, T., Novak, R. W., Ruzyllo, J., Besson, P., Mertens, P., Eds.; The Electrochemical Society, Pennington: 2007; Vol. 11.

(62) Singhal, S.; Elkhatib, B.; Stuber, J.; Sreenivasan, S. V.; Ezekoye, O. A. *Ieee Transactions on Semiconductor Manufacturing* 2009, *22*, 399.

(63) Hangos, K. M.; Cameron, I. T. *Process modelling and model analysis*; San Diego : Academic Press, 2001.

(64) de Larios, J. M.; Ravkin, M.; Travis, G.; Keller, J.; Krusell, W. U. S. 6,616,722, September 9, 2003.

(65) Ravkin, M.; de Larios, J. M. May 16, 2006.

(66) O'Donnell, R. J. US 7093,375 B2, August 22,2006.

(67) Ghadiali, S. N.; Gaver, D. P., III *J. Fluid Mech.* 2003, *478*, 165.

(68) O'Brien, S. B. G. M. *J. Fluid Mech.* 1993, *254*, 649.

(69) Britten, J. A. *Chem. Eng. Cornrn.* 1993, *120*, 59.

(70) Eom, D.-H.; Kim, K.-S.; Park, J.-G. *Jpn. J. Appl. Phys.* 2002, *41*, 5881.

(71) Ansys; Ansys Inc.

(72) Heavens, O. S. *Optical properties of thin solid films*; New York, Academic Press, 1955.

(73) Azzam, R. M. A.; Bashara, N. M. *Ellipsometry and polarized light*; North-Holland Pub. Co. New York, 1987.

(74) Yeh, P. *Optical waves in layered media*; John Wiley & Sons Inc: New York, 1988.

(75) Hale, G. M.; Querry, M. R. *Applied Optics* 1973, *12*, 555.

(76) Monk, D. J.; Soane, D. S.; Howe, R. T. *J. Electrochem. Soc.* 1994, *141*.

(77) Fogler, H. S. *Elements of Chemical Reaction Engineering*; Third ed.; Prentice Hall of India: New Delhi, 2003.

(78) Prunici, P.; Hess, P. *Journal of Applied Physics* 2008, *103*.

(79) Choi, S.; Kim, T. H.; Everitt, H. O.; Brown, A.; Losurdo, M.; Brun, G.; Moto, A. *J Vac Sci Technol B* 2007, *25*, 969.

(80) Tompkins, H. G.; McGahan, W. A. *Spectroscopic Ellipsometry and reflectometry, a user's guide*; John Wiley and Sons, Inc, 1999.

(81) Tompkins, H. G.; Irene, E. A. *Handbook of ellipsometry*; William Andrew Publishing/Noyes, 2005.

(82) Rancourt, J. D. *Optical thin films : users handbook* Bellingham, Wash. : SPIE Optical Engineering Press, 1996.

(83) Agrawal, A. Ph.D., Georgia Institute of Technology, 2003.

(84) Hu, Y. Z.; Sharangpani, R.; Tay, S.-P. *J. Vac. Sci. Technol. A* 2000, *18*, 2527.

(85) Xiong, R. T.; Grover, M. A. *Ieee T Contr Syst T* 2009, *17*, 1228.

(86) Pande, A. A.; Mui, D. S. L.; Hess, D. W. *IEEE Transactions on Semiconductor Manufacturing*.

(87) Max Born; Emil Wolf; A. B. Bhatia *Principles of Optics: Electromagnetic Theory of Propagation, Interference and Diffraction of Light* 7ed.; Cambridge University Press, 2000.

(88) de Larios, J. M.; Ravkin, M.; Travis, G.; Keller, J.; Krusell, W. U. S., September 9, 2003.

(89) Ravkin, M.; de Larios, J. M. U. S., May 16, 2006.

(90) Woods, C.; Garcia, J. P.; de Larios, J. U. S. , April 3, 2007.

(91) Yoo, D. G.; Nam, S. H.; Kim, M. H.; Jeong, S. H.; Jee, H. G.; Lee, H. J.; Lee, N. E.; Hong, B. Y.; Kim, Y. J.; Jung, D.; Boo, J. H. *Surf Coat Tech* 2008, *202*, 5476.

(92) Lee, D. K.; Lee, S. J.; Bang, J.; Yang, H. *J Electrochem Soc* 2009, *156*, D211.

(93) Mathworks *MATLAB User's guide*, 2010.

(94) Guspiel, J.; Riesenkampf, W. *Hydrometallurgy* 1993, *34*, 203.

(95) http://en.wikipedia.org/wiki Accessed Jan, 15,2010.

(96) Joback, K. G.; Reid, R. C. *Chem Eng Commun* 1987, *57*, 233.

(97) *Perry's Chemical Engineers' Handbook*; 7 ed.; Perry, R. H.; Green, D. W., Eds.; Mc-Graw Hill, 1997.

(98) NIST 2008.

(99) www.tut.fi/units/me/ener/laitteistot/EFD/LDA.html 2010.

(100) Chabal, Y. J. *Surf. Sci. Rep.* 1988, *8*, 211.

(101) Urban, M. W. *Attenuated Total Reflection Spectroscopy of Polymers*; American Chemical Society, Washington, D.C., 1996.

(102) http://nmr-analysis.blogspot.com/2008/07/dosy-nmr.html 2010.

(103) Leal, L. G. *Laminar flow and convective transport processes*; Butterworth-Heinemann: Boston, 1992.

(104) Park, J.-G.; Lee, S.-H.; Ryu, J.-S.; Hong, Y.-K.; Kim, T.-G.; Busnaina, A. A. *Journal of The Electrochemical Society* 2006, *153*, G811.

(105) Alay, J.-L.; Verhaverbeke, S.; Vandervorst, W.; Heyns, M. *Jpn. J. Appl. Phys., 32*, 358.

(106) Park, J.-G.; Pas, M. F. *J. Electrochem. Soc.*, *142*, 2028.

(107) Sides, P. J.; Hoggard, J. D. *Langmuir* 2004, *20*, 11493.

(108) Werner, C.; Zimmermann, R.; Kratzmuller, T. *Colloids and Surfaces A* 2001, *192*, 205.

(109) Kirby, B. J.; Hasselbrink, E. F., Jr. *Electrophoresis* 2004, *25*, 187.

(110) http://www.malvern.co.uk/labeng/technology/images/zeta_potential_schematic.png Accessed Jan, 15, 2010.

(111) Kolasinski, K. W. *J. Electrochem. Soc.* 2005, *152*, J99.

(112) McTigue, P.; O'Donnell, T. A.; Verily, B. *Austr. J. Chem.* 1985, *38*, 1797.

(113) Bell, R. P.; Bascombe, K. N.; McCoubrey, J. C. *J. Chem. Soc.* 1956, 1286.

(114) Miki, N.; Maeno, M.; Ohmi, T. *J. Electrochem. Soc.* 1990, *137*, 790.

(115) Clark, R. P.; Moser, J. R. *J. Electrochem. Soc.* 1971, *118*, 666.

(116) Broderick, S. J. *J. Chem. Eng. Data* 1962, *7*, 55.

(117) Bard, A. J. *Electrochemical methods*; John Wiley and Sons, 1980.

(118) Herzinger, C. M.; Johs, B.; McGahan, W. A.; Woollam, J. A.; Paulson, W. *Journal of Applied Physics* 1998, *83*, 3323.

(119) G. E. Jellison, J. *Optical Materials* 1992, *1*, 41.

(120) http://www.scholarpedia.org/article/Backward_differentiation_formulas Accessed Jan, 15, 2010.

(121) http://en.wikipedia.org/wiki/Five-point_stencil Accessed Jan, 15, 2010.